NATURE OF OXYGEN SPECIES ON Au(111) AND Ag(111) MODEL CATALYSTS AND THEIR ROLE IN O-H, C-H, C-C, N-H BOND ACTIVATION

A DISSERTATION SUBMITTED TO

THE GRADUATE SCHOOL OF ENGINEERING AND SCIENCE

OF BILKENT UNIVERSITY

IN PARTIAL FULFILLMENT OF THE REQUIREMENTS FOR

THE DEGREE OF

DOCTOR OF PHILOSOPHY

IN

CHEMISTRY

By

Mustafa Karatok

October 2017

NATURE OF OXYGEN SPECIES ON Au(111) AND Ag(111) MODEL CATALYSTS AND THEIR ROLE IN O-H, C-H, C-C, N-H BOND ACTIVATION

By Mustafa Karatok

October 2017

We certify that we have read this dissertation and that in our opinion it is fully adequate, in scope and in quality, as a dissertation for the degree of Doctor of Philosophy.

Emrah Özensoy(Advisor)

Şefik Süzer

Oğuz Gülseren

Ahmet Oral

Hande Toffoli

Approved for the Graduate School of Engineering and Science:

Ezhan Karasan
Director of the Graduate School

ABSTRACT

NATURE OF OXYGEN SPECIES ON Au(111) AND Ag(111) MODEL CATALYSTS AND THEIR ROLE IN O-H, C-H, C-C, N-H BOND ACTIVATION

Mustafa Karatok
Ph.D. in Chemistry
Advisor: Emrah Özensoy
October 2017

Metal-catalyzed heterogeneous oxidation reactions have high importance for the large-scale production of the commodity chemicals vastly used in the chemical industry. Controlling the selectivity in such processes to increase the product yield and minimize the production of undesired byproducts requires a molecular level understanding of the bond activation mechanisms. Thus, understanding the nature of oxygen species in various bond cleavage processes is critical. In the current work, nature of oxygen species was studied on the planar Au(111) and Ag(111) single crystal model catalyst surfaces via x-ray photoelectron spectroscopy (XPS), temperature programmed desorption/ temperature programmed reaction spectroscopy (TPD/TPRS), low energy electron diffraction (LEED) and infrared reflection absorption spectroscopy (IRAS) techniques under ultra-high vacuum (UHV) conditions. Ozone (O_3) was utilized as the oxygen delivery agent providing atomic oxygen to the reacting surface. Various oxygen species were determined on both Au(111) and Ag(111) model catalysts and their role in O-H, C-H, C-C and N-H bond activation was investigated by using probe molecules such as methanol, acetaldehyde and ammonia. Three different oxygen species such as atomic oxygen (O_a), subsurface oxygen (O_{sub}) and surface oxide (O_{ox}) were determined on Au(111) single crystal. Oxygen accumulation on Au(111) surface at 140 K for θ_O<1.0 MLE of oxygen coverage resulted in the surface atomic oxygen (O_a) formation while 2D surface oxide (O_{ox}) started to grow for θ_O>1.0 MLE of oxygen coverage at the same temperature. It was also shown that oxygen atoms dissolved (O_{sub}) into the bulk of the Au(111) single crystal when oxygen was accumulated at 473 K. Atomic oxygen species (O_a) on Au(111) was found to be very active for the cleavage of O-H and C-H bonds in methanol; C-C bond in acetaldehyde; N-H bond in ammonia molecules. Surface oxide (O_{ox}) overlayer was also active for methanol oxidation, however it showed very high

selectivity towards CO_2. Dissolved oxygen atoms (O_{sub}) revealed almost no activity in methanol oxidation reactions on Au(111). In a similar manner, three different oxygen species were determined on the Ag(111) surface such as surface atomic oxygen (O_a), surface oxide (O_{ox}) and bulk-like oxide (O_{bulk}) species. Disordered atomic oxygen (O_a) and surface oxide (O_{ox}) overlayers prepared at 140 K on Ag(111) for $\theta_O \leq 0.2$ MLE were found to be very active for O-H and C-H bond cleavage producing formaldehyde as the dominant product. Increasing oxygen quantity for both oxygen species (0.7 MLE $\leq \theta_O \leq$ 1.3 MLE) resulted mostly CO_2 formation. O_a ($\theta_O <$ 1.10 MLE) was also found to be highly active in N-H bond cleavage for ammonia and selective to N_2 as the dominant product. On the other hand, ordered p(5×1) and c(4×8) surface oxide (O_{ox}) overlayers on Ag(111) prepared 473 K were found to be almost entirely inactive for N-H cleavage. Extreme oxygen exposures on Ag(111) ($\theta_O >$ 1.93 MLE) at 140 K led to bulk-like silver oxide (O_{bulk}) species with poor N_2 selectivity in ammonia oxidation and increasing extent of formation of toxic pollutants such as NO and N_2O.

Keywords: Oxidation Catalyst, Bond Activation, Model Catalyst, Au(111), Ag(111).

ÖZET

OKSİJEN TÜRLERİNİN Au(111) VE Ag(111) MODEL KATALİZÖRLERİ ÜZERİNDEKİ DOĞASI VE O-H, C-H, C-C, N-H BAĞ AKTİVASYONUNDAKİ ROLLERİ

Mustafa Karatok
Kimya, Doktora
Tez Danışmanı: Emrah Özensoy
Ekim 2017

Metal katalizli heterojen oksidasyon reaksiyonları, kimya endüstrisinde büyük ölçekli olarak üretilen ürünlerin üretiminde büyük önem taşımaktadır. Ürün verimini arttırmak ve istenmeyen yan ürünlerin üretimini en aza indirmek için bu tür proseslerde seçiciliğin kontrolü, molekül seviyesinde bağ aktive etme mekanizmalarının anlaşılmasını gerektirmektedir. Bu nedenle, çeşitli bağ kırılma süreçlerinde oksijen türlerinin doğasını anlamak kritik önem taşımaktadır. Mevcut çalışmada, x-ışını fotoelektron spektroskopisi (XPS), sıcaklık programlı desorpsiyon / sıcaklık programlı reaksiyon spektroskopisi (TPD / TPRS), düşük enerjili elektron kırınımı (LEED) ve kızılötesi yansıma absorpsiyon spektroskopisi (IRAS) teknikleri kullanılarak düzlemsel Au(111) ve Ag(111) tek kristal model katalizör yüzeyleri üzerindeki oksijen türlerinin doğası ultra-yüksek vakum (UHV) koşulları altında incelenmiştir. Atomik oksijeni sağlaması bakımından oksijen kaynağı olarak ozon (O_3) kullanılmıştır. Au(111) ve Ag(111) model katalizörler üzerindeki çeşitli oksijen türleri belirlenip, bu türlerin metanol, asetaldehit ve amonyak gibi moleküller kullanılarak O-H, C-H, C-C ve N-H bağ aktivasyonlarındaki rolü araştırılmıştır. Au(111) tek kristali üzerinde yüzey atomik oksijen (O_a), yüzey altı oksijen (O_{sub}) ve yüzey oksit (O_{ox}) olmak üzere üç farklı oksijen türü belirlenmiştir. Au(111) üzerinde 140 K sıcaklıkta, 1 tek katman eşdeğeri (MLE) ve daha az miktarda oksijen birikimi, atomik yüzey oksijeni (O_a) oluşumuyla sonuçlanırken, aynÄś sıcaklıkta 1 MLE'den daha fazla oksijen birikimiyle birlikte 2 boyutlu yüzey oksit oluşmaya başladığı saptanmıştır. Ayrıca oksijenin 473 K sıcaklıktaki yüzeye gönderilmesiyle oksijen atomlarının Au(111) tek kristalinin içerisinde çözündüğü (O_{sub}) gösterilmiştir. Yüzeyde bulunan oksijen atomlarının (O_a) metanoldeki O-H ve C-H; asetaldehitteki C-C; amonyaktaki N-H bağlarının kırılmasında çok aktif olduğu görülmüştür. Yüzeydeki oksit katmanının (O_{ox}) da metanol ile tepkimeye girdiği, fakat bu tepkime sonucunda CO_2

oluşmasına karşı çok yüksek seçicilikte olduğu görülmüştür. Au(111) tek kristali içerisinde çözünmüş olan oksijen atomları (O_{sub}) metanol oksidasyon reaksiyonlarında neredeyse hiç aktivite göstermemiştir. Benzer şekilde Ag(111) tek kristali üzerinde yüzey atomik oksijen (O_a), yüzey oksit (O_{ox}) ve balk oksit (O_{bulk}) olmak üzere üç farklı oksijen türü belirlenmiştir. 140 K sıcaklıkta 0.2 MLE ve daha az oksijen ile oluşturulan düzensiz dizilmiş atomik oksijen (O_a) ve yüzey oksit (O_{ox}) katmanlarının metanoldeki O-H ve C-H bağlarının kırılmasında aktif olduğu ve baskın ürün olarak formaldehit oluşturduğu görülmüştür. Artan oksijen miktarıyla birlikte (0.7 MLE $\leq \theta_O \leq$ 1.3 MLE), bahsedilen her iki tür de çoğunlukla CO_2 oluşumuna sebep olmaktadır. Ayrıca O_a türünün ($\theta_O <$ 1.10 MLE) amonyak molekülündeki N-H bağ kırılmasında aktif olduğu ve baskın ürün olarak N_2 oluşturduğu saptanmıştır. Diğer taraftan, Ag(111) tek kristali üzerinde 473 K sıcaklıkta oluşturulan p(5×1) ve c(4×8) yüzey dizilimindeki yüzey oksit (O_{ox}) katmanının N-H bağ kırılmasında neredeyse tamamen pasif olduğu görülmüştür. Ag(111) üzerinde 140 K sıcaklıkta yüksek oksijene ($\theta_O >$ 1.93 MLE) maruz bırakılarak oluşturulan balk gümüş oksit (O_{bulk}) türünün ise amonyak oksidasyonu tepkimesinde N_2 oluşumuna karşı düşük seçicilik gösterdiği ve NO, N_2O gibi toksik kirleticilerin oluşumunu artırdığı saptanmıştır.

Anahtar sözcükler: Oksidasyon Katalizörü, Bağ Aktivasyonu, Model Katalizör, Au(111), Ag(111).

Acknowledgements

First of all, I would like to express my sincere gratitude to my advisor, Dr. Emrah Özensoy for his patience, motivation and immense knowledge. I deeply appreciated that he believed in my potential and gave me an opportunity to be part of his team. His guidance helped me all throughout my research and he has become my role model with his scientific enthusiasm and vision.

Besides my advisor, I would like to thank the rest of my thesis committee, Dr. Şefik Süzer, Dr. Coşkun Kocabaş, Dr. Hande Toffoli, Dr. Oğuz Gülseren and Dr. Ahmet Oral for their insightful comments and invaluable time.

My sincere thanks goes to my former lab mate, Dr. Evgeny Vovk, for his patience and support in the first few tough years of my graduate work. I also thank to my lab mates Asad Shah, Ali Vâlâ Koç and Bartu Karakurt for their collaboration, companionship and for all the fun we have had in the lab.

I owe my deepest gratitude to a spectacular craftsman, Ethem Anber, not only for his help in technical problems and for giving useful design ideas, but also for sharing his life experiences and for his advice.

I would like to thank to Sean McWhorter for his friendship and for encouraging me in my desperate times. I would also like to thank to other group members that I worked with in different projects: Dr. Zafer Say, Dr. Deniz Erdoğan, Kerem Emre Ercan, Merve Kurt, Aybegüm Samast, Elif Perşembe, Merve Balcı, and one of my lunch partner in the last months, Mohammed Irfan, for their cooperation and friendship.

I also would like to acknowledge Dr. Mehmet Erbudak from ETH Zurich for his contributions regarding the construction of the UHV experimental setup.

I would like to thank to the Scientific and Technological Research Council of Turkey (TUBITAK) (Project code: 112T589) for the financial support.

I would like to offer my special thanks to my mom and dad, for their love and support during my education.

Finally my deepest appreciation goes to my wife, Dr. Zahide Pamir Karatok, who was very patient and thoughtful although she was conducting her own stressful research. She supported me all the time and deserves all the credit for encouraging me to apply to Bilkent in the first place.

Contents

1 Introduction **1**

1.1 Motivation of the Study 1

1.2 Nature of Oxygen on Au(111) Single Crystal 3

1.3 Nature of Oxygen on Ag(111) Single Crystal 5

2 Experimental **8**

2.1 Temperature Programmed Desorption/ Reaction Spectroscopy . . 9

2.2 X-ray Photoemission Spectroscopy 13

2.3 Infrared Reflection Absorption Spectroscopy 15

2.4 Low Energy Electron Diffraction 19

2.5 Atomic Oxygen Accumulation Methods 21

2.5.1 NO_2 and water co-adsorption 22

2.5.2 Ozone Decomposition 24

3 Bond Activation on Gold **26**

3.1 Characterization of the Au(111) Single Crystal Surface 26

3.2 Oxygen Behavior on Au(111) Single Crystal 29

3.2.1 Examination of the Activity of Oxygen Overlayers on Au(111) by Titration with CO Molecules 37

3.3 C-H and O-H Activation on Au(111) Single Crystal 38

3.3.1 Methanol on Clean Au(111) Single Crystal 39

3.3.2 Methanol on Oxygen pre-covered Au(111) Single Crystal . 41

3.4 C-C Activation on Au(111) Single Crystal 45

3.4.1 Acetaldehyde and Methyl Formate on Clean Au(111) Single Crystal 45

3.4.2 Acetaldehyde on Oxygen Pre-covered Au(111) 49
3.5 N-H Activation on Au(111) 52
3.5.1 Ammonia adsorption on clean Au(111) 52
3.5.2 Ammonia on Oxygen Pre-covered Au(111) 53

4 Bond Activation on Silver 56
4.1 Characterization of the Ag(111) Single Crystal Surface 56
4.2 Oxygen Behavior on Ag(111) Single Crystal 58
4.3 C-H and O-H Activation on Ag(111) 65
4.3.1 Methanol on Clean Ag(111) 66
4.3.2 Methanol on oxygen pre-covered Ag(111) 68
4.3.3 The Effect of Methanol Dosage Temperature to the Methanol Oxidation Reaction Pathways 75
4.4 N-H Activation on Ag(111) 77
4.4.1 Ammonia on Clean Ag(111) 77
4.4.2 Ammonia on Oxygen Pre-covered Ag(111) 81

5 Conclusions 87
5.1 Bond Activation by Au(111) 87
5.2 Bond Activation by Ag(111) 89

A Diagram of the IRAS Setup 108

B QMS Fragmentation Patterns of the Chemicals 109

C Infrared Frequencies and Mode Assignments for Methanol and Methoxy Species on Ag(111) 110

D Alternative depiction of TPRS data for ammonia SCO reaction 111

E TPRS profiles for NH_3 and H_2O during ammonia SCO reaction 112

F List of Publications 113

List of Figures

1.1 (100), (110) and (111) fcc crystal surfaces. Adapted from Ref. [14] (All atoms are identical, color coding for different layers are for visualization only) 3

2.1 Pictures of the multicomponent UHV system 9
2.2 Schematic setup for TPD experiments under UHV conditions. Adapted from Ref. [65] 10
2.3 Representative TPD spectra for (a) zeroth, (b) first and (c) second order desorption kinetics. Adapted from Ref. [68] 12
2.4 (a) Diagram of the photoemission process. (b) Universal curve that is plot of IMFP values of the metals as a function of the kinetic energy of electrons. Figures were adapted from Ref. [65] 14
2.5 (a) A dual anode x-ray source configuration. Adapted from Ref. [72] (b) A double-pass cylindrical Mirror Energy Analyzer. Adapted from Ref. [73] 15
2.6 (a) Phase shifts of IR light components as a function of the angle of incidence on a metal surface. Adapted from Ref. [74]. (b) A schematic representation of dipole moments of a diatomic molecule located perpendicular and parallel to the metal surface and their image dipoles on the surface. (c) Electric field and intensity functions of p-polarized light in copper surface as a function of the angle of incidence. Adapted from Ref. [74] 17
2.7 Scaled-drawings and final view of the IRAS chamber that was designed and manufactured in the current work 18

2.8 Scaled-drawings and final view of the IRAS setup that was designed and manufactured in the current work 19
2.9 (a) Constructive interference phenomena and the relationship between the real space vs. k-space basis vectors in a LEED experiment. (b) A schematic of a LEED configuration. Adapted from Ref. [75] 21
2.10 Custom-design NO_2 dosing line equipped with a stainless steel disc pinhole (Diameter = 5 μm). 23
2.11 Schematic of the custom-made $Pb(NO_3)_2$(s)-based NO_2 delivery system. 23
2.12 Details of the custom-made ozonizer and ozone trap accommodating the silica gel. 24
2.13 (a) Commercial ozone generator, ozone trap (b) before and (c) after ozone storage. 25

3.1 Reconstructed Au(111) unit cell [89]. b) STM image of a reconstructed Au(111) surface (size 120×120 nm^2) in UHV. Inset shows an atomic resolution image (8×6 nm^2) where the unit cell is marked with a rectangle. Adapted from Ref. [91] 27
3.2 A representative survey XP spectrum of the clean Au(111) single crystal. 28
3.3 (a) Au *4f* XP spectrum (b) LEED pattern of the clean Au(111) single crystal. 29
3.4 O_2 TPD profiles with increasing coverage of atomic oxygen on Au(111) prepared via ozone decomposition at 460 K (a), 300 K (b) and 140 K (c). 31
3.5 Au *4f* region XP spectra of high coverage oxygen layers (θ_O = 2 MLE) on Au(111) prepared at 460 K (a), 300 K (b) and 140 K (c) in comparison to the clean Au(111) single crystal. 34
3.6 Au4f region XP spectra of Au(111) including 0.8 MLE oxygen overlayer prepared at 140 K in comparison to Au *4f* spectrum of clean Au(111) surface. 35

3.7 O *1s* XP spectra of the oxygen overlayers on Au(111) prepared and monitored at 140 K. The right panel shows the O *1s* spectrum recorded after heating of the 0.9 MLE oxygen layer to 300 K (the spectrum was acquired at 300 K). 36
3.8 TPD profiles of O/Au(111) overlayers before and after reaction with CO. TPD profiles showing m/z=32 desorption channel for oxygen recorded after ∼0.7 MLE of oxygen accumulation at (a) 460 K, (b) 300 K and (c) 140 K (red spectra) and spectra monitored after subsequent 3.0 L of CO exposure (10^{-8} Torr × 5 min.) on the analogous O/Au(111) overlayers at 140 K (blue spectra). . . . 38
3.9 TPD profiles (m/z=31) obtained after methanol adsorption on clean Au(111) surface at 90 K as a function of increasing methanol coverage. Reprinted with permission from [110] Copyright (2017) Springer (order number: 4206641091824). 40
3.10 IRAS spectra of monolayer and multilayer of methanol on clean Au(111) 41
3.11 TPRS profiles for the reaction of methanol with oxygen accumulated at (a) 460 K, (b) 140 K on Au(111). 42
3.12 TPRS profile showing desorption channels of methyl formate (oxidative coupling product) and formaldehyde (partial oxidation product) obtained after methanol exposure to oxygen pre-covered Au(111). 43
3.13 TPRS profiles for the reaction of methanol with (a) 0.3 MLE (b) 1.2 MLE of oxygen accumulated at 300 K on Au(111) 44
3.14 Coverage-dependent TPD profiles for the m/z = 29 desorption channel obtained *via* acetaldehyde (CH_3CHO(g)) adsorption on the clean Au(111) model catalyst surface at 90 K. Inset emphasizes the non-monotonic intensity of the chemisorbed acetaldehyde desorption feature at 139 K as a function of acetaldehyde coverage. 47
3.15 Coverage-dependent TPD profiles for the m/z=43 desorption channel obtained via methyl acetate (CH_3COOCH_3(g)) adsorption on the clean Au(111) model catalyst surface at 90 K. 48

3.16 TPRS profiles for various desorption channels obtained after 2.9 MLE of acetaldehyde accumulation at 90 K on 0.1 MLE of oxygen pre-covered Au(111) model catalyst surface at 140 K 50
3.17 TPD profiles (m/z = 17) obtained after ammonia adsorption on clean Au(111) surface at 90 K as a function of increasing ammonia coverage 52
3.18 TPRS profiles for the reaction of ammonia (0.6 MLE) at 83 K (a) and 190 K (b) on 0.3 MLE oxygen pre-covered gold surface at 190 K. 54
3.19 TPRS profiles for the reaction of ammonia (0.6 MLE) at 190 K on 0.6 MLE oxygen pre-covered gold surface at 190 K. 55

4.1 A representative survey XP spectrum of the clean Ag(111) single crystal. 57
4.2 (a) Ag *3d* XP spectrum (b) LEED pattern of the clean Ag(111) single crystal. 58
4.3 (a) TPD profiles for oxygen desorption (m/z = 32) obtained by increasing ozone exposures on clean Ag(111) at 140 K. (b) Relative oxygen surface coverages (obtained via integrated TPD desorption signals in part (a)) for surface and subsurface oxygen species on Ag(111) as a function of ozone exposure. 60
4.4 LEED images of O/Ag(111) overlayers obtained by introducing different ozone exposures at 140 K on clean Ag(111) surface followed by pumping and annealing to 473 K in UHV. (a) LEED image of the p(5x1)-O/Ag(111) overlayer (θ_O = 0.83 MLE) and (b) its simulated (theoretical) LEED pattern. (c) LEED image of the c(4x8)-O/Ag(111) overlayer (θ_O = 1.10 MLE) and (d) its simulated (theoretical) LEED pattern. 62
4.5 O *1s* XPS spectra of O/Ag(111) as a function of increasing oxygen coverage obtained by increasing exposures of ozone at 140 K. Inset on the right shows the integrated O *1s*/Ag *3d* signal ratio as a function of oxygen coverage. Inset on the left shows the O *1s* XPS spectra for O/Ag(111) with θ_O = 2.66 MLE dosed at 140 K (red) and dosed at 473 K (black). 64

4.6 Normalized Ag *3d* XPS spectra for clean Ag(111) (black), θ_O = 1.93 MLE O/Ag(111) (blue), θ_O = 3.70 MLE O/Ag(111) (red) and subtracted spectrum of clean Ag(111) from θ_O = 3.70 MLE O/Ag(111) (green). 65
4.7 TPD profiles (m/z = 31) obtained after methanol adsorption on clean Ag(111) surface at 100 K as a function of increasing methanol coverage. 67
4.8 IRAS spectra of methanol adsorption on clean Ag(111) surface at 100 K as a function of methanol surface coverage. 68
4.9 TPRS profiles for the reaction of methanol with oxygen on Ag(111). In all of the experiments, an identical exposure of methanol ($P_{methanol}$ = 1.0 x 10^{-9} Torr x 60 sec.) was dosed at 200 K on oxygen-covered (θ_O = 0.7 MLE) Ag(111) surface, where oxygen was delivered by ozone exposure either at (a) 140 K or at (b) 473 K 69
4.10 TPRS profiles of methanol oxidation reaction products (*i.e.* formaldehyde, methanol, CO_2) for the reaction between methanol (T*ads*=200 K) and oxygen pre-covered Ag(111) surfaces as a function of oxygen coverage. 71
4.11 Integrated TPRS desorption signals for the methanol oxidation products (*i.e.* formaldehyde, methanol, CO_2) on O/Ag(111) surface including either O_a or O_{ox} species as a function of oxygen coverage extracted from the TPRS data given in Figure 4.10. . . . 72
4.12 IRAS spectra of methanol (1.0 MLE) on O_a/Ag(111) for various oxygen coverages at 140 K 73
4.13 IRAS spectra of methanol (1.0 MLE) on O/Ag(111) (θ_O = 0.7 MLE) for methanol accumulation temperature (a) at 100 K, (b) at 100 K followed by annealing to 300 K, (c) at 300 K. 76
4.14 TPRS spectra of methanol (1.0 MLE) on O/Ag(111) (θ_O = 0.7 MLE) for methanol accumulation temperature (a) at 100 K and (b) at 300 K. 77

4.15 TPD profiles (m/z=17) obtained after ammonia adsorption on clean Ag(111) surface at 90 K as a function of increasing ammonia coverage. 78
4.16 IRAS spectra of ammonia adsorption on clean Ag(111) surface at 90 K as a function of ammonia surface coverage. 80
4.17 TPRS profiles for the reaction of ammonia with oxygen on Ag(111). In all of the experiments, an identical exposure of NH_3 (P_{NH3} = 2.0 x 10^{-9} Torr x 60 s) was dosed at 250 K on oxygen-covered (θ_O = 0.21 MLE) Ag(111) surface, where oxygen was delivered by ozone exposure either at 140 K (multi-colored spectra) or at 473 K (grey-colored spectra). 82
4.18 TPRS profiles of various ammonia SCO reaction products (i.e. N_2, NO, N_2O) for the reaction between ammonia and oxygen pre-covered Ag(111) surfaces as a function of oxygen coverage. For all of the data, oxygen was delivered on Ag(111) by ozone exposure at 140 K, while NH_3 was delivered using an identical ammonia exposure at 250 K (P_{NH3} = 2.0 x 1010^{-9} Torr x 60 s) 84
4.19 Integrated TPD desorption signals for the main ammonia SCO products (i.e. N_2, NO, N_2O) on O/Ag(111) surface as a function of oxygen coverage extracted from the TPRS data given in Figure 4.18. 85

5.1 Reactivity and selectivity trends of methanol oxidation reaction on O/Au(111) as a function of oxygen coverage and temperature. . . 88
5.2 Reactivity and selectivity trends of ammonia SCO on O/Ag(111) as a function of oxygen coverage and temperature. 90

D.1 Alternative depiction of the TPRS data corresponding to the various ammonia SCO reaction products (*i.e.* N_2, NO, N_2O) for the reaction between ammonia and oxygen pre-covered Ag(111) surfaces as a function of oxygen coverage. For all of the data, oxygen was delivered on Ag(111) by ozone exposure at 140 K, while NH_3 was delivered after ozone using an identical ammonia exposure at 250 K ($P(NH_3)$ = 2.0 × 10^{-9} Torr × 60 sec.) 111

E.1 TPRS profiles for NH_3 ($m/z = 17$) and H_2O ($m/z = 18$) desorption channels obtained during the reaction between ammonia and oxygen pre-covered Ag(111) surfaces as a function of oxygen coverage as shown in Figure 4.18 of the main text. 112

List of Tables

4.1 Vibrational frequency assignments for the NH_3/Ag(111) IRAS data presented in Figure 4.16 81

Chapter 1

Introduction

1.1 Motivation of the Study

Catalytic processes contribute to the production of most of the materials and chemicals that we use in our daily life *e.g.* food, fabric, construction material, oil, pharmaceutical industries. Furthermore, most of the processes, especially in chemical industry, rely on heterogeneous catalytic reactions [1, 2]. Despite the limited surface area of solid catalysts compared to homogeneous catalysis, ease of separation and wide range of operation conditions make heterogeneous catalysis an industrially advantageous approach. Metal-catalyzed heterogeneous oxidation reactions are particularly crucial for the large scale production of commonly used commodity chemicals [3]. For example, formaldehyde is produced in industrial scale from methanol partial oxidation on solid silver catalysts [4]. Synthesis of carbonyl derivatives from alcohols constitutes an important portion of organic chemical product synthesis [5]. Several carbonyl derivatives such as aldehydes, ketones, carboxylic acids and esters can be synthesized from the corresponding alcohols by conventional organic synthesis methods [6]. However, these methods have strong environmental drawbacks due to the use of heavy-metal salts as oxidizing agents, generation of undesired byproducts and the utilization of toxic solvents [5, 7, 8]. Thus, heterogeneous catalysis enables large scale chemical

production *via* green chemistry methods.

Selectivity is the main concern in the catalytic oxidation reactions. For example, in the formaldehyde production process from methanol on silver catalysts, formic acid and carbon dioxide are also produced as byproducts [4]. It was shown that the same reaction leads to methyl formate formation on gold catalyst as a result of a coupling reaction pathway [9]. Various metals were shown to be active in ammonia oxidation reaction for the purpose of ammonia abatement. Depending on the reaction conditions, the formation of the toxic byproducts such as NO, NO_2, N_2O were reported in addition to the main product, N_2 [10]. Controlling the selectivity in such reactions in order to increase the product yield and to minimize the production of undesired byproducts requires a molecular level understanding of the bond activation mechanisms. Thus, understanding the nature of oxygen in the O-H, C-H, C-C and N-H bond cleavage processes for oxidation reactions is critical in terms of the selectivity of the catalyst.

Catalytic activity of metal nanoparticles varies with the nanoparticle size and shape as well as with the nature of the support material. However, understanding the structure-catalytic functionality relationships are quite challenging. In order to obtain fundamental insights regarding the detailed catalytic mechanisms of the catalysts, atomically well-defined planar model catalysts can be used a versatile platform where surface structure and reaction parameters can be readily controlled. However, such well-defined model catalysts can not survive under atmospheric conditions due to the adsorption of atoms and molecules in the air. In order to maintain the catalyst surface clean for a long time and to perform atomic scale experiments, ultra high vacuum (UHV) is needed. Thus, well-defined model catalysts such as Au(111) and Ag(111) single crystals under UHV conditions are ideal environments to examine the nature of oxygen for oxidation reactions.

There are three common crystal structures for stacking bulk metal atoms, namely face-centered cubic (fcc), body centered cubic (bcc) and hexagonal close packed (hcp). While the alkali metals and a few transitions metals crystallize in bcc, most of the metals prefer stacking in either fcc or hcp system [11]. Surface structure of the metals varies depending on their bulk crystal arrangement. Most

of the precious metals including gold and silver exhibit fcc structure[12]. Cutting an fcc crystal along the unit cell in any direction creates surfaces with different atomic orientations which can be labeled by using Miller indices. Most commonly observed crystal faces are (111), (110) and (100) planes which have relatively high atomic density and low surface free energy [13]. Schematic drawing of these faces are given in Figure 1.1 [14].

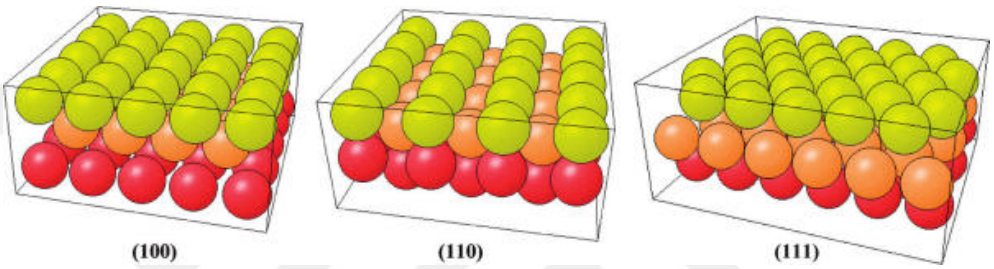

Figure 1.1: (100), (110) and (111) fcc crystal surfaces. Adapted from Ref. [14] (All atoms are identical, color coding for different layers are for visualization only)

Based on Density Functional Theory (DFT) calculations, the surface free energies of (100), (110) and (111) facets of gold are found to be 0.08, 0.10 and 0.05 eV/Å^2, respectively [14]. Among these facets, (111) surface has the lowest surface free energy rendering it the most stable termination which is also the most frequently observed facet in experimental studies on gold nanoparticles [15]. In a similar manner, silver nanoparticles mostly consist of (111) facet [16]. Thus, performing reactions on Au(111) and Ag(111) single crystal surfaces is an effective way of understanding the catalytic behavior of gold and silver nanoparticles.

1.2 Nature of Oxygen on Au(111) Single Crystal

Gold had been considered as an inert metal until the pioneering work of Bond et al. on the hydrogenation of olefins over supported gold catalysts [17]. Afterwards, Hutchings [18] and Haruta [19] reported that gold nanoparticles have high activity for acetylene hydrochlorination and CO oxidation, respectively. After the

discovery of catalytically active gold, numerous reports were published in various heterogeneous catalytic applications such as water-gas shift reaction, CO oxidation, hydrocarbon oxidation, NO reduction, alkene epoxidation, selective alcohol and aldehyde oxidation reactions [20, 21]. Bonding of partial oxidation reaction intermediates/byproducts on gold surfaces are relatively weak compared to other catalytically active metals favoring catalytic selectivity on gold [22]. Highly selective catalytic character of gold makes it unique and this property allows the production of carbonyl derivatives by selective oxidation reactions.

In order to understand the nature of oxygen on Au(111) single crystal surfaces, numerous studies were performed and different oxygen species were mentioned in the literature. Min *et al.* reported three different oxygen species such as chemisorbed oxygen, surface oxide and bulk oxide on Au(111) single crystal depending on the adsorption temperature and quantity of oxygen [23]. In this study, the most active species for CO oxidation was reported as the chemisorbed oxygen which was formed at 200 K. In another study, Baker *et al.* utilized High Resolution Electron Energy Loss (HREEL) spectroscopy to investigate the oxygen overlayers on the Au(111) surface and reported two oxygen features [24]. In agreement with theoretical calculations, the first feature which is dominant at low coverages was attributed to chemisorbed oxygen atoms in 3-fold sites; while the second feature which prominent at near saturation coverages was associated with surface oxide. Besides, the transformation of the active oxygen species to the inactive ones was reported by Ojifinni et *al.* [25]. In this study, oxygen species formed at 77 K was shown to be active towards CO oxidation and pre-annealing of O/Au(111) overlayers to a certain temperature was shown to increase the quantity of inactive oxygen species. It was suggested that at higher temperatures the adsorbed atomic oxygen species transform from the metastable state (which is responsible for greater reactivity) to a more stable (*i.e.* less reactive) state.

Another debate about the oxygen species on gold catalysts is the formation of gold oxide. Former studies showed that gold oxide on the bulk metallic gold can be formed at stronger oxidizing conditions depending on the method of oxygen layer preparation [26, 27, 28]. However gold oxide shows low stability and starts to decompose at room temperature [27]. Although it was mentioned in the literature

many times that bulk gold oxide is formed after ambient ozone treatment at elevated temperatures, the conclusive experimental evidences were not presented [14, 24, 23, 29]. In another study, Klyushin *et al.* demonstrated with *in-situ* XPS that gold oxide on the gold foil was stable only in the presence of ozone (0.3 mbar) and decomposed under vacuum at 373 K or even in the presence of ozone at temperatures higher than 523 K [28]. In the same work, estimated thickness of the oxide phase was 0.4±0.1 nm which coincides with the smallest axis of the Au_2O_3 unit cell, pointing to the formation of surface gold oxide.

Surface morphology of the Au(111) single crystal was also investigated after the formation of oxygen overlayers and it was demonstrated that gold surface morphology changed drastically after atomic oxygen adsorption. According to a Scanning Tunneling Microscopy (STM) data, adsorption of oxygen on the clean Au(111) surface initiates reconstruction of the characteristic herringbone structure to a stripped one [30] and leads to corrugation of the surface [23]. Corrugation manifests itself as release of the gold atoms from the surface yielding a roughened surface. The degree of corrugation depends on oxygen coverage and preparation temperature; the corrugation is stronger at high coverages and high temperatures. DFT studies in the literature agree with the experimental results suggesting the formation of corrugated gold surface and conclude that the cost of adatom creation can easily be compensated at high oxygen coverages [31, 32]. It is interesting that the morphology of the corrugated surface remains unchanged after removal of the surface oxygen by reaction with CO [33].

1.3 Nature of Oxygen on Ag(111) Single Crystal

O/Ag(111) system is an important catalytic system which has been thoroughly investigated within the context of different catalytic reactions in the last few decades both experimentally [34, 35, 36, 37, 38, 39, 40, 41, 42, 43, 44] and/or

theoretically [45, 46, 47, 48, 49, 50]. Campbell reported that atomic oxygen populated at 490 K by high pressure (5 Torr) O_2 dosage on Ag(111) is active for CO oxidation [38]. Ertl and co-workers reported two distinct surface oxygen atoms on Ag(111) and claimed that only one type of surface oxygen which was stable up to 900 K took part in the methanol partial oxidation reaction to formaldehyde [51]. They also reported that dissolved oxygen species was inactive in this reaction. In another study, Bukhtiyarov and co-workers revealed two types of oxygen species on a silver foil which were claimed to be ionic and covalent oxygen [52]. They found that the covalent oxygen takes part in ethylene epoxidation reaction while ionic oxygen yields only CO_2. In their following work, they found that covalent oxygen is active for an electrophilic addition to the C=C bond of ethylene while the ionic oxygen is active in a nucleophilic attack to C-H bond [42]. Thus, they named these oxygen species as electrophilic and nucleophilic oxygen. .

Oxygen containing Ag(111) surfaces are known to undergo surface reconstruction readily. The most commonly observed reconstruction of this system is the *p(4x4)* structure which was first observed by Rovida *et al.* [34]. The atomic structure of the *p(4x4)* reconstruction was revised in 2000 [53] and even a more recent model was proposed by Schnadt *et al.* in 2006 [49]. In addition, other reconstructions of the O/Ag(111) system were also observed such as $(\sqrt{3}\times\sqrt{3})R30^{o}$ [54], $c(3\times5\sqrt{3})rect$ [49], (7×7) [44], $c(4\times8)$ [50] and $p(4\times5\sqrt{3})rect$ structures [50]. Reconstruction process of Ag(111) surface was reviewed by Michaelides *et al.* [55].

Yet, recent studies indicate that O/Ag(111) structure proves to be an elusive system to understand in a comprehensive manner at the atomic scale [56, 57, 58, 59, 60, 61, 62]. Rocha *et al.* revealed five different atomic oxygen species by ambient pressure XPS on silver single crystals, polycrystalline silver and powders depending on the oxygen accumulation temperature and quantity [63]. Atomic oxygen species reported in that particular study have different electronic structures and their role in oxidation reactions on silver catalysts are still questionable. In another study in 2016, Derouin *et al.* showed that sub-surface oxygen formation on Ag(111) single crystal strongly depended on the reaction conditions and such species existed during the industrial conditions of ethylene

epoxidation reaction [58]. Thus, sub-surface oxygen might also have a critical role in various oxidation reactions on silver catalysts.

Chapter 2

Experimental

Experiments were performed in a custom-made UHV chamber with a base pressure of 2x10^{-10} Torr which is equipped with X-ray Photoemission Spectroscopy (XPS), Low Energy Electron Diffraction (LEED), Infrared Reflection Absorption Spectroscopy (IRAS) and Temperature Programmed Desorption/Reaction Spectroscopy (TPD/TPRS) capabilities. These characterization techniques were explained in detail in the sections below. A turbo molecular pump (Varian, TV 551 Navigator) with a pumping speed of 550 l/s for N_2 was used to evacuate the UHV chamber. An additional titanium sublimation pump (TSP) with titanium filaments (Varian, Model 916-0017) and a control unit (Balzers, USS2) was used to remove residual gases especially H_2. Pressure inside the UHV chamber was followed by an ionization gauge (Varian, UHV-24). Pictures of the UHV system are given in Figure 2.1.

Au(111) and Ag(111) single crystal samples (10 mm-diameter $\times$ 1 mm-thickness disc, both sides polished, MaTeck GmbH) were affixed on Ta wires through which the sample could be resistively heated up to 1073 K. The cooling of the sample was achieved *via* a liquid nitrogen reservoir located inside the sample manipulator probe holding the Au(111) or Ag(111) single crystals. The temperature of the sample was measured using a K-type thermocouple attached on the lateral facet of the single crystals. Single crystals were atomically cleaned

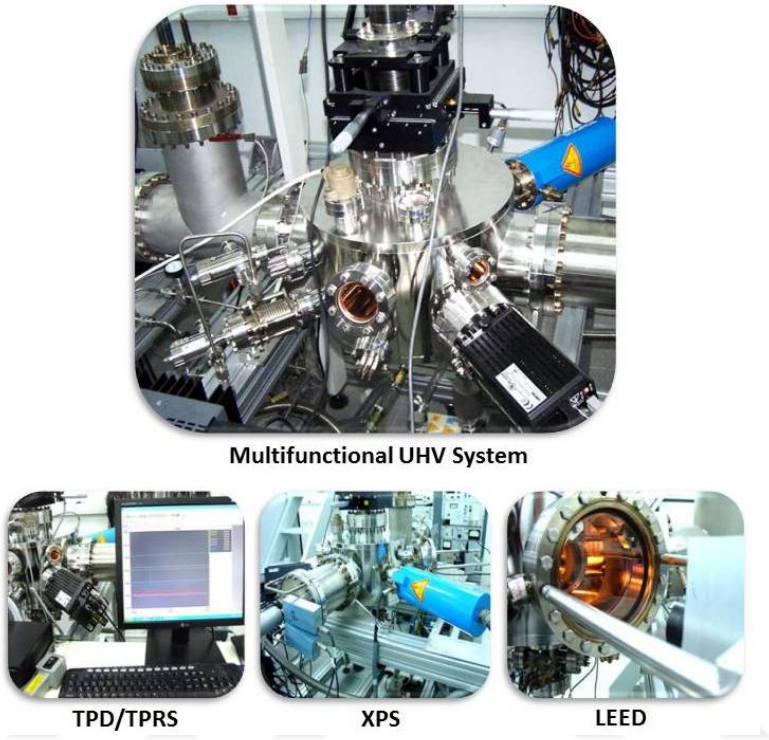

Figure 2.1: Pictures of the multicomponent UHV system

before the experiments by cycles of Ar^+ sputtering (Ar(g), Linde AG, purity $\geq$99.999%) with an ion gun (LK Technologies, Model NGI3000) at room temperature using an accelerating voltage of 1.5 kV with a filament current of 15 mA, which is followed by annealing at 773 K in UHV during 20 min.

2.1 Temperature Programmed Desorption/ Reaction Spectroscopy

Temperature Programmed Desorption (TPD) is a technique that provides kinetic and thermodynamic information about desorption processes of adsorbed atoms/molecules on a substrate [64]. In this technique, the substrate is linearly heated and the partial pressures of atoms/molecules desorbing from the surface are followed by mass spectrometry. When more than one species are adsorbed

on a substrate, this technique is called Temperature Programmed Reaction Spectroscopy (TPRS). The schematic setup for TPD experiments under UHV conditions were given in Figure 2.2. In the current work, PID-controlled linear sample heater (Heatwave, Model 101303) and a quadrupole mass spectrometer (QMS) (Ametek Dycor Dymaxion DM200) were used for the TPD/TPRS experiments. All of the TPD/TPRS experiments were performed with a heating rate of 1 K/s, 70 eV QMS beam energy and 30 ms dwell time for each desorption channel.

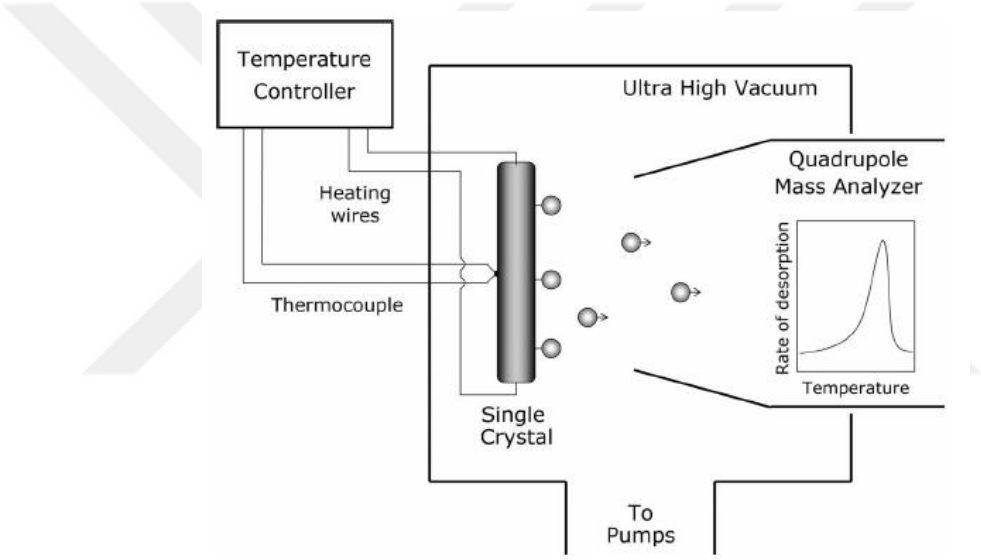

Figure 2.2: Schematic setup for TPD experiments under UHV conditions. Adapted from Ref. [65]

In TPD/TPRS experiments, shape of the partial pressure curve as a function of temperature contains information about desorption kinetics because the QMS signal is proportional to the rate of desorption if the pumping speed is large enough [66]. Equation 2.1 is the Polanyi-Wigner equation which indicates the relationship between desorption rate, desorption energy, desorption order and temperature [65].

$$r = -\frac{d\theta}{dt} = k_{des}\theta^n = \nu(\theta)\theta^n exp\left(-\frac{E_{des}(\theta)}{RT}\right) \tag{2.1}$$

$$T = T_o + \beta t \tag{2.2}$$

where r is the rate of desorption; θ is the adsorbate coverage in monolayers; t is the time; k_{des} is the reaction rate constant for desorption; n is the order of desorption; ν is the pre-exponential factor of desorption; E_{des} is the activation energy of desorption; R is the gas constant; T is the temperature; T_o is the temperature at which the experiment starts; β is the heating rate (*i.e.* dT/dt).

At very low temperatures, E_{des}>RT and no desorption occurs. E_{des}/RT ratio decreases with increasing temperature and desorption is observed in a certain temperature range. The desorption temperature of the atoms/molecules and the peak shape are affected by the desorption order. Representative TPD spectra for zeroth, first and second order desorption kinetics are given in Figure 2.3. Zeroth order desorption kinetics (n=0 in the Polanyi-Wigner equation) indicates that the desorption rate does not depend on coverage and increases exponentially with increasing temperature. As can be seen in Figure 2.3a, all signals with various coverages have a common leading edge with a rapid drop after desorption temperature maxima. In addition, peak positions shift to higher temperature with increasing coverage. Zeroth-order desorption is mostly observed in multilayer systems where the reservoir of the evolving molecules are practically infinite (*i.e.* in large excess).

First-order desorption kinetics (n=1) implies that the desorption rate is proportional to the coverage. TPD spectra exhibiting first-order desorption kinetics are given in Figure 2.3b. In this figure, the desorption maximum is constant at any coverage and all desorption signals have a characteristic asymmetric peak shape. First-order desorption behavior is common for atomic and non-dissociative adsorption/desorption of molecules in a reversible manner. In addition, for adsorbate overlayers following layer-by-layer growth mode, non-dissociative desorption intensities for sub-monolayer coverages converge to a saturation intensity where the surface of the substrate is fully covered with the adsorbate. This saturation point can be used to quantitatively determine the relative coverages of the other desorption curves [67]. In the second-order desorption kinetics, the desorption rate is proportional to θ^2 and as can be seen in Figure 2.3c, peak maximum shifts to lower temperatures as a function of adsorbate coverage. Recombinative desorption of atoms/molecules upon dissociative adsorption typically exhibits

second-order desorption kinetics [64].

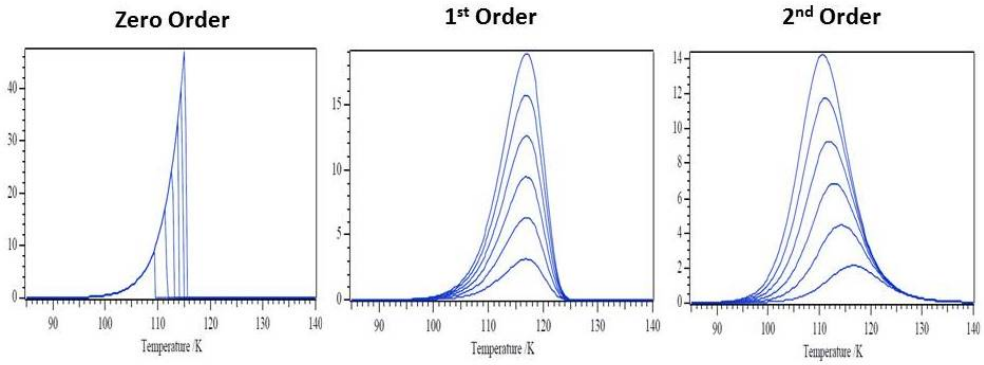

Figure 2.3: Representative TPD spectra for (a) zeroth, (b) first and (c) second order desorption kinetics. Adapted from Ref. [68]

TPD/TPRS techniques also provide thermodynamic information *e.g.* adsorption/desorption enthalpies. Although the kinetic parameters that are used to calculate the desorption enthalpy mostly depend on the surface coverage, thermodynamic information can be derived by making some assumptions [67]. For example, for the molecules that follow first-order desorption kinetics, Redhead analysis can be used to calculate desorption enthalpy of the adsorbate [69]. In this analysis, kinetic parameters are assumed to be coverage independent and the ratio of the pre-exponential factor to the heating rate (ν/β) is in between 10^8 - 10^{13} K^{-1} [65]. The pre-exponential factor is generally chosen as 10^{13} s^{-1} [65]. In the Redhead formula (Equation 2.3), the experimental peak maximum of the TPD signal is substituted with T_{max} and the desorption energy of the adsorbate is calculated.

$$E_{des} = RT_{max}\left[ln\left(\frac{\nu T_{max}}{\beta}\right) - 3.46\right] \tag{2.3}$$

Another way of the desorption energy calculation which allows the determination of the coverage and temperature dependent parameters is the Leading Edge analysis [70]. This method uses the Polanyi-Wigner equation given above. To keep the T and ν variation constant, a small fraction of the spectrum at the low temperature side is used and based on the logarithmic Polanyi-Wigner equation,

ln r is plotted vs. 1/T. After that, E_{des} can be determined from the slope this Arrhenius plot. This method uses the minimum number of assumptions however, the quality (*i.e.* signal to noise, S/N) of the spectrum must be extremely good to have accurate analysis [65].

2.2 X-ray Photoemission Spectroscopy

X-ray Photoelectron Spectroscopy (XPS) is a surface sensitive technique that is based on the photoelectric effect [65]. In this technique, electrons at different energy levels in solids are ejected *via* irradiation by x-rays and these electrons provide information on the atomic composition of the analyte and the oxidation states of the elements [71]. A diagram of the photoemission process is given in Figure 2.4a. In this process, photon with a known energy ($h\nu$) is absorbed by an electron in the core level of atom with a certain binding energy (E_b). This electron is ejected through the vacuum level with a certain kinetic energy (E_{kin}). The kinetic energy is measured by an electron analyzer and the binding energy of the electron can be calculated by using the Equation 2.4. In this equation, ϕ is the work function of the spectrometer.

$$E_b = h\nu - E_{kin} - \phi \tag{2.4}$$

Electrons have a certain traveling depth in a solid matrix depending on their kinetic energy. The average traveling distance of an electron between two inelastic collisions for a certain E_{kin} is called Inelastic Mean Free Path (IMFP) [71]. Since IMFP is less then 1-2 nm between the kinetic energy range of 10-1000 eV for a variety of metals, XPS is a surface sensitive method [71]. IMFP values of atomic solids plotted against E_{kin} of the electrons - which is also called the "universal curve" - is given in Figure 2.4b. As can be seen in this plot, the escape depth is the lowest at the kinetic energy of *ca.* 50-100 eV indicating electron detection from the outermost layer. It is agreed as a general rule that 95% of the detected electrons are coming from the thickness that three times the IMFP [71].

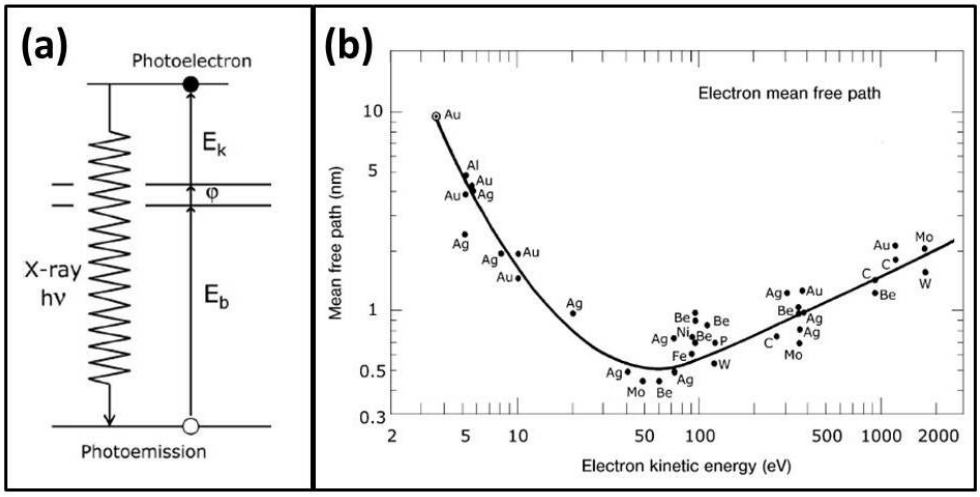

Figure 2.4: (a) Diagram of the photoemission process. (b) Universal curve that is plot of IMFP values of the metals as a function of the kinetic energy of electrons. Figures were adapted from Ref. [65]

Photoelectron signals are labeled according to the orbital (l) and spin (s) quantum numbers of core levels from which the electron emanates; the total quantum number (J=l+s) is also denoted as a subscript [65]. Since the spin quantum number may be either +1/2 or -1/2, each level for l>1 has two sub-levels and this phenomena is called spin-orbit splitting [65]. As an example, Au 4f has signals which are labeled as $4f_{7/2}$ (l=3, s=+1/2) and $4f_{5/2}$ (l=3, s=-1/2).

In a regular XP spectrometer, an x-ray tube is used as an x-ray source. A representative schematic is given in Figure 2.5a. In the current work, Riber (Model CX 700) source including Mg (hν=1253.6 eV, Full Width at Half Maximum, FWHM=0.70 eV) and Al (hν=1486.6 eV, FWHM=0.85 eV) dual anode was used. Anode materials were coated on a copper substrate because copper is a good thermal conductor which can be efficiently cooled with the water cooling system. Tungsten alloy filaments (Ø 180 μm) generating electrons for X-ray creation were located near the anodes. 200 W power (200 mA, 10kV) was used for electron emission from the filaments for all of the experiments. An aluminum sheet (1-2 μm thick) was used as an energy filter to remove satellite lines and the continuous radiation (the Bremmstrahlung). This aluminum filter absorbs 24% of Mg emission and 15% of Al emission.

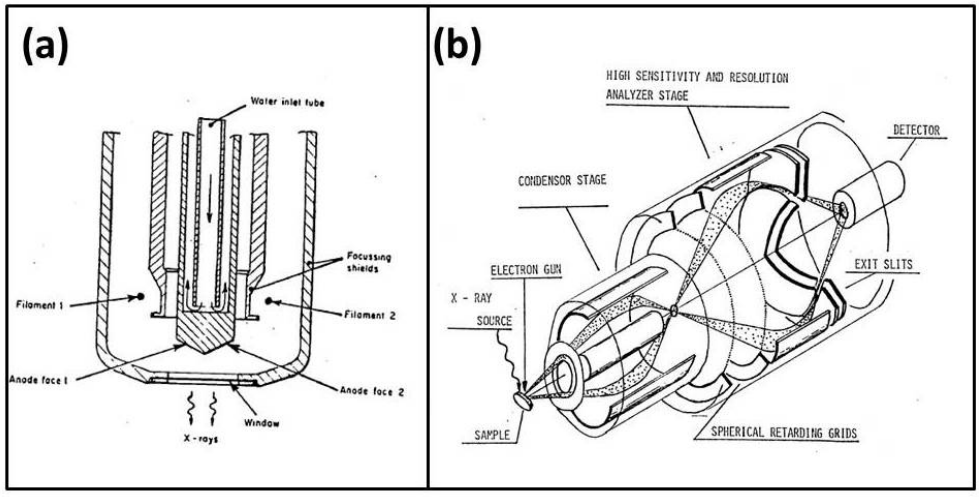

Figure 2.5: (a) A dual anode x-ray source configuration. Adapted from Ref. [72] (b) A double-pass cylindrical Mirror Energy Analyzer. Adapted from Ref. [73]

In the current XPS configuration, a double-pass cylindrical mirror analyzer (CMA) (Riber EA150) was used as an energy analyzer. CMA consists of two stages as given in Figure 2.5b. In the first stage (condenser), incoming electrons are focused to the entrance slit of the analyzer stage and it provides flexibility in the sample positioning ($\pm$ 3mm). Electrons coming from the entrance slit are retarded by the spherical grids and focused along the axis in the second stage. The energy resolution of the system depends on the voltage between the retarding grids and the inner cylinder (F_1). Then the beam is re-focused (F_2)through the exit slit to an electron multiplier. Resolution (F_1) and focusing (F_2) voltages were optimized in the current work for survey scan (1.0 eV spectrometer resolution) as F_1=27 V, F_2=50 V and for region scan (0.1 eV spectrometer resolution) as F_1=7 V, F_2=25 V.

2.3 Infrared Reflection Absorption Spectroscopy

Infrared Reflection Absorption Spectroscopy (IRAS) technique provides information regarding the adsorption site and/or geometry of the adsorbed molecules on a substrate as well as the concentration of the adsorbate with a high sensitivity

(1/1000 of a CO monolayer) [74].In addition, the high spectral resolution of IRAS (1-5 cm^{-1}) enables detection of the adsorbates which have similar vibrational frequencies in contrast to other vibrational techniques such as Electron Energy Loss Spectroscopy (EELS, typical resolution > 30 cm^{-1}) [74]. Besides, its broad working pressure range from UHV to atmosphere and its compatibility with a variety of surfaces make IRAS a widely used technique [74].

In this method, a collimated IR beam is reflected from the surface to be analyzed and collected by a detector. Electric field of incident infrared light has two components namely s-polarized and p-polarized lights which are perpendicular and parallel to the plane of incidence, respectively. These components interact with the metal electrons and a phase shift occurs on the metal surface depending on the angle of incidence (ϕ). Phase shifts of both components of light as a function of the angle of incidence are given in Figure 2.6a. As can be seen in this figure, s-component of the incident light shifts 180° for all angles that results destructive interference. Lack of the parallel component of electric field reveals a selection rule for conducting (*e.g.* metallic) surfaces that only the vibrational modes perpendicular to the surface can interact with the electric field. A schematic explanation of this phenomena is given in Figure 2.6b.

In contrast to the s-component, phase shift of the p-polarized light changes drastically with angle of incidence and the shift remains less than 90° between $0<\phi<85$. As an example, surface electric field of copper metal at a frequency of 2000 cm^{-1} as a function of ϕ is given in Figure 2.6c (dashed line). In addition, the intensity of absorption is proportional to the square of the surface electric field [74]. This function reaches a maximum at close to grazing incidence in Figure 2.6c (solid line). In order to increase the IRAS signal intensity, IRAS experiments are performed close to grazing angle of incidence.

In the current work, IRAS setup including source and detector compartments and an additional UHV chamber was designed and manufactured. Scaled-drawings of the IRAS chamber with all dimensions and a picture of the manufactured chamber are given in Figure 2.7. ConFlat (CF, Outer Diameter=8 in) flanges were attached to connect IRAS chamber to the main UHV chamber

and the manipulator. Barium Fluoride Mid-IR transparent view-ports (Hositrad Vacuum Technology, 2.75 CF flange, 38 mm view diameter) were included to the tubings (a) for the IR beam inlet and outlet. These tubings allow execution of IRAS experiments at 83^o angle of incidence. Two tubings (b) with 1.33 in CF flanges were centered directly to the sample position for reactant dosers. Additional 2.75 in CF flanges (c) together with glass view-ports were attached for visual monitoring purposes.

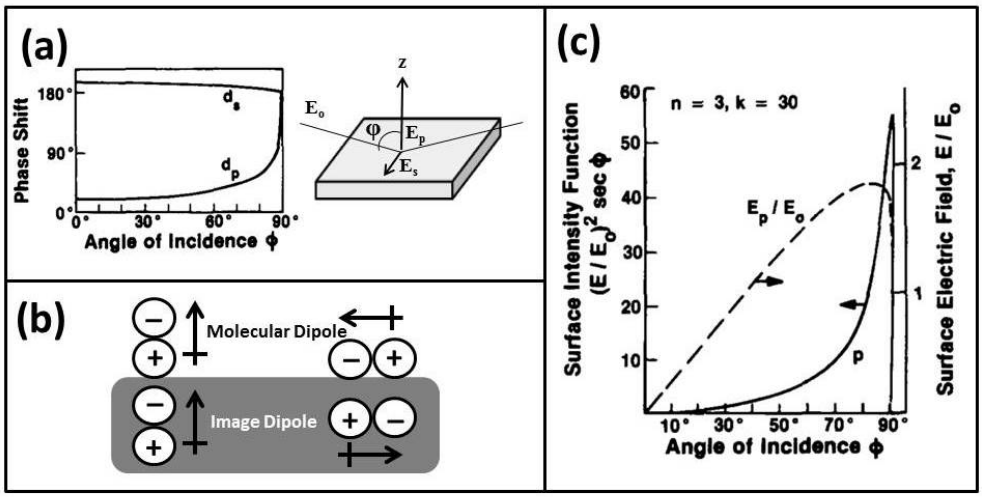

Figure 2.6: (a) Phase shifts of IR light components as a function of the angle of incidence on a metal surface. Adapted from Ref. [74]. (b) A schematic representation of dipole moments of a diatomic molecule located perpendicular and parallel to the metal surface and their image dipoles on the surface. (c) Electric field and intensity functions of p-polarized light in copper surface as a function of the angle of incidence. Adapted from Ref. [74]

.

Since the IR source and the detector are located outside of the UHV environment, the gas phase vibrational signals of the molecules in the air such as H_2O and CO_2 can readily obscure surface signals which are relatively lower in intensity. In order to avoid the interference from these background gases in the air, the IR beam path outside the UHV chamber must go through a controlled environment. This can be done either by pumping the air in the optics compartment outside the UHV chamber or by purging this compartment with an inert gas. Thus two separate Poly(methyl methacrylate) (PMMA) compartments for IR source and

the detector were designed and manufactured. These compartments were purged by using nitrogen gas (Linde AG, purity $\geq$ 99.99%). A Bruker FTIR Spectrometer (Tensor 37) was used and it was located in the spectrometer compartment. The IR radiation coming from the spectrometer as a parallel beam is focused on the sample located in the IRAS chamber by 90^o off-axis gold-coated Mid-IR parabolic mirrors (Thorlabs). IR beam reflected from the single crystal passed through the detector compartment and was focused onto a liquid nitrogen cooled Mercury-Cadmium-Tellurite (MCT) detector which is located on a two-axis stage. Description of the IRAS setup is given in Figure 2.8. In addition, a diagram showing the optics and the beam path is given in Appendix A. It is worth mentioning that - to the best of our knowledge - currently designed and manufactured UHV-IRAS setup is the first of its kind in Turkey. Along these lines, currently reported UHV-IRAS results constitute the first UHV-IRAS data obtained in Turkey from single crystal surfaces containing monolayer and multilayer adsorbate overlayers in UHV.

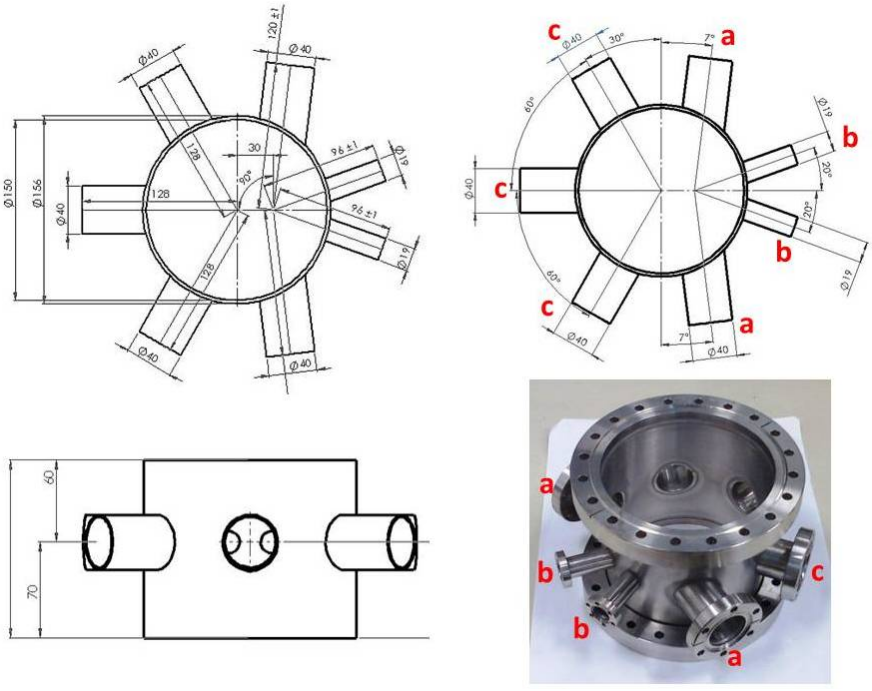

Figure 2.7: Scaled-drawings and final view of the IRAS chamber that was designed and manufactured in the current work

.

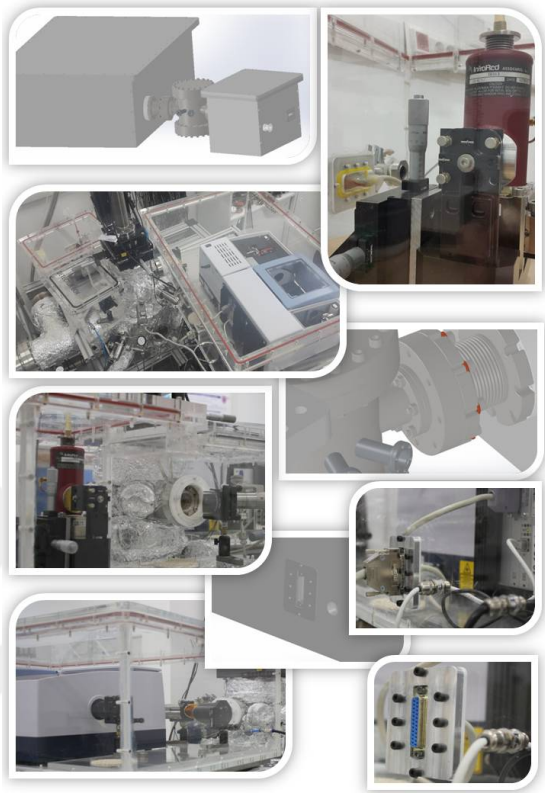

Figure 2.8: Scaled-drawings and final view of the IRAS setup that was designed and manufactured in the current work

.

In the current study, data acquisition details for the IRAS experiments were the following: ADC count rate=15000-18000, aperture size=6 mm, scanner velocity=10 kHz, resolution=4 cm^{-1}, number of sample scans=100. Background spectrum was taken before (R_1) and after (R_2) the adsorbate accumulation on a single crystal and the adsorbate spectrum was represented to be (R_1-R_2)/R_2 (*i.e.* $\Delta R/R$).

2.4 Low Energy Electron Diffraction

Low Energy Electron Diffraction (LEED) method provides structural information about the single crystal surfaces and ordered adsorbate layers [65]. Since the IMFP values of the electrons having energy in the range of 20-200 eV is only a few

Angstrom, diffracted electrons carry information only from the outermost layers [75]. Thus, LEED is a very convenient method to investigate surface structures of the single crystals. In this method, electrons are accelerated by an electron gun towards a single crystal surface and the beam of electrons scatters from the surface. Elastically scattered electrons show constructive interference due to the periodic order of the surface atoms when the Bragg condition given in Equation 2.5 is satisfied where, n is the order of diffraction, λ is the wavelength of the electrons, a is the distance between two atoms in the surface, α is the angle between the scattered electrons and the surface normal [65].

$$n\lambda = asin\alpha \tag{2.5}$$

When the scattered electrons are collected on a fluorescent screen, bright spots in each direction of the constructive interferences are observed. This set of bright spots forms the LEED pattern which is the scaled representation of the real surface pattern in the reciprocal (k) space. The real space unit cell vectors ($\bar{a}_i$) can be determined from the basis vectors in k-space ($\bar{a}_i{}^*$) by linear algebraic operations. The relationship between the k-space and real space basis vectors together with the constructive interference phenomena are summarized in Figure 2.9a.

Schematic of a LEED configuration is given in Figure 2.9b. Number of grids located between the sample and the screen varies with different configurations. Those grids are either grounded to minimize the electrostatic deflection of the electrons or negatively biased (*e.g.* suppressor grids) with respect to the gun potential to transmit only elastically scattered electrons. Besides, a few kV positive potential is applied to the fluorescent screen (2.0 kV in the current work) in order to collect electrons and make spots visible.

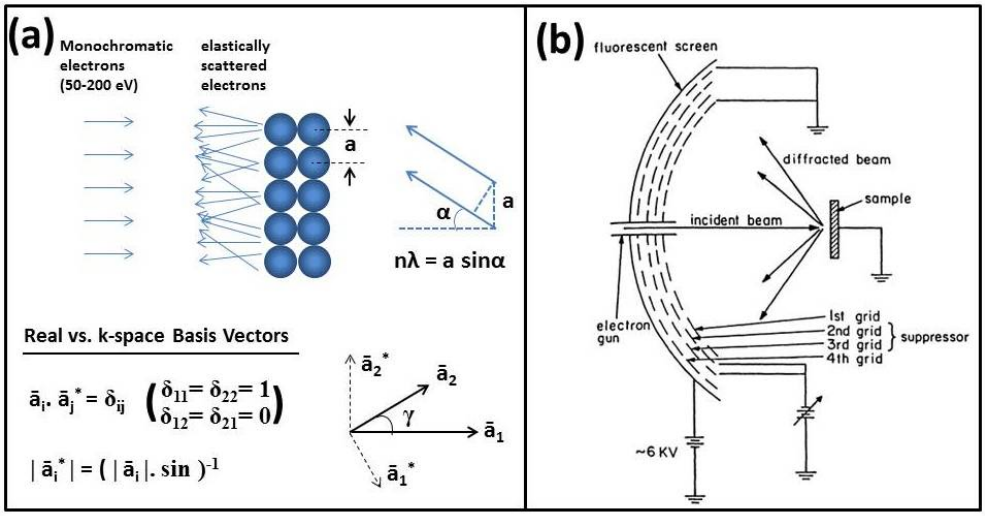

Figure 2.9: (a) Constructive interference phenomena and the relationship between the real space vs. k-space basis vectors in a LEED experiment. (b) A schematic of a LEED configuration. Adapted from Ref. [75]

2.5 Atomic Oxygen Accumulation Methods

Molecular oxygen does not dissociate neither on Au(111) [76] nor on Ag(111) [38] surface under UHV conditions. The dissociation probability of oxygen molecule is given in the literature as $< 10^{-6}$ and $\sim 5 \times 10^{-6}$ on the clean Au(111) [77] and Ag(111) [38] single crystals, respectively. There have been many efforts in the literature to create atomic oxygen under UHV conditions and different methods have been suggested such as thermal dissociation of gaseous O_2 on hot filaments [78], electron-induced chemisorption of oxygen [79], radio frequency-generated oxygen plasma [80], oxygen sputtering [81], co-adsorption of nitrogen oxides and water [82] and ozone decomposition [83]. Among these methods, NO_2 adsorption and ozone decomposition methods were used in the current work (further details are given in the subsections below). Ozone decomposition method was confirmed as the most efficient way of atomic oxygen accumulation as also mentioned in the literature [83].

2.5.1 NO_2 and water co-adsorption

In the current work, co-adsorption of NO_2/N_2O_4 and H_2O at 86 K with subsequent thermal desorption was initially utilized to deliver atomic oxygen species on Au(111). This method has been originally developed by Wang and Koel and described in the literature [82, 84, 85]. It should be noted that atomic oxygen layer cannot be formed by direct interaction of NO_2 with a gold surface. In this method, the heating of co-adsorbed NO_2 (or N_2O_4) and solid water to 400 K leads to the desorption of all species except atomic oxygen. Adsorbed atomic oxygen up to a surface coverage of 0.5 ML (ML= monolayer) can be reliably obtained *via* this method. Also this approach does not require high pressures of adsorbates. However, this method requires an NO_2 dosing system that can prevent NO_2 dissociation. Most of the conventional valve systems (*e.g.* high precision UHV leak valves) fail to provide intact NO_2 delivery and lead to the decomposition into NO and O_2. Thus, we have used a set of stainless steel (12 mm diameter) blank discs with microscopic pinholes in the center (*ca.* 5-40 μm in diameter). These microscopic pinholes were manufactured *via* a 250 mV pulse laser at Bilkent University Physics Department, Prof. Ö. İlday laboratory. The 5 μm pinhole disk was installed between the gas line and the UHV chamber. Use of this pinhole allows direct exposure of NO_2 without dissociation. Figure 2.10 illustrates the custom-made pinhole dosing system. Gas exposure can be regulated by manipulating upstream gas pressure before the pinhole (*i.e.* P_g). For the production of atomic oxygen, a second dosing line equipped with a conventional leak valve was utilized to dose H_2O(g).

With this method, different exposures of NO_2 could be delivered to the Au(111) surface. However, oxygen could not be detected in the TPD experiments. It is likely that during the transfer of NO_2 gas from the glass container to the dosing line, most of the NO_2 had been already decomposed before reaching the pinhole. Thus, another NO_2 delivery system was designed which utilized $Pb(NO_3)_2$, as the NO_2 source and was installed to the UHV system (Figure 2.11). This delivery system thermally decomposed the lead nitrate *via* resistive heating, generating nitrogen dioxide and oxygen gases. This design precludes extensive interaction

of NO_2 with the dosing lines and direct delivery on to the single crystal.

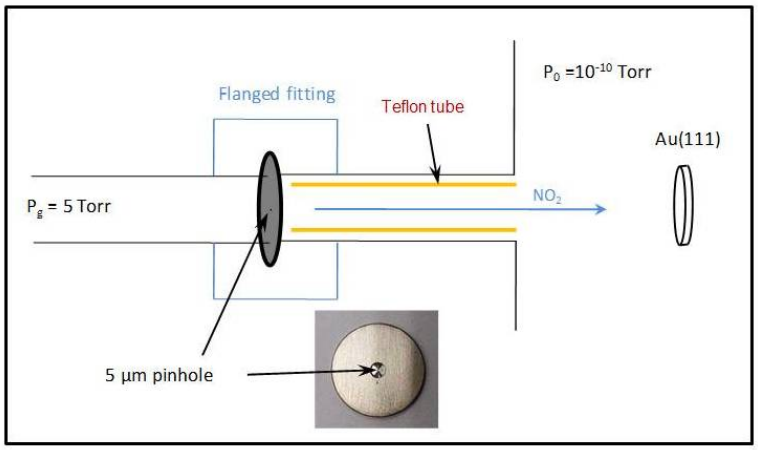

Figure 2.10: Custom-design NO_2 dosing line equipped with a stainless steel disc pinhole (Diameter = 5 μm).

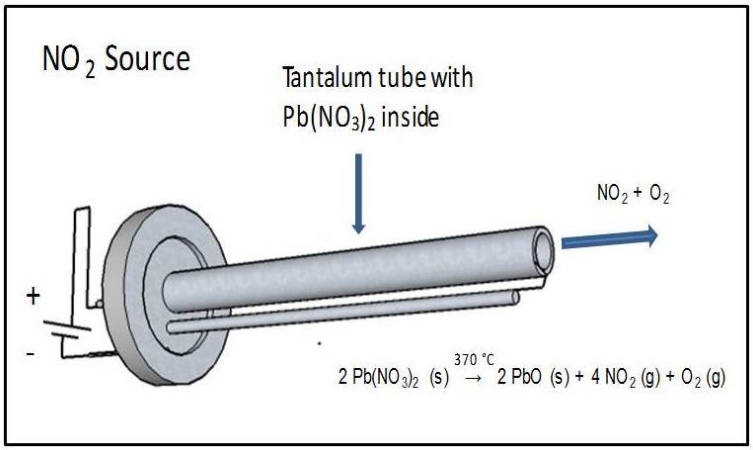

Figure 2.11: Schematic of the custom-made $Pb(NO_3)_2$(s)-based NO_2 delivery system.

The preliminary experiments showed that the doser design given in Figure 2.11 does not provide reliable quantity of oxygen atoms on the Au(111) surface. Furthermore, this design also led to unwanted Pb accumulation on the Au(111) surface. Hence, we focused on an alternative O_{ads}/Au(111) preparation method utilizing ozone adsorption whose details were given in the following subsection.

2.5.2 Ozone Decomposition

As mentioned previously, ozone decomposition method is widely utilized for preparation of O_{ads}/Au surfaces due to its high effectiveness. Furthermore, it eliminates the necessity to cool the single crystal sample to liquid nitrogen temperature and the O_{ads} layer can be prepared at/above room temperature. However there are some difficulties in using this method. Ozone is produced via atmospheric pressure of oxygen which cannot be directly dosed to the UHV system. Therefore, an ozone pre-concentrator was designed and manufactured where ozone is first accumulated in a silica gel trap at dry ice temperature (-78 °C). Note that while ozone could be captured and stored in/on the silica gel, O_2 did not adsorb onto the silica gel. Then, after evacuation of the excess oxygen, the trap is carefully heated to desorb ozone and ozone is dosed into the UHV system. It should be noted that ozone desorption from silica gel is a very rapid process and care must be taken to prevent explosion due to the rapid pressure rise in the trap. A custom-made corona discharge ozonizer was modified with the silica gel ozone trap system which was connected to UHV system through a pinhole dosing line (Figure 2.12). The ozone in the ozonizer was produced by generating oxygen plasma using a high voltage (6 kV) bias on platinum pins at high oxygen pressure (∼700 Torr).

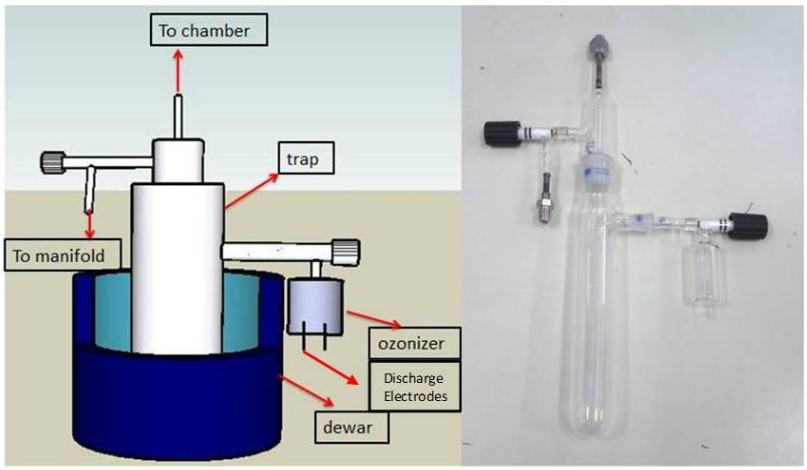

Figure 2.12: Details of the custom-made ozonizer and ozone trap accommodating the silica gel.

When the silica gel particles absorb ozone molecules, color of the silica gel changes from white to violet (Figure 2.13). However, the amount of produced ozone in the corona discharge cell was not sufficient for the observation of this color change. Thus, a commercial ozone generator (Genozon, GN-Q1001S) was used to produce sufficient ozone that can be stored in the trap. The images of the commercial ozone generator (a), ozone trap before (b) and after (c) ozone accumulation are shown in Figure 2.13. Moreover, Teflon tubing was used for transferring ozone to the leak valve instead of stainless steel tubing in order to prevent ozone decomposition along the dosing pipeline. Different flow rates and ozone trapping times have been used for the optimization. After the optimization, oxygen (99.999% purity, Linde AG) was passed with a flow rate of 1 L/min through the ozone generator connected to the ozone trap by Teflon tubing. The trap was filled with dried silica gel (grain size = ~2 mm) and cooled with a slurry of ethanol and dry ice (-78 °C). After 5 min of O_3+O_2 flow through the trap at atmospheric pressure, silica gel particles changed their color from white to violet. Then, the trap was evacuated to 10^{-3} Torr to remove O_2. Next, absorbed ozone was removed from the trap by heating before dosage to the UHV system.

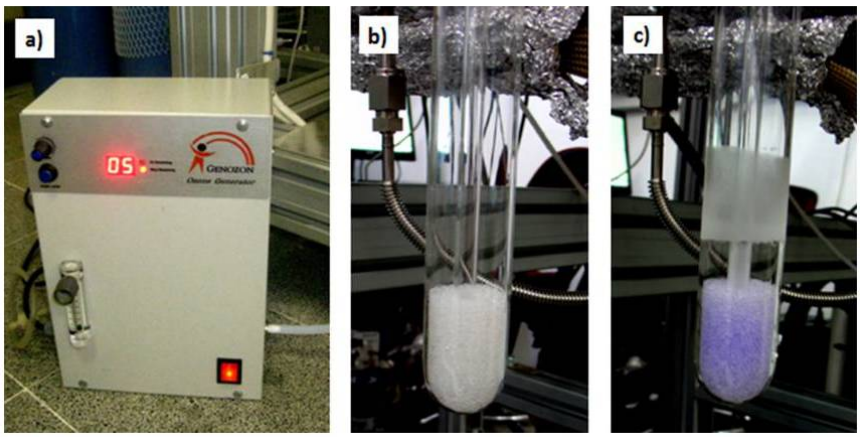

Figure 2.13: (a) Commercial ozone generator, ozone trap (b) before and (c) after ozone storage.

Chapter 3

Bond Activation on Gold

3.1 Characterization of the Au(111) Single Crystal Surface

Some metals exhibit rearrangement in their surface atoms under UHV conditions to further decrease the surface free energy such as *e.g.* W(100), Mo(100), Ir(100) [2] and Au(111). Gold is the only fcc metal whose (111) facet exhibits reconstruction under UHV conditions [86]. The reconstruction of Au(111) surface has been investigated by numerous methods such as Low Energy Electron Diffraction (LEED) [87], Helium Atom Diffraction (HAD) [88], Scanning Tunneling Microscopy (STM) [86, 89], and DFT calculations [90]. Reconstructed Au(111) surface has a $22\times\sqrt{3}$ surface unit cell structure and it is thought to originate from dislocated low-coordination surface atoms which tend to maximize

their coordination [89]. Due to the contraction/dislocation of surface atoms, the unit cell contains 23 atoms instead of 22 atoms. Thus, partial dislocations are periodically formed because of the mismatching epitaxy of surface atoms and the sublayer. These dislocation domains create hills with a height of 0.1-0.2 Å to decrease the stress on the surface and so, a zigzag pattern which is called the "herringbone structure" is formed [89]. Schematic drawing of the reconstructed Au(111) unit cell and an STM image of the herringbone structure are shown in Figure 3.1.

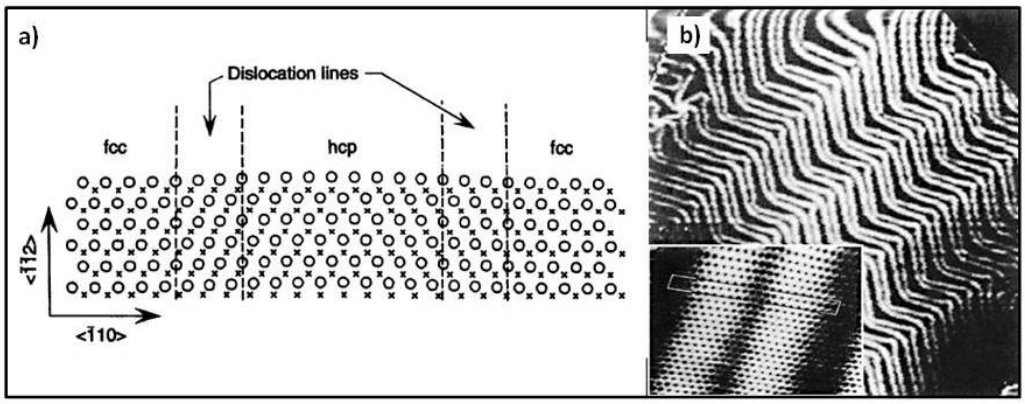

Figure 3.1: Reconstructed Au(111) unit cell [89]. b) STM image of a reconstructed Au(111) surface (size 120×120 nm^2) in UHV. Inset shows an atomic resolution image (8×6 nm^2) where the unit cell is marked with a rectangle. Adapted from Ref. [91]

Au(111) surface was atomically cleaned by multiple cycles of Ar^+ sputtering, followed by subsequent annealing at 773 K under UHV conditions. The cleanness of the surface was confirmed by XPS. Trace amount of argon, sulfur and carbon atoms (*i.e.* natural contaminations in gold ores) were detected together with gold signals before the cleaning procedure. Sputtering-annealing cycle was repeated until the impurities dropped below detection limits. A representative survey scan of the clean Au(111) single crystal after Ar^+ sputtering and annealing cycles is shown in Figure 3.2. As can be seen in Figure 3.2, all photoemission signals belong to the gold sample and no contamination exists on the Au(111) single crystal.

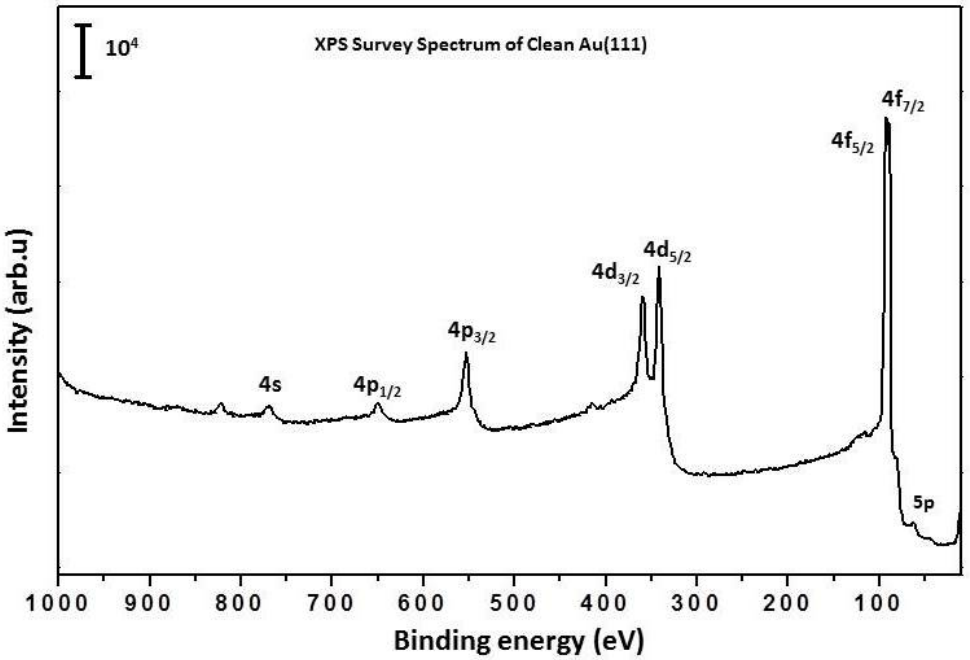

Figure 3.2: A representative survey XP spectrum of the clean Au(111) single crystal.

In order to determine the chemical states of gold atoms, Au *4f* region was also analyzed by XPS and the spectrum is given in Figure 3.3a. Au $4f_{7/2}$ signal was found to be located at 84.0 eV indicating metallic state of gold atoms (*i.e.* Au^0) [92]. In addition to the impurity and the chemical state analysis of the Au(111) surface by XPS, atomic level crystallographic orientation of the Au (111) single crystal surface was also confirmed by LEED. Hexagonal (1×1) crystal pattern was obtained from the clean Au(111) single crystal surface and the LEED image is shown in Figure 3.3b. In this pattern, the spots on the fluorescent screen were dispersed. This is the characteristic pattern of the Au(111) single crystal surface and caused by the herringbone reconstruction of the Au(111) surface which was mentioned above.

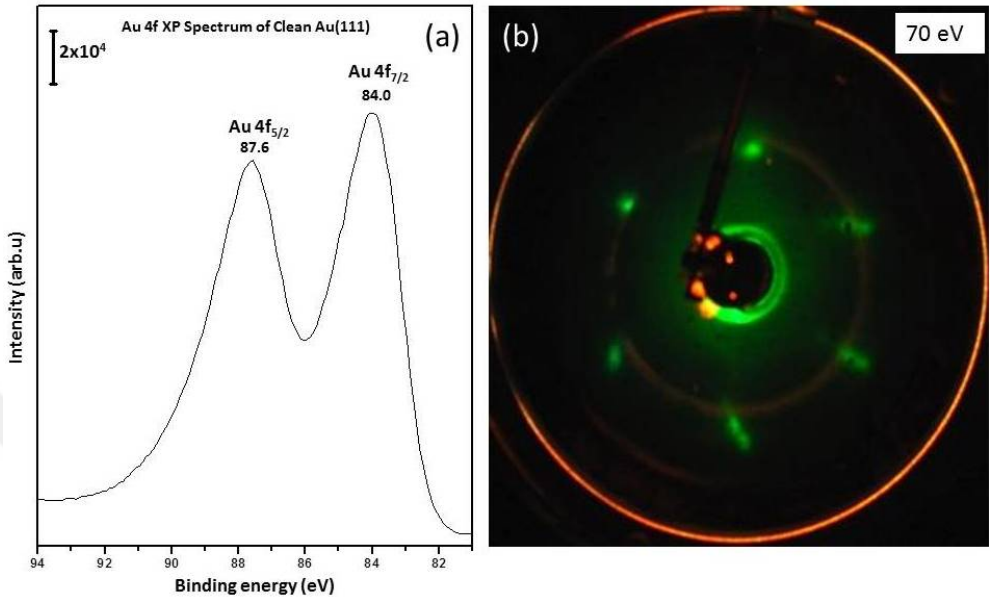

Figure 3.3: (a) Au *4f* XP spectrum (b) LEED pattern of the clean Au(111) single crystal.

3.2 Oxygen Behavior on Au(111) Single Crystal

In order to understand the nature of oxygen on Au(111), TPD experiments of oxygen layers prepared at various temperatures were performed. TPD spectra showing m/z=32 (O_2) with increasing ozone exposure at 460 K (a), 300 K (b) and 140 K (c) are given in Figure 3.4. In the literature, Saliba *et al.* performed similar TPD experiments of oxygen *via* ozone adsorption on the Au(111) surface at 300 K [93]. They concluded that oxygen desorption follows first-order kinetics. In the following works (whatever temperature and atomic oxygen preparation method was utilized), researchers associated the oxygen desorption with first order or pseudo-first order kinetics even though the TPD spectra does not fit the first-order kinetics [77]. The observed inconsistencies in TPD spectra with first-order behavior were associated with restructuring and corrugation of the surface which is indeed confirmed by STM [23].

In the current work, oxygen TPD spectra of the oxygen layers prepared at 460 K (Figure 3.4a) reveal a common leading edge of the spectral curves with

increasing temperature. The spectra also show a sharp decline at the end of desorption. Furthermore, the spectra do not converge to a saturation coverage; O_2 desorption signal continuously grows with ozone exposure. This behavior unambiguously indicates zero-order desorption kinetics. Similar O_2 TPD spectra were reported by Gong *et al.* for atomic oxygen layers prepared at 77 K using a radio frequency generated plasma jet [94]. Zero-order desorption kinetics can be expected when the reservoir of desorbing molecules is infinite, as in the case of multilayer desorption. The possible suggested structures of the oxygen layers that can lead to zero-order O_2 desorption are 1) bulk gold oxide (O_{bulk}); the decomposition rate of which does not depend on oxygen content and 2) subsurface atomic oxygen (O_{sub}) dissolved into the bulk of gold single crystal. No oxide formation was detected by XPS at 460 K (discussed below) and it was deduced that oxygen dissolves into the bulk when it is accumulated at 460 K temperature. Former studies in the literature support our discussion. Min *et al.* showed that CO oxidation rate decreases when ozone exposure temperature increases from 200 K to 400 K [23]. In their study, bigger oxygen island formation on the Au(111) surface at 400 K compared to 200 K was demonstrated by STM; and the presence of the inaccessible oxygen atoms dissolving in big islands at higher temperature and decrease of the reaction rate were reported. Parker *et al.* also mentioned that CO oxidation rate increases when the surface temperature decreases [83]. In another study, Sault *et al.* prepared atomic oxygen on Au(110)-(1×2) surface at room temperature (RT) by using hot filament and found 10% of remained oxygen after high pressure H_2 titration at 400 K [95].

The desorption behavior is different for oxygen layers prepared at 300 K (Figure 3.4b) and 140 K on Au(111) (Figure 3.4c). Saturation coverage was reached when the oxygen layer was prepared at 140 K. Very similar TPD spectra (top two spectra in Figure 3.4c) were observed which were individually exposed to 0.8 L and 2.4 L of ozone. Saturation coverage was also observed by Wang *et al.* on Au(111) by NO_2+H_2O co-adsorption method for atomic oxygen accumulation at 86 K [82]. Starting from the lowest coverage in Figure 3.4c, intensity of the desorption signal continuously increases and its maximum shifts to higher temperatures. After a certain exposure (the fifth spectrum from bottom), the peak

maximum suddenly shifts to lower temperature and becomes broader indicating appearance of a new desorption state. The peak maximum monotonically shifts to higher temperature with further oxygen accumulation until it reaches the saturation. Similar TPD spectra with a steep shift of maximum were reported by Davis *et al.* for oxygen on Au(111) that were prepared by O_2 splitting on a glowing filament [96]. Gong *et al.* also presented very similar oxygen TPD results from the Au(111) single crystal by using another oxygen accumulation method which is RF plazma [97]. It is interesting that the maximum of the chemisorbed oxygen desorption signal starting from low oxygen coverage monotonically shifts to higher temperature, while recombinative second-order O_2 desorption shows a shift towards lower temperatures. This second shift might be related to the surface islands of oxygen which are known to form, for example, on Al(111) and Pt (111) surfaces [98, 99, 100]. In accordance with the literature work, the desorption signals in Figure 3.4c before the sudden shift are suggested to result from the recombinative desorption of surface atomic oxygen (O_a).

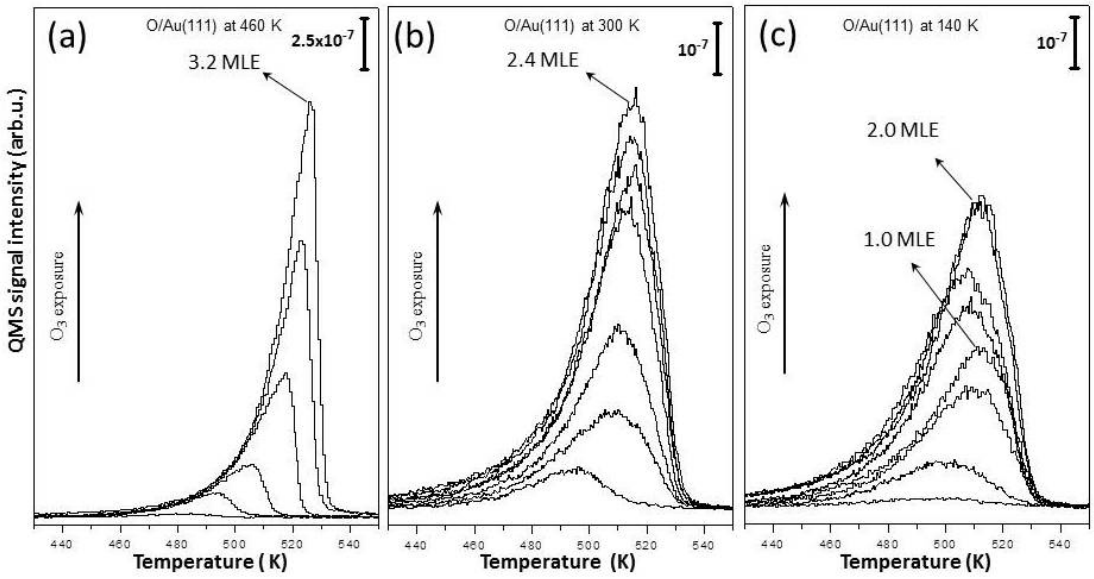

Figure 3.4: O_2 TPD profiles with increasing coverage of atomic oxygen on Au(111) prepared via ozone decomposition at 460 K (a), 300 K (b) and 140 K (c).

Subsequently appeared state at 507 K after the fifth spectrum in Figure 3.4c for high oxygen coverage is attributed to 2D gold oxide overlayer (O_{ox}). Former studies in the literature support this assignment. It was known that oxygen

atoms locate on Au(111) surface at 3-fold position for low coverages [33, 24]. However, a new vibrational feature in HREELS spectrum was reported for high oxygen coverage by Baker *et al.* and it was concluded that 2D gold oxide layer was formed [24] for high oxygen accumulation. In another study, Gottfried *et al.* showed that oxygen originating from gold oxide decomposition had lower desorption temperature compared to the chemisorbed atomic oxygen [101]. In contrast to the current study, TPD signals of the gold oxide and atomic oxygen were well separated in Gottfried's work. It must however be considered that a different gold single crystal surface, Au(110)-(1×2), and a different heating rate were used in their work.

DFT studies in the literature support the surface gold oxide (O_{ox}) assignment in the current work as well. Miller *et al.* found that d-band densities of states for surface gold atoms increase with increasing oxygen coverage, which means increased overlap of oxygen and surface gold orbitals [102]. Baker *et al.* argued that release of gold atoms from the surface is favorable at high oxygen coverages, where Au-O bond becomes stronger [33]. In another study, Baker *et al.* calculated charges on the oxygen atoms at different coverages and found more covalent Au-O interaction with increasing coverage [31]. It must be considered as an alternative explanation that desorption temperature shift may also be related to the changing surface structure with increasing oxygen quantity which is shown by STM [23]. Goodman's work shows that oxygen desorption features are completely different on Au(110) and Au(111) surfaces; peak positions are 470 K and 535 K, respectively [96].

In Figure 3.4c, the integrated peak area of the signal where the saturation was reached and that of the signal before shifting (fourth spectrum from bottom in Figure 3.4c) were calculated. The ratio between the integrated areas of these signals was found to be precisely 2:1. This ratio is in agreement with the model where the concentration of oxygen atoms in 2D gold oxide layer (O_{ox}) is double of that in fully covered surface atomic oxygen layer. In our oxygen coverage calculations, integrated area of the signal belonging to fully covered surface atomic oxygen (fourth spectrum from bottom in the Figure 3.4c) was assumed to be 1.0 MLE and taken as a reference for oxygen coverage in other TPD experiments.

Therefore the saturation coverage in the corresponding figure was determined to be 2.0 MLE.

Figure 3.4b presents the TPD spectra of oxygen prepared by ozone accumulation at 300 K. Oxygen desorption behavior in Figure 3.4b was very close to the Koel's work in the literature that oxygen was accumulated by ozone exposure at 300 K [93]. In their study, the behavior of TPD spectra were assigned to first-order desorption kinetics. However,it is difficult to assign this behavior directly to first-order desorption kinetics. The maximum of the peaks monotonically shifts to higher temperatures with increasing oxygen coverage. In the current study, the saturation coverage was not observed in contrast to the literature work, however the rate of adsorption at high coverages significantly decreases. These spectra in the current study were tentatively associated with a desorption state which demonstrates zero-order kinetics for the O/Au(111) layers prepared at 460 K and a second desorption state with peak maximum at 515 K which was related to the surface atomic oxygen (O_a).

Figure 3.5 represents Au *4f* XP spectra of Au(111) single crystal including 2.0 MLE oxygen layers that were prepared at corresponding temperatures in comparison to the Au *4f* spectrum of the clean Au(111) surface. For oxygen layers prepared at 460 K and 300 K (Figure 3.5a and b), no sufficient difference is observed in the Au *4f* spectra between clean and oxygen containing surfaces and gold was only found in metallic state. Therefore, oxygen that was accumulated at elevated temperature (460 K), which followed zero-order desorption kinetics in Figure 3.4a, can be associated with atomic oxygen dissolved in the bulk of gold single crystal. However, the monitored XP spectra cannot absolutely prove the absence of gold oxide 3D gold oxide agglomerates which are difficult to detect with XPS method due to the experimental detection limits. When the saturated oxygen overlayer was prepared at 140 K, FWHM of Au *4f* signal slightly increased as can be seen in Figure 3.5c compared to the spectrum of the clean Au(111). Subtraction of these signals from each other indicates the existence of oxidized gold atoms.

Gold oxide formation was also previously reported in the literature. Koslowski

et al. oxidized gold film by RF oxygen plasma at high pressure and estimated the thickness of the film to be about 4 nm [103]. When they performed angle resolved XPS analysis of Au *4f* region, detected oxide signal was intense at 60° but it was very small at 0° compared to metallic gold even for 4 nm thick oxide layer. In another study, Schlögl and co-workers oxidized gold foil by ozone and analyzed the surface with high pressure XPS during ozone flow [28]. They also revealed the formation of 2D gold oxide (O_{ox}) and assigned Au $4f_{7/2}$ oxide signal as 85.2 eV which coincides with the current findings. When they heated the sample, gold oxide decomposed after 523 K even the sample was under ozone flux. A DFT work reveals that surface oxide (O_{ox}) can be stable at 200-420 K at 1 atm, however oxide structure can only be stable below 200 K under UHV conditions [104]. This study explains the lack of gold oxide formation in the current work at 300 K and 460 K. In addition, Friend and co-workers calculated energy barriers for surface and subsurface oxide formation and revealed that it is less than 0.1 eV for surface oxide while it is 0.8-1.4 eV for the formation of subsurface oxide (*i.e.* surface oxide formation is energetically favorable rather than bulk oxide formation) [24].

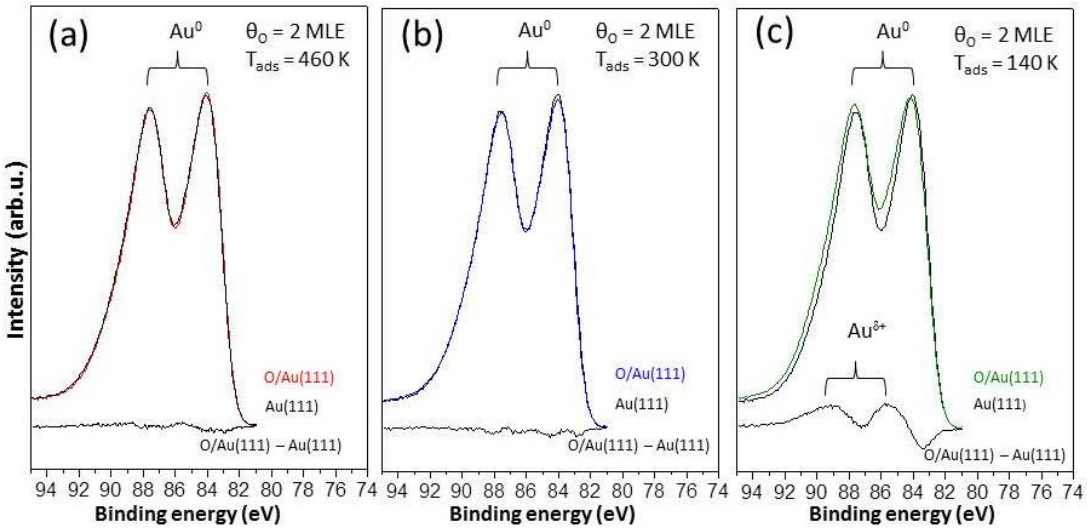

Figure 3.5: Au *4f* region XP spectra of high coverage oxygen layers (θ_O = 2 MLE) on Au(111) prepared at 460 K (a), 300 K (b) and 140 K (c) in comparison to the clean Au(111) single crystal.

It is worth mentioning that gold oxide could not be detected for 0.8 MLE

oxygen covered Au(111) surface at 140 K. Au *4f* XP spectrum for 0.8 MLE of oxygen covered Au(111) single crystal and for the clean Au(111) are given in Figure 3.6. This is in agreement with the suggestion that gold oxide emanates only after 1 MLE oxygen coverage with the appearance of the new desorption state in Figure 3.4c.

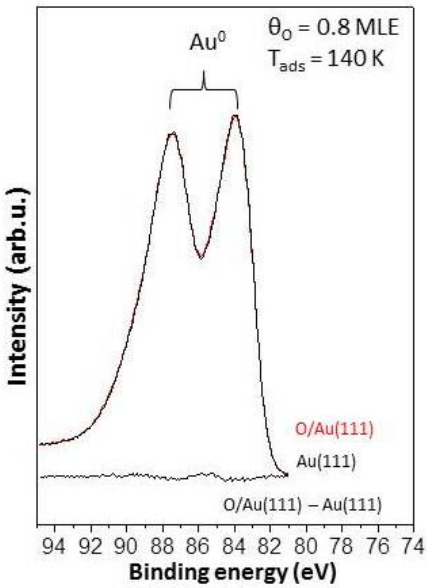

Figure 3.6: Au4f region XP spectra of Au(111) including 0.8 MLE oxygen overlayer prepared at 140 K in comparison to Au *4f* spectrum of clean Au(111) surface.

Chemisorbed atomic oxygen overlayer prepared at low temperature and low oxygen coverage, which is denoted as O_a in the current study, attracts interest due to its high activity (*e.g.* towards CO [23]) and selectivity in oxidative coupling reactions [22]. Thus, we focused on such oxygen overlayers in the current work in depth. O *1s* XP spectra of the oxygen overlayers with various coverages prepared at 140 K are presented in Figure 3.7. At low oxygen coverage, the O *1s* signal demonstrated asymmetry establishing the presence of at least two different oxygen species in the overlayer. The O *1s* spectra of 0.5 MLE and 0.9 MLE oxygen overlayers can be deconvoluted in two symmetric (Gaussian + Lorentzian) peaks with binding energy maxima at 529.5 eV and 531.3 eV binding energies. The saturated 2.0 MLE overlayer prepared at 140 K revealed a broad peak with maximum at 530.6 eV which can be associated with surface gold oxide

(O_{ox}). Binding energy of gold oxide O *1s* signal was reported in the literature within the range of 530.0-530.2 eV [26, 81, 103, 105]. According to the former studies, the peak at 529.5 eV can be associated with oxygen atoms located on the gold surface (O_a), while the assignment of the shoulder at higher binding energy (531.3 eV) remained unclear [23, 26, 27, 28, 106]. This signal at 531.3 eV cannot be associated with gold oxide since oxide formation could not be detected in Au *4f* spectra at low oxygen coverages. It cannot be also associated with adsorbed residual water from background since the O *1s* signal of the adsorbed water is expected around 533 eV [92]. In addition, water is not stable on the gold surface at 300 K and this signal remains almost unchanged when the sample was heated to 300 K. It can be associated with surface OH species, however OH species are not expected to be stable on the gold metal surface at 300 K. Nevertheless this possibility cannot be completely excluded.

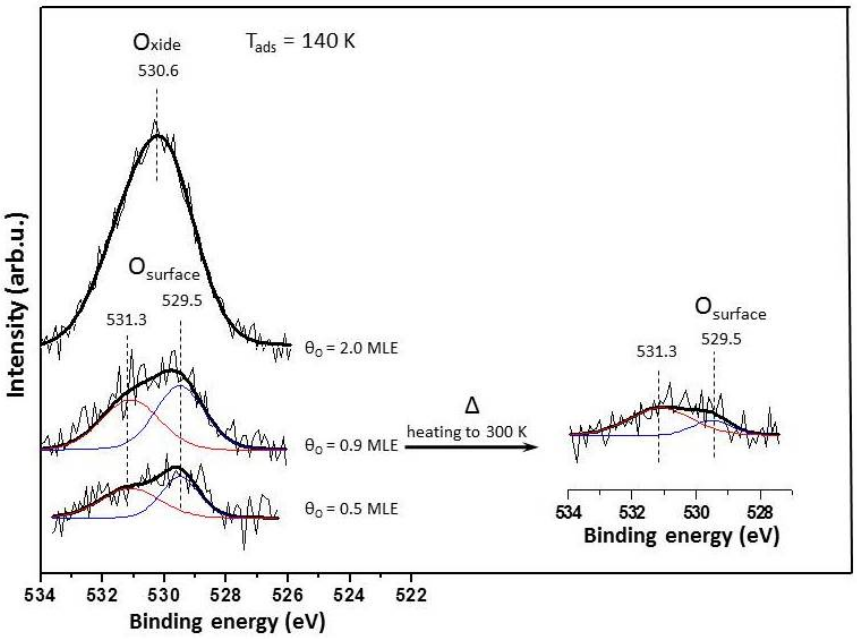

Figure 3.7: O *1s* XP spectra of the oxygen overlayers on Au(111) prepared and monitored at 140 K. The right panel shows the O *1s* spectrum recorded after heating of the 0.9 MLE oxygen layer to 300 K (the spectrum was acquired at 300 K).

After having heated 0.9 MLE O/Au(111) surface to 300 K, the total O *1s* signal became less intense. The peak at 531.3 eV is slightly suppressed while the peak at

529.5 eV was suppressed by around 80%. One can see from the TPD experiments that at temperature below 300 K oxygen does not desorb from the Au(111) surface (see Figure 3.4). Therefore it is logical to suggest the diffusion of oxygen atoms into the bulk of the Au(111) single crystal. Besides, the O *1s* component at higher binding energy (531.3 eV) is tentatively attributed to subsurface atomic oxygen (O_{sub}). This assignment is in agreement with theoretical calculations of oxygen atoms on Al(111) surface, where it was shown that oxygen atoms in 3-fold site below the surface have higher O *1s* BE than oxygen atoms above the surface [99].

3.2.1 Examination of the Activity of Oxygen Overlayers on Au(111) by Titration with CO Molecules

In order to determine the activity of the oxygen overlayers that were prepared at three different temperatures, CO was used as a probe molecule to titrate oxygen atoms. Since CO interacts with atomic oxygen on the Au(111) surface already at 77 K, the activity of the oxygen overlayers was examined in the following way: oxygen overlayers were prepared at various temperatures (the estimated oxygen coverage was $\theta_O = 0.7$ MLE) and followed by CO accumulation at relatively high exposure (3.0 L) at 140 K to remove all of the active oxygen. The subsequent TPD (m/z=32 channel) spectra of unreacted oxygen are presented in Figure 3.8 in comparison to the spectra of the oxygen overlayers without CO treatment. One can see that the quantity of inactive oxygen strongly depended on the oxygen overlayer preparation temperature and increased with the increasing temperature.

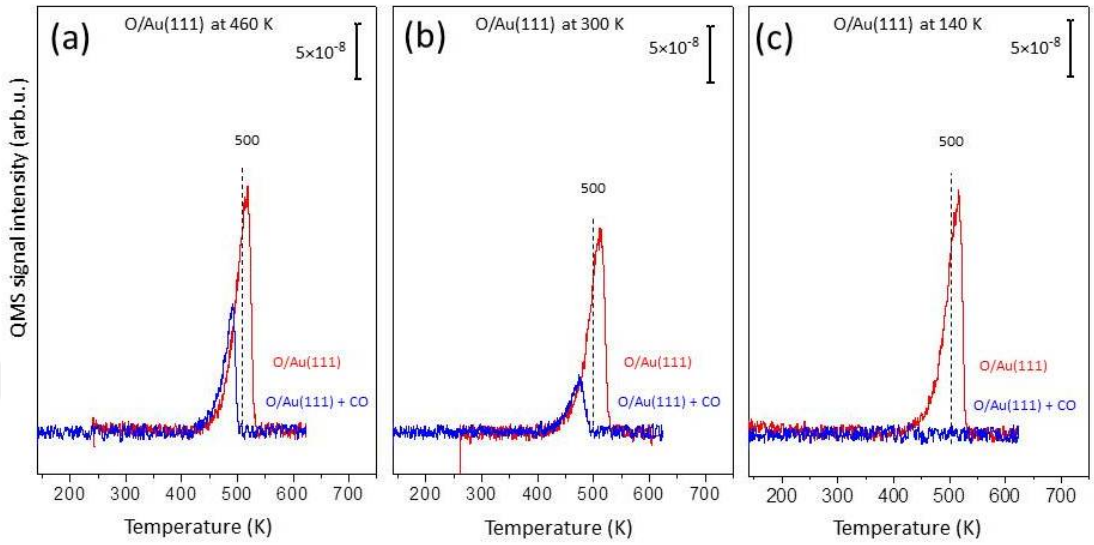

Figure 3.8: TPD profiles of O/Au(111) overlayers before and after reaction with CO. TPD profiles showing m/z=32 desorption channel for oxygen recorded after ∼0.7 MLE of oxygen accumulation at (a) 460 K, (b) 300 K and (c) 140 K (red spectra) and spectra monitored after subsequent 3.0 L of CO exposure (10^{-8} Torr × 5 min.) on the analogous O/Au(111) overlayers at 140 K (blue spectra).

3.3 C-H and O-H Activation on Au(111) Single Crystal

In order to determine the reactivity of oxygen overlayers towards C-H and O-H bond activation, oxygen was accumulated at three different temperatures (as mentioned in Section 3.2) and methanol was used as a probe molecule. Methanol oxidation reactions were performed at different temperatures individually on oxygen pre-covered Au(111) surface. Before the methanol oxidation reactions, desorption behavior and molecular orientation of methanol molecules on the clean Au(111) single crystal surface without oxygen layers were determined.

3.3.1 Methanol on Clean Au(111) Single Crystal

Methanol adsorption was carried out on the clean Au(111) surface at 90 K and m/z=31 signal which corresponds to the most intense fragment in the mass spectrum of gas-phase methanol was monitored in TPD experiments. Fragmentation pattern of methanol during Residual Gas Analysis (RGA) is given in Appendix B. In all of the TPD experiments, methanol was found to desorb molecularly in a reversible manner from the clean Au(111) single crystal surface. TPD spectra of m/z=31 signal as a function of methanol exposure are given in Figure 3.9. In Figure 3.9, desorption maximum located at ∼155 K was observed for the lowest methanol coverage of $\theta_{methanol}$ = 0.1 MLE. With increasing methanol coverage, the major methanol desorption feature at 155 K almost reached saturation which was immediately followed by the appearance of an additional desorption maximum at 140 K that can be assigned to the formation of multilayer methanol overlayers. This signal (fourth spectrum from the bottom) was used to estimate the relative methanol coverages. For this purpose, the multilayer signal at 140 K was deconvoluted and subtracted from the whole desorption spectrum and the integrated desorption signal between 100 K and 500 K associated with the desorption maximum at 155 K was used to estimate $\theta_{methanol} = 1$ MLE. With increasing methanol coverage, amorphous (α_2) and crystalline (α_1) methanol multilayers appeared at 142 and 137 K; respectively. Weak and broad features at *ca.* 170 K and 210 K which were more pronounced at higher methanol coverages ($\theta_{methanol} \geq 3.8$ MLE) can be associated with strongly bonded methanol species on coordinately unsaturated points and extended defects on the Au(111) single crystal surface. The methanol TPD spectra in Figure 3.9 are in very good agreement with the literature [107].

IRAS spectra of methanol on the clean Au(111) surface (at high exposures corresponding to $\theta_{methanol} > 1.0$ MLE) at 90 K and 140 K are shown in Figure 3.10. At 140 K, saturated chemisorbed monolayer of methanol is expected to be formed while at 90 K, multilayer methanol is formed. Signal assignments are in a good agreement with the literature for methanol on Au(111) [108] and Cu(110) [109]. The characteristic ν(CO) band at 1031 cm^{-1} is observed at 140 K while

this signal shifts to 1043 cm^{-1} at 90 K for multilayer coverages. This indicates vertical or bent C-O bond geometry of the methanol molecule at both monolayer and multilayer coverages. On the other hand, ν(OH) band at 3290 cm^{-1} was not detected at 140 K pointing on parallel O-H bond to the surface plane. Characteristic CH_3 stretching ($\sim$2900 cm^{-1}) and deformation (1452 cm^{-1}) features are broader for the multilayer coverage and demonstrates overlapping features (prepared at 90 K). These new features can be associated with methanol molecules in the crystallized multilayer which have different orientations in comparison to the molecules in the first monolayer.

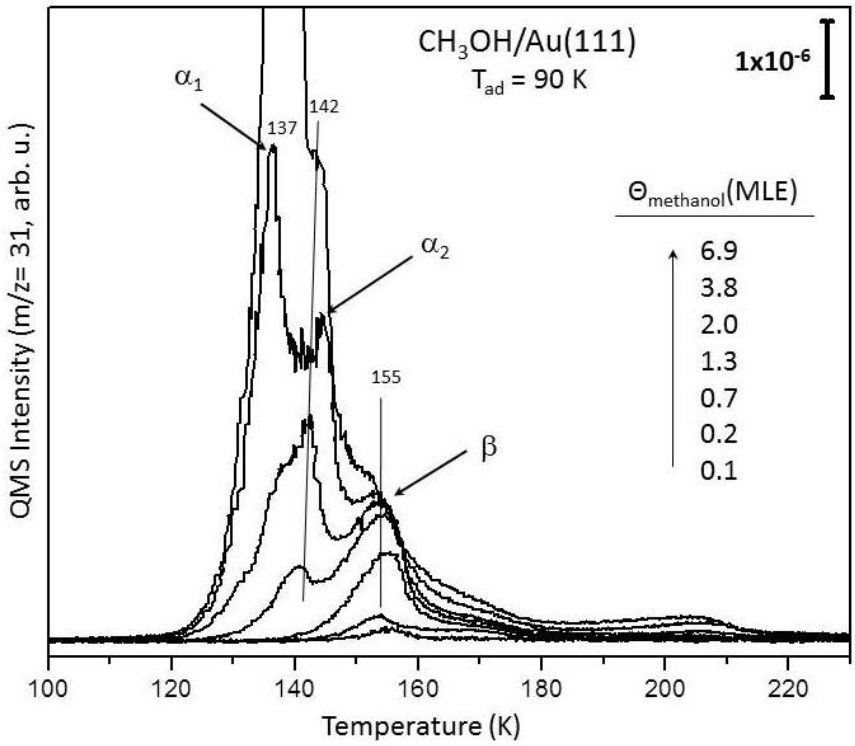

Figure 3.9: TPD profiles (m/z=31) obtained after methanol adsorption on clean Au(111) surface at 90 K as a function of increasing methanol coverage. Reprinted with permission from [110] Copyright (2017) Springer (order number: 4206641091824).

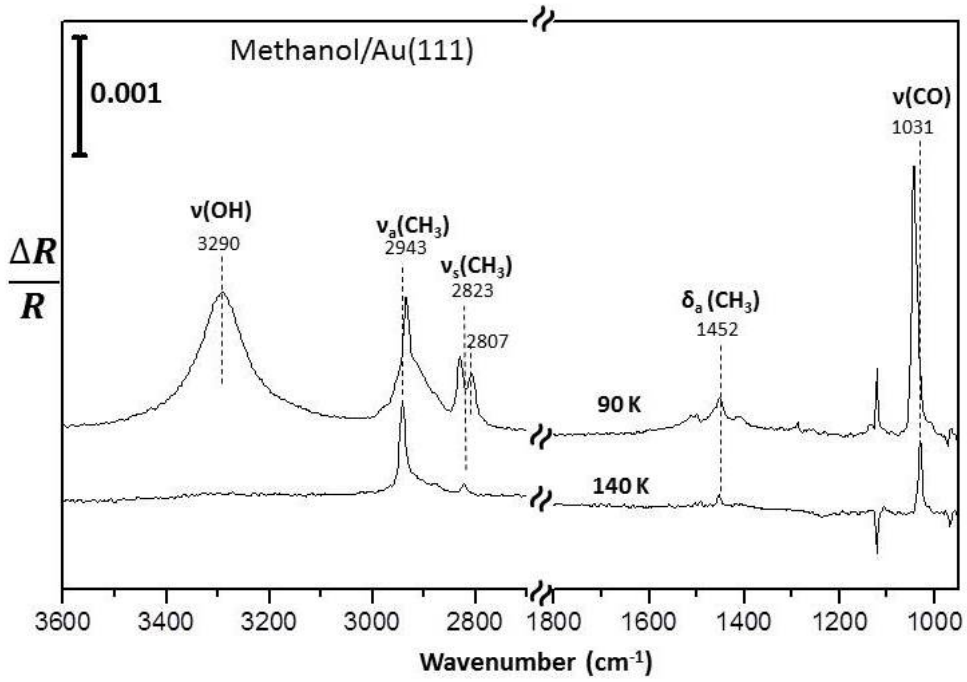

Figure 3.10: IRAS spectra of monolayer and multilayer of methanol on clean Au(111)

3.3.2 Methanol on Oxygen pre-covered Au(111) Single Crystal

TPRS profiles recorded after ozone exposure onto the clean Au(111) surface at 460 K (a) and 140 K (b) followed by subsequent methanol exposure ($\theta_{methanol}$ = 2.6 MLE) at 140 K are given in Figure 3.11. Atomic oxygen coverage in these experiments was estimated as 0.2 MLE. m/z=32 is a common fragment for molecular oxygen and methanol desorption and the most intense signal of methanol (m/z=31) was not additionally shown in Figure 3.11 not to make the figure crowded. Signal of m/z=32 channel at $\sim$ 200 K in both figures is associated with molecular desorption of unreacted methanol desorbing from the Au(111) surface non-dissociatively which was shown at $\sim$160 K previously in Figure 3.9. It was shown in the literature that monolayer methanol desorption from clean Au(110) surface is $\sim$ 200 K and it is obvious that atoms in the underlying second layer in Au(110), which can be easily exposed to the adsorbed methanol molecules, increase the adsorption strength [111]. Thus, increase of

monolayer desorption temperature from pre-oxidized Au(111) surface can be related to the change of surface morphology. In addition, Gong *et al.* attributed increase of methanol monolayer desorption temperature on oxygenated surface to either methanol stabilization by oxygen atom or recombination and disproportionation of the methoxy groups [107]. In Figure 3.11a, recombinative oxygen desorption was observed in m/z=32 channel at ∼500 K. As can be seen from the figure, methanol and oxygen desorb separately at different temperatures when oxygen was accumulated at 460 K. No (or very limited) interaction was observed between methanol and oxygen which can be indicated by limited detection of complete methanol oxidation product, CO_2 (m/z=44). In addition, no signal was detected for the oxidative coupling product of methanol, methyl formate, in the m/z=60 channel.

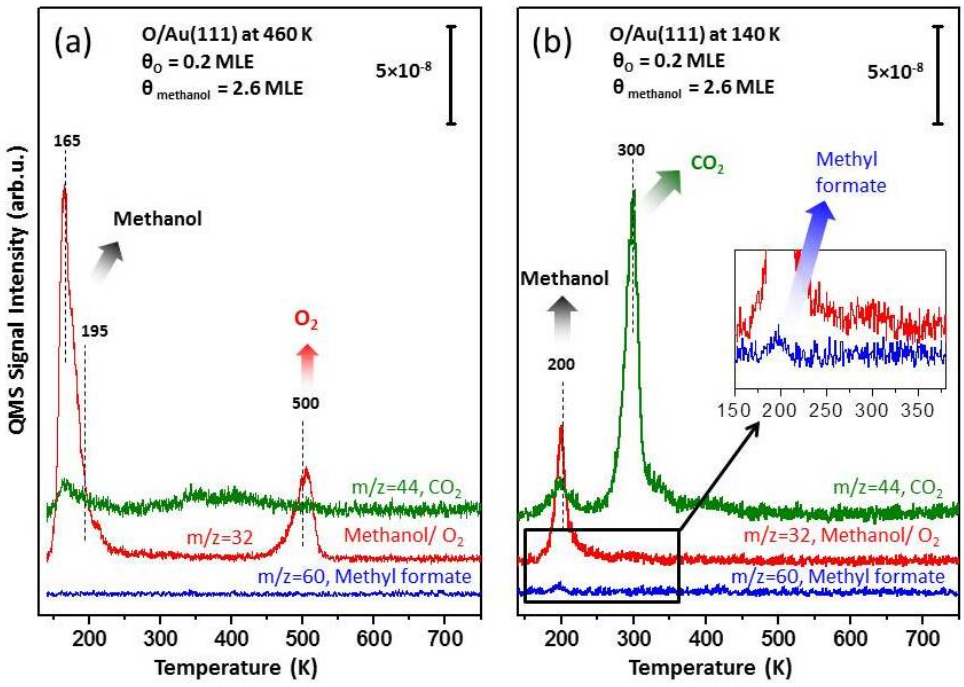

Figure 3.11: TPRS profiles for the reaction of methanol with oxygen accumulated at (a) 460 K, (b) 140 K on Au(111).

In contrast to the TPRS results given in Figure 3.11a, oxygen overlayer prepared at 140 K (O_a) interacts with methanol with complete oxygen utilization and no oxygen desorption at 500 K was detected in Figure 3.11b. All oxygen was consumed to produce CO_2 and methyl formate. Very intense CO_2 signal at

300 K and small methyl formate together with excess methanol signals at 197 K were observed. It must be mentioned that the main ionization fragment of methyl formate is m/z=31 which is a fragment of methanol as well. Since following a common fragment complicates the analysis, m/z=60 channel was followed for methyl formate. According to NIST database [112] characteristic m/z=60 fragment of pure methyl formate gives only 40% of the m/z=31 signal. Methyl formate as a methanol partial oxidation product on gold at low temperature was reported in the former studies on Au(111) [113] and on supported gold catalysts [114]. Current results confirm the oxidative coupling reaction of methanol on Au(111).

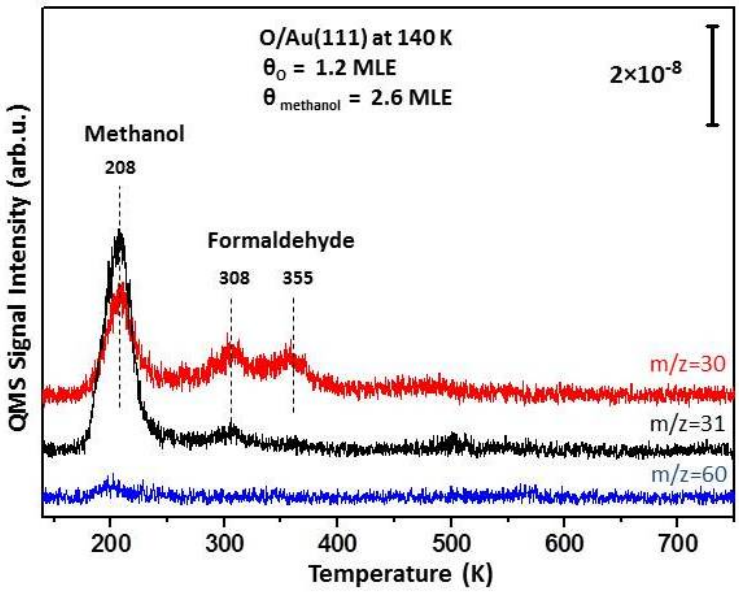

Figure 3.12: TPRS profile showing desorption channels of methyl formate (oxidative coupling product) and formaldehyde (partial oxidation product) obtained after methanol exposure to oxygen pre-covered Au(111).

In addition to the methyl formate formation, another oxidation product formaldehyde was also observed from the partial oxidation reaction of methanol with the increase of oxygen coverage on Au(111). TPRS spectra representing formaldehyde formation are given in Figure 3.12. m/z= 30/31 ratio is calculated for methanol and formaldehyde from the RGA results given in Appendix B as 0,4 and 24, respectively. When this ratio is considered, it is obvious in Figure 3.12 that the desorption signals at 308 and 355 K belong to formaldehyde desorption.

Molecular methanol and methyl formate desorption are also seen at ∼200 K in Figure 3.12.

When oxygen overlayer was prepared at 300 K, a distinct peak of CO_2 (m/z=44) was observed at 310 K together with the unreacted methanol and oxygen desorption at 195 K and 500 K, respectively (Figure 3.13a). Thus, it can be deduced that some quantity of oxygen is able to interact with methanol in contrast to oxygen overlayer that was prepared at 460 K. Scales of figures in 3.11 and 3.13 are all identical. It is worth mentioning that with the increase of oxygen coverage (in the existence of excess methanol), the intensity of CO_2 peak at 310 K does not grow while the O_2 signal proportionally increases (Figure 3.13b). Therefore, only limited quantity of oxygen is able to interact with methanol when it is accumulated at 300 K and oxygen mostly desorbs as unreacted oxygen. Formation of methyl formate (Figure 3.13a,) is not obvious, probably due to the limited activity of oxygen suppressing formation of both CO_2 and methyl formate.

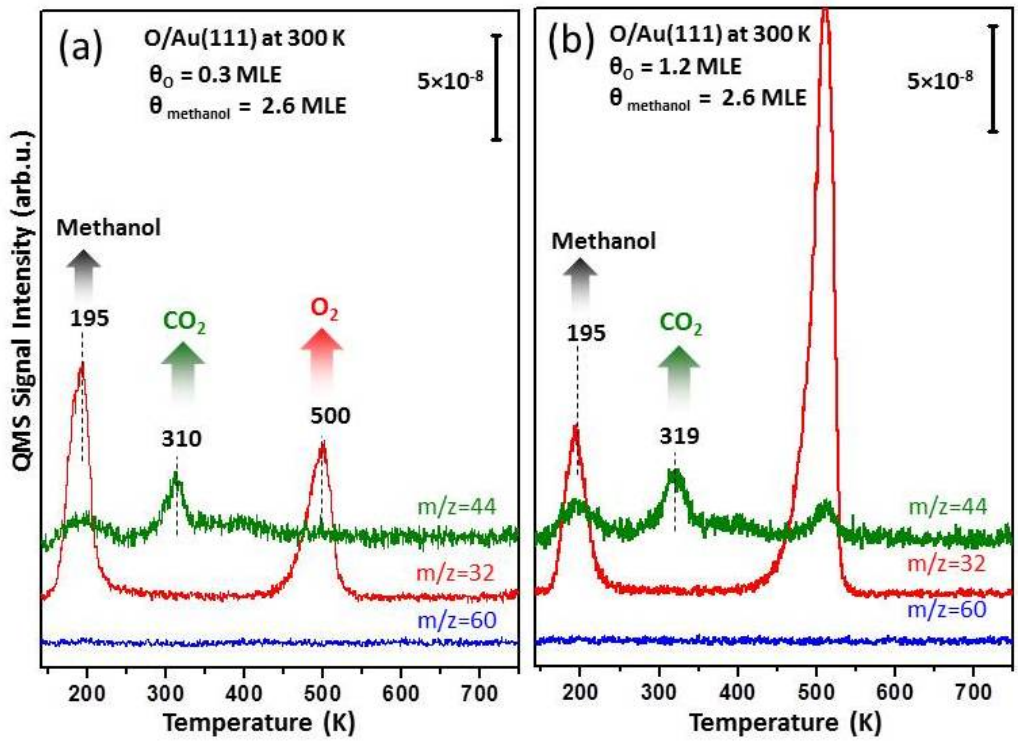

Figure 3.13: TPRS profiles for the reaction of methanol with (a) 0.3 MLE (b) 1.2 MLE of oxygen accumulated at 300 K on Au(111)

Overall, surface atomic oxygen (O_a) activates O-H and C-H bond to yield formaldehyde and methyl formate with the reaction of methanol on Au(111) single crystal while dissolved oxygen atom (O_{sub}) has limited reactivity towards this reaction. In addition, 2D surface gold oxide (O_{ox}) mostly gives CO_2 as a total oxidation product. Methanol oxidation reaction mechanism on Au(111) surface was suggested in the literature by Friend and co-workers as follows [113]: Active oxygen (denoted as O_a in the current study) activates O-H bond of methanol and forms methoxy on the surface (Eq 3.1). Then formaldehyde is formed by β-H elimination (*i.e.* C-H bond cleavage) (Eq 3.2). Formaldehyde either desorbs to the gas phase or is attacked by another methoxy to form methyl formate (Eq 3.3). Reaction of formaldehyde with adsorbed atomic oxygen yields consecutively formate and CO_2 (Eqs 3.4-3.5).

$$2CH_3OH(g) + O(a) \rightarrow 2CH_3O(a) + H_2O(g) \tag{3.1}$$

$$CH_3O(a) \rightarrow H_2CO(a) + H(a) \tag{3.2}$$

$$H_2CO(a) + CH_3O(a) \rightarrow HCOOCH_3(g) + H(a) \tag{3.3}$$

$$H_2CO(a) + O(a) \rightarrow HCOO(a) + H(a) \tag{3.4}$$

$$HCOO(a) \rightarrow CO_2(g) + H(a) \tag{3.5}$$

3.4 C-C Activation on Au(111) Single Crystal

3.4.1 Acetaldehyde and Methyl Formate on Clean Au(111) Single Crystal

Before the investigation of the interaction between adsorbed oxygen species with acetaldehyde on the Au(111) model catalyst surface, it is instructive to examine the adsorption/desorption phenomena corresponding to the reactant and the product. Thus, the adsorption and desorption properties of acetaldehyde and methyl acetate on the clean Au(111) model catalyst surface were investigated.

QMS fragmentation patterns of acetaldehyde and methyl acetate was given in Appendix B. Detailed analysis of the coverage-dependent adsorption behavior of acetaldehyde on the clean Au(111) model catalyst surface at 90 K is given in Figure 3.14. The TPD results presented in Figure 3.14 are in very good agreement with the former work of Pan *et al.* [115]. Based on this former report, 117 K and 124 K desorption features in Figure 3.14 can be attributed to the molecular desorption of acetaldehyde from multilayer states, where the former feature can be associated with an amorphous acetaldehyde multilayer while the latter corresponds to a crystalline multilayer phase. The characteristic desorption signal at 139 K can be assigned to the desorption of acetaldehyde from the first monolayer on the Au(111) surface. On the other hand, the high temperature desorption signal located at *ca.* 194 K is associated with the decomposition of the polymerized forms of acetaldehyde on the Au(111) model catalyst surface. It is worth mentioning that polymerization of acetaldehyde has been reported on a variety of single crystal surfaces where the polymerization was confirmed by TPD and/or High Resolution Electron Energy Loss Spectroscopy (HREELS) on Ru(001) [116], Pt(111) and Sn/Pt(111) [117], and Ag(111) [118], while acetaldehyde polymerization was not observed on Pd(111) [119].

As can be seen in Figure 3.14, relative acetaldehyde coverages present on the Au(111) surface can be calibrated using the 139 K desorption signal corresponding to the molecular acetaldehyde in the first monolayer. By considering the maximum integrated desorption signal that can be attained by the 139 K (*i.e.* monolayer) peak in the absence of any multilayer features located at 124 K or 117 K, one can estimate the approximate saturation coverage of adsorbed species in the first monolayer. This can be achieved by integrating the m/z=29 TPD curve between 128-223 K at the particular exposure corresponding to a maximum intensity of the 139 K feature (*i.e.* $\epsilon_{Acetaldehyde} = 0.010$ L). This approach is based on the presumption that during the completion of the first monolayer, albeit a limited extent, polymeric states start to appear before the saturation of the monolayer feature at 139 K.

Along these lines, the interplay between the monolayer desorption feature at 139 K and the polymerization-related desorption states located at 185, 194 and

202 K in Figure 3.14; is worth discussing in further detail. It is plausible that during the completion of the first monolayer, 2D polymeric acetaldehyde species may be formed in addition to the adsorbed acetaldehyde species. This particular 2D polymeric state has a characteristic decomposition temperature of 185 K. As can be seen in the inset of Figure 3.14, at high acetaldehyde surface coverages exceeding a monolayer, intensity of the 139 K feature starts to attenuate at the expense of the growth of the multilayer features (*i.e.* 124, 117 K) along with new and strong desorption signals at 194 and 202 K. Therefore, it can be argued that at high surface coverages of acetaldehyde on Au(111), polymerization starts to dominate which lead to the formation of strongly bound 3D polymeric species [116], decomposing and desorbing at elevated temperatures (*i.e.* at 194 and 202 K).

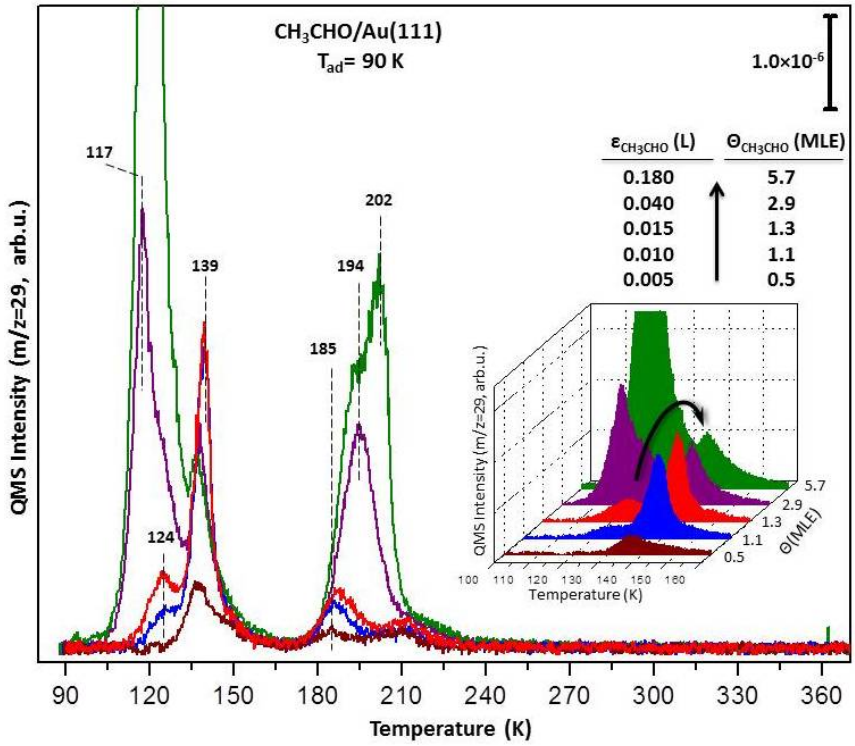

Figure 3.14: Coverage-dependent TPD profiles for the $m/z = 29$ desorption channel obtained *via* acetaldehyde ($CH_3CHO(g)$) adsorption on the clean Au(111) model catalyst surface at 90 K. Inset emphasizes the non-monotonic intensity of the chemisorbed acetaldehyde desorption feature at 139 K as a function of acetaldehyde coverage.

Having investigated the adsorption behavior of the reactant, the adsorption of methyl acetate (CH_3COOCH_3, MA)which is the oxidative coupling product that can be generated during the reaction of acetaldehyde with oxygen pre-covered Au(111) was studied. As can be seen in the fragmentation pattern of MA in Appendix B, the main QMS fragmentation signal is observed for m/z=43. Thus, we performed coverage-dependent TPD experiments on the clean Au(111) surface at 90 K by varying the MA exposure (Figure 3.15) and monitoring the m/z=43 desorption signal. Figure 3.15 indicates that low exposures of MA on Au(111) leads to a characteristic desorption feature at *ca.* 172 K. This particular desorption feature can be assigned to the molecular adsorption of MA on Au(111) in the first monolayer. It is apparent that 172 K desorption signal saturates for higher MA exposures. At higher exposures (*e.g.* 0.01 L), a weak desorption feature can be detected at 146 K, which can be assigned to MA species originating from the second layer. Further increase in the MA exposure results in the observation of two multilayer desorption features at 140 and 142 K which can be attributed to crystalline and amorphous multilayer phases, respectively.

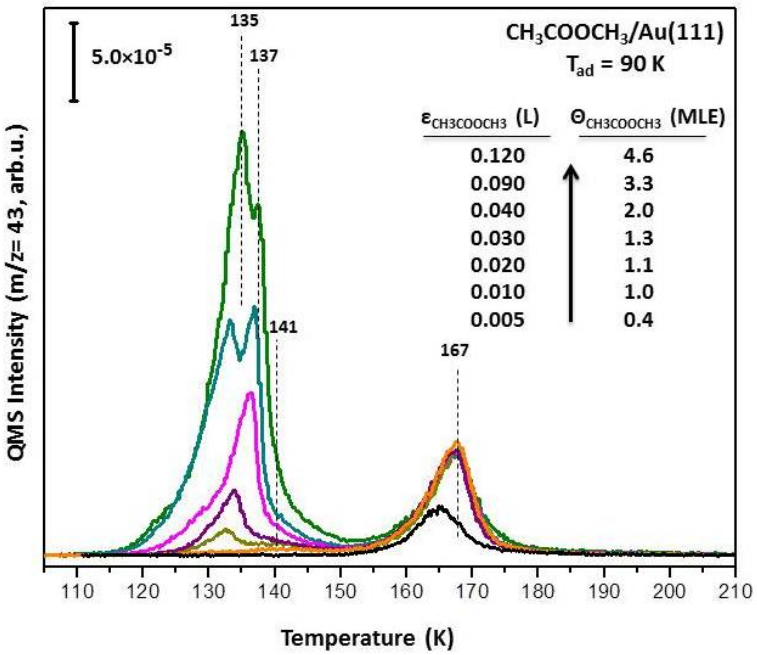

Figure 3.15: Coverage-dependent TPD profiles for the m/z=43 desorption channel obtained via methyl acetate (CH_3COOCH_3(g)) adsorption on the clean Au(111) model catalyst surface at 90 K.

3.4.2 Acetaldehyde on Oxygen Pre-covered Au(111)

The reaction between the oxygen pre-covered Au(111) single crystal model catalyst surface with acetaldehyde was investigated *via* TPRS. Figure 3.16 presents the corresponding TPRS results where a clean Au(111) surface was initially covered with 0.1 MLE of oxygen (O_a) at 140 K. This was followed by 2.9 MLE of acetaldehyde accumulation at 90 K. Relevant desorption channels (*i.e.* m/z = 18, 28, 29, 32, 43, 44, 45 and 59) were simultaneously monitored during the temperature-programmed reaction. Analysis of the normalized relative QMS fragmentation patterns given in Appendix B suggests that m/z = 18, 28, 29, 45, 59 desorption channels can almost exclusively be explained by considering a single species for each desorption channel (*i.e.* H_2O, CO, CH_3CHO, CH_3COOH and CH_3COOCH_3; respectively). On the other hand, m/z=44 desorption channel can be associated with both CH_3CHO and CO_2 species. At least three separate species can simultaneously contribute to the m/z=43 desorption channel; namely CH_3CHO, CH_3COOH and CH_3COOCH.

In Figure 3.16, the desorption peaks located at 141 K appearing in multiple desorption channels such as m/z = 28, 29, 43 and 44 can be predominantly due to the chemisorbed acetaldehyde in agreement with similar TPD features located at 138-139 K in Figure 3.14. Figure 3.16 reveals a water desorption signal located at 154 K. Since this feature is not accompanied by concomitant carbon-containing desorption features of similar magnitude appearing at 154 K; it is likely that this particular water desorption signal is associated with background water accumulated on the surface at low temperatures during the experiment. Similar water desorption signals at 154 K have been observed after individual adsorption of acetaldehyde and methyl acetate experiments. Desorption features located at 171 K in Figure 3.16 particularly for the m/z = 29, 43 and 59 desorption channels can be assigned to predominantly MA, the oxidative coupling product. It is worth mentioning that since the m/z=44 trace in Figure 3.16 does not reveal an intense feature at 171 K, a significantly high contribution of acetaldehyde to this feature can be ruled out. Furthermore, desorption of MA at 171 K during the reaction of oxygen pre-covered Au(111) with acetaldehyde is in perfect agreement with the

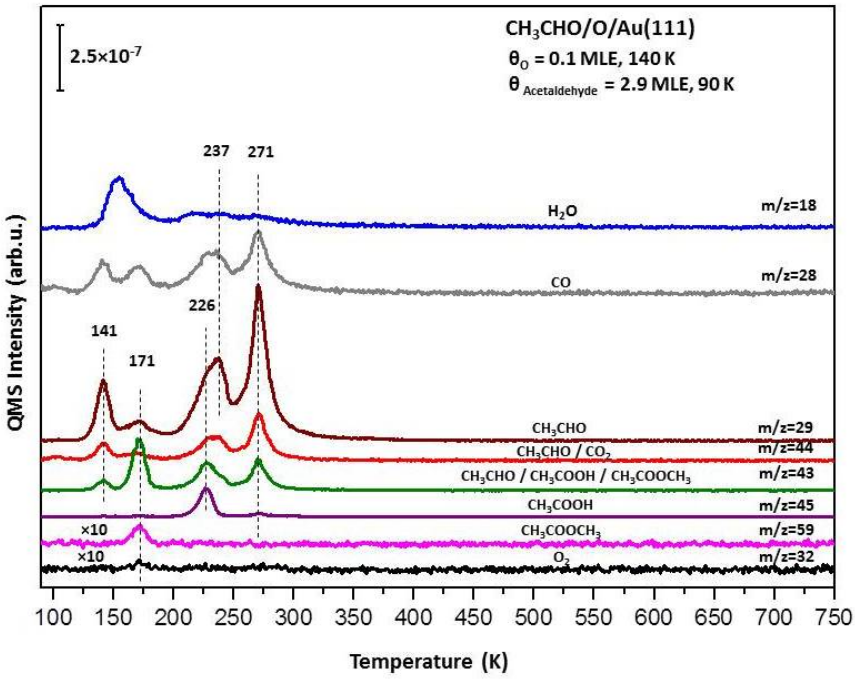

Figure 3.16: TPRS profiles for various desorption channels obtained after 2.9 MLE of acetaldehyde accumulation at 90 K on 0.1 MLE of oxygen pre-covered Au(111) model catalyst surface at 140 K

desorption temperature of chemisorbed MA on the clean Au(111) model catalyst surface as shown in Figure 3.15. On the other hand, the significant CO desorption signal located at 171 K can be attributed to the decomposition of chemisorbed acetaldehyde species into CO and H_2 (the latter species was not followed in the current TPRS experiments). This is due to the fact that neither MA nor acetaldehyde species has an intense QMS fragmentation signals at m/z=28. One can note that ethyl acetate (like methyl acetate) also has an intense m/z=43 fragmentation signal [120] and can be considered as an alternative product. However, lack of the m/z=45 signal at 171 K which is an expected fragmentation signal for ethyl acetate suggests that a significant amount of ethyl acetate formation in addition to MA can be ruled out. Furthermore, control experiments involving individual ethyl acetate adsorption on the clean Au(111) single crystal surface showed that for adsorbate coverages less than 1 ML, ethyl acetate desorbs at a temperature of 189 K with a first-order desorption kinetics [110]. This particularly higher desorption temperature of ethyl acetate is also in accordance with

the interpretation that the 171 K feature in the m/z=43 trace of Figure 3.16 is predominantly associated with MA rather than ethyl acetate.

Figure 3.16 shows that at higher temperatures, TPRS data reveal a distinct desorption feature at 226 K for the m/z=45 channel which is exclusively associated with acetic acid. It is worth mentioning that this particular feature cannot be attributed to diethyl ether; since there is no detectable feature in the m/z=59 TPRS channel of Figure 3.16 at 226 K. Influence of the acetic acid desorption is also visible in other relevant desorption traces such as m/z=29, 43, 44. However behavior of m/z=29, 43, 44 at T $\geq$ 200 K is more complex due to the contribution to these desorption channels from the desorption products of polymerized acetaldehyde species as well as decomposed acetic acid [121]. On the other hand, the desorption signals appearing at 237 K in m/z=28, 29, 43, 44 traces of Figure 3.16 have a smaller contribution from acetic acid due to the lack of the m/z=45 desorption signal at 237 K and reflect a convoluted identity that can be associated with acetaldehyde and CO_2. However, lack of a significant H_2O desorption signal (*i.e.* m/z=18 in Figure 3.16) within the temperature window of 200-300 K suggest that total oxidation is not significant under such reaction conditions. Finally increasing the reaction temperature to 271 K leads to the evolution of strong desorption signals which can be originating from the decomposition of polymerization products of acetaldehyde as well as the decomposition of acetic acid. It is worth mentioning that no significant O_2 (*i.e.* m/z=32) desorption was detected throughout the TPRS experiments given in Figure 3.16.

As a result, surface atomic oxygen (O_a) reacts with acetaldehyde on Au(111) surface and yields two different partial oxidation products namely, methyl acetate and acetic acid without the formation of significant quantities of carbon dioxide. Since the formation of methyl acetate as the oxidative coupling reaction product implies C-C bond activation; it was demonstrated that O_a containing Au(111) single crystal model catalyst surface can activate C-C bonds.

3.5 N-H Activation on Au(111)

3.5.1 Ammonia adsorption on clean Au(111)

In order to reveal the specific fragmentation pattern of ammonia, RGA analysis was performed and the fragmentation pattern was given in Appendix B. Ammonia adsorption was carried out on the clean Au(111) single crystal at 90 K and m/z=17 signal was monitored in TPD experiments along with m/z = 28, 18, and 2 signals in order to check the presence of potential decomposition products and water desorption from background adsorption. In all of the TPD experiments, ammonia was found to desorb molecularly in a reversible manner from the clean Au(111) single crystal surface.

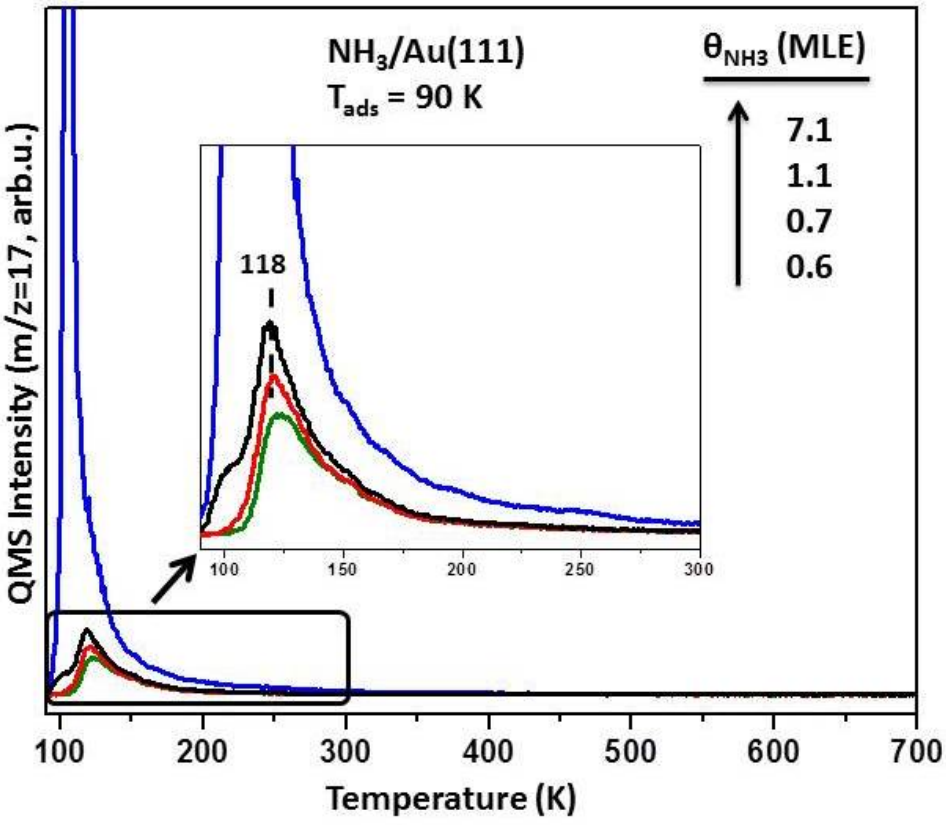

Figure 3.17: TPD profiles (m/z = 17) obtained after ammonia adsorption on clean Au(111) surface at 90 K as a function of increasing ammonia coverage

Figure 3.17 shows m/z=17 desorption signal as a function of ammonia coverage. In this figure, ammonia desorption maximum located at 123 K was observed for the lowest ammonia coverage. With increasing ammonia coverage, desorption signal at 123 K became broader and its desorption maximum shifted to 118 K. Broadening and temperature shift with increasing coverage in the sub-monolayer range is a common behavior of ammonia on metal surfaces such as Pt [122], Rh [123], Ir [124]. An additional desorption signal appeared at 100 K with higher ammonia coverage which can be assigned to the formation of multilayer ammonia overlayers. These TPD results are in a perfect agreement with the literature data [125]. At very high ammonia coverages, monolayer and multilayer signals converge due to the multilayer desorption signals exhibiting zero-order desorption kinetics. TPD data given in Figure 3.17 can be used to estimate the relative ammonia surface coverages. For this purpose, the multilayer signal at 100 K was deconvoluted and subtracted from the whole desorption spectrum and the integrated desorption signal between 105 K and 400 K associated with the desorption maximum at 118 K was used to estimate θ_{NH3}=1 MLE.

3.5.2 Ammonia on Oxygen Pre-covered Au(111)

Ammonia oxidation reactions were carried out on O/Ag(111) and the resulting products were followed in TPRS experiments. It was observed that ammonia dissociates in the presence of adsorbed oxygen on the Au(111) surface. During TPRS experiments for ammonia oxidation on Au(111), QMS channels for molecular ammonia (m/z = 17, 16) and potential oxidation products, namely N_2 (m/z=28), NO (m/z=30), NO_2 (m/z=46) and N_2O (m/z=44) were simultaneously followed together with H_2O (m/z=18) and O_2 (m/z=32) desorption. Figure 3.18 represents TPRS spectra taken after exposing θ=0.6 MLE of ammonia at 83 K (a) and 190 K (b) on 0.3 MLE oxygen pre-covered (O_a) gold surface. In Figure 3.18a, molecular ammonia desorbs at 138 K and water from background adsorption desorbs at 190 K while the recombinative desorption of N_2 (m/z=28) produces multiple signals between 290 K and 490 K. N_2 desorption reveals N-H cleavage and NH_x formation on the Au(111) single crystal. In addition, water desorption

within the same temperature range was also in line with the N-H bond activation and hydrogen abstraction from ammonia by surface oxygen atoms on Au(111). No other desorbing products were observed in this particular experiment.

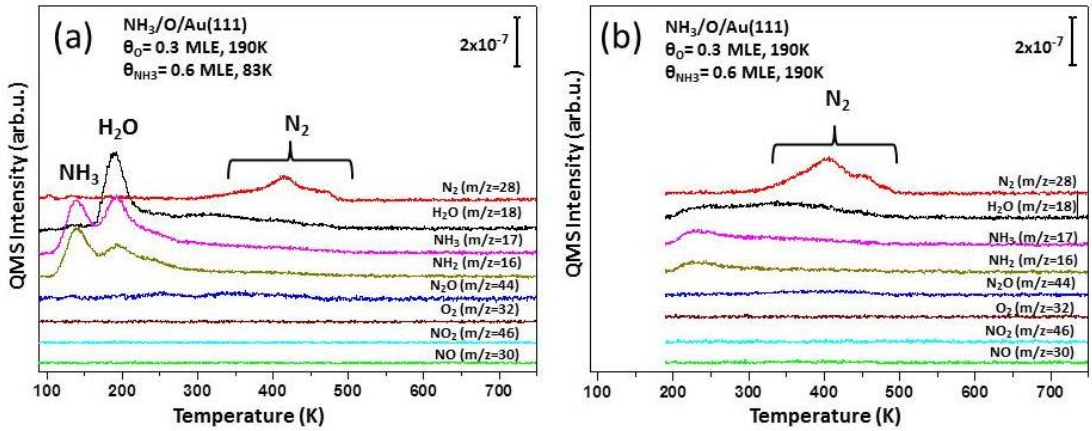

Figure 3.18: TPRS profiles for the reaction of ammonia (0.6 MLE) at 83 K (a) and 190 K (b) on 0.3 MLE oxygen pre-covered gold surface at 190 K.

In order to prevent poisoning of the O/Au(111) surface with excess ammonia and background water adsorption, NH_3 was dosed on the O/Au(111) at 190 K (*i.e.* at a temperature above the desorption maximum of the first monolayer of ammonia on clean Au(111)). TPRS spectra for this experiment are given in Figure 3.18b. In this particular case, much smaller unreacted ammonia and water desorption between 200 K - 250 K were observed in comparison to the former conditions. Moreover, the signal intensity of N_2 (m/z=28) increased indicating more N-H bond activation and more NH_x formation on the surface. Similarly, water desorption caused by N-H activation was also observed at between 300 K - 500 K.

In addition, atomic oxygen coverage was increased to 0.6 MLE in order to explore the effect of O/NH_3 ratio on the nitrogen formation selectivity. Nitrogen atoms were further oxidized; NO desorption at 460 K and N_2O desorption between 300 K - 480 K were observed.Besides, unreacted excess O_2 desorption was also observed at 500 K. TPRS results for ammonia oxidation on the oxygen rich gold surface can be seen in Figure 3.19.

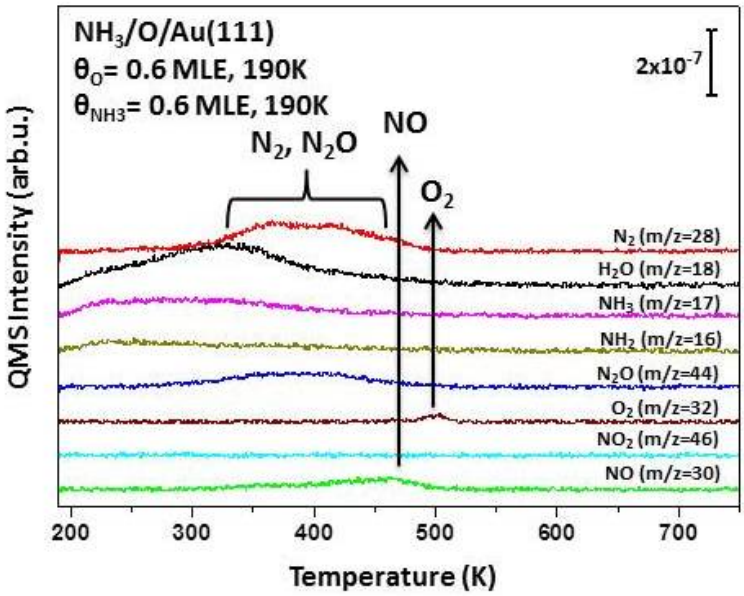

Figure 3.19: TPRS profiles for the reaction of ammonia (0.6 MLE) at 190 K on 0.6 MLE oxygen pre-covered gold surface at 190 K.

As a result, surface oxygen atom (O_a) activates N-H bond in ammonia molecule and selectively yields N_2 without any other oxidation products such as NO and N_2O for low coverage. The selectivity of the ammonia oxidation reaction to the products can be tuned by the oxygen quantity.

Chapter 4

Bond Activation on Silver

4.1 Characterization of the Ag(111) Single Crystal Surface

Ag(111) surface was atomically cleaned by multiple cycles of Ar^+ sputtering followed by subsequent annealing at 773 K under UHV conditions. The cleanness of the surface was confirmed by XPS. Sputtering-annealing cycle was repeated until the impurities dropped below detection limits. A representative survey scan of the clean Ag(111) single crystal after Ar^+ sputtering and annealing cycles is shown in Figure 4.1. As can be seen in the figure, no significant impurities were observed within our detection limit.

In order to determine the chemical states of silver atoms, Ag *3d* region was also analyzed by XPS and the spectrum is given in Figure 4.2a. Ag $3d_{5/2}$ signal was

found to be located at 368.3 eV indicating metallic state of silver atoms (*i.e.* Ag^0) [92]. In Figure 4.2a, small signals appearing between 366-356 eV were identified as Mg α_3 and Mg α_4 x-ray satellites.

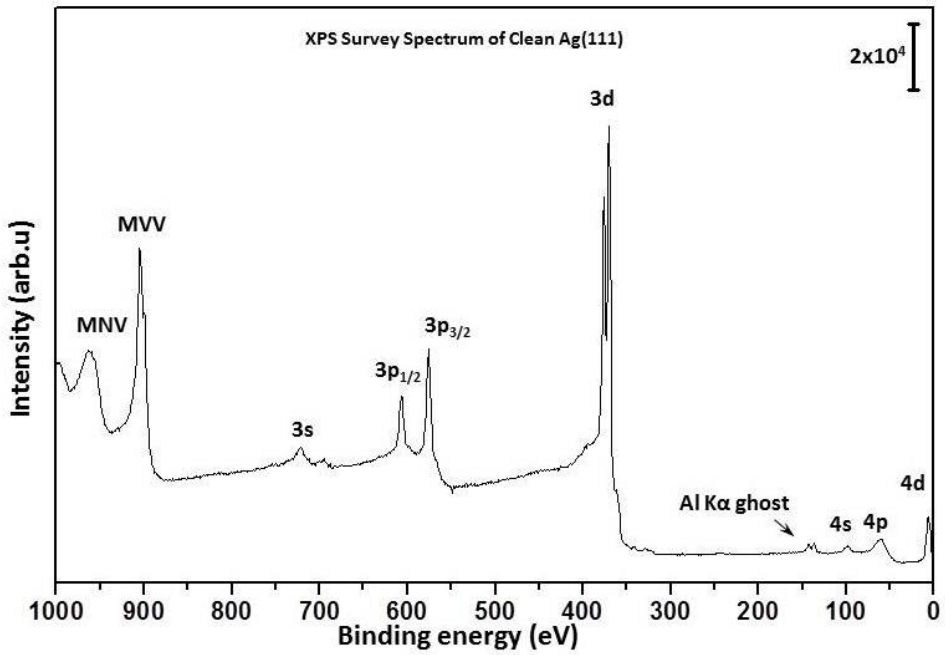

Figure 4.1: A representative survey XP spectrum of the clean Ag(111) single crystal.

In addition to the impurity and the chemical state analysis of the silver surface by XPS, atomic level crystallographic orientation of the Ag (111) single crystal surface was also confirmed by LEED. Hexagonal (1×1) crystal pattern was obtained from the clean Ag(111) single crystal surface and the LEED image is shown in Figure 4.2b.

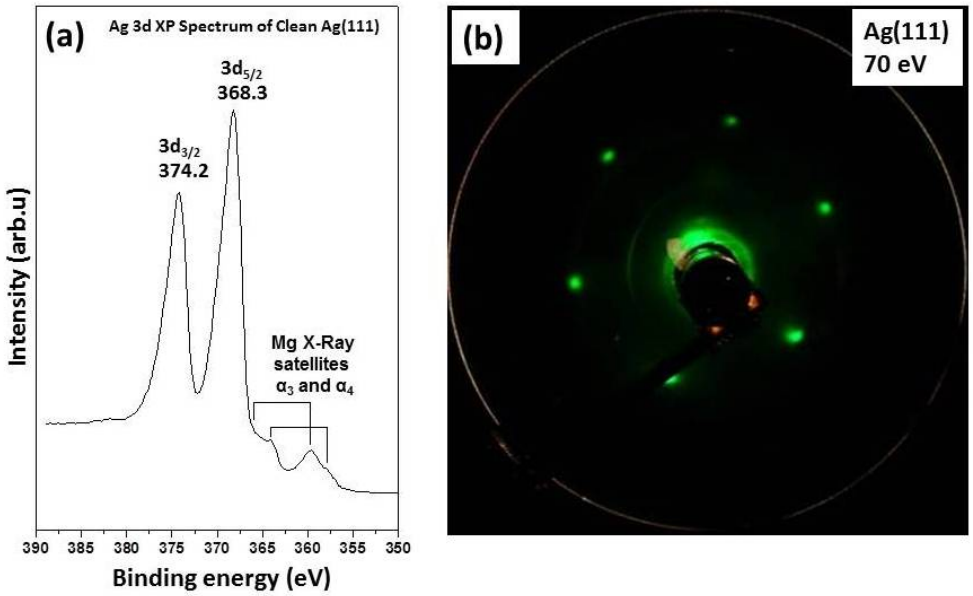

Figure 4.2: (a) Ag *3d* XP spectrum (b) LEED pattern of the clean Ag(111) single crystal.

4.2 Oxygen Behavior on Ag(111) Single Crystal

Before the investigation of the effect of the oxygen species on bond activation, behavior of oxygen species generated upon ozone decomposition on clean Ag(111) single crystal model catalyst surface was studied via TPD, LEED and XPS techniques. For this purpose, increasing exposures of ozone were introduced on Ag(111) at 140 K and the TPD spectra of molecular oxygen (m/z = 32) desorbing from the Ag(111) single crystal surface as a function of temperature were acquired as shown in Figure 4.3a. As can be seen in Figure 4.3a, oxygen desorption starts at 535 K for an oxygen surface coverage of θ_O = 0.13 MLE and the desorption temperature slowly increases with increasing oxygen surface coverage. Furthermore, various additional low-temperature (T<525 K) desorption features (*e.g.* see the red spectrum in Figure 4.3a) start to appear and grow in intensity with increasing θ_O. These features can be associated with subsurface atomic oxygen (O_{sub}) as previously reported in the literature [38, 58]. These low temperature features do not converge to a saturation as in agreement with a former report [58], presumably due to the diffusion of atomic oxygen into the

subsurface. Campbell *et al.* argued that oxygen atoms could be more stable on the silver surface rather than in bulk silver oxide based on the heat of adsorption of oxygen atoms on Ag(111) as compared to the heat of formation of bulk silver oxide [38]. Therefore, bulk oxide formation due to oxygen diffusion to the silver subsurface seems to be rather unlikely at low oxygen coverages. However formation of bulk-silver oxide at high oxygen coverages is feasible and will be discussed in more detail below. Along these lines, by exploiting isotopically labeled oxygen molecules, Backx *et al.* showed that subsurface oxygen in the Ag(110) surface desorbs at lower temperatures than the surface oxygen atoms [126]. TPD data for O/Ag(111) (Figure 4.3a) obtained via ozone decomposition is in good agreement with a former study, where NO_2 decomposition was utilized for atomic oxygen delivery on Ag(111) [127].

Integrated TPD signals corresponding to surface (O_a) and subsurface (O_{sub}) oxygen species in Figure 4.3a were also calculated individually and plotted as a function of ozone exposure (Figure 4.3b). In this latter plot, monolayer coverage reaches a plateau around 0.04 L which may be attributed to the saturation of the first overlayer on the surface. The absolute surface saturation coverage of the first oxygen monolayer on Ag(111) was previously calculated by Campbell *et al.* [38] for a *(4x4)*-O/Ag(111) surface structure at this coverage. It is worth mentioning that in the current work, *(4x4)*-O/Ag(111) structure was not observed in any of the investigated coverages, because this structure is not stable when oxygen is accumulated under UHV conditions [60, 61]. Nevertheless, in the current work, the saturation exposure of 0.04 L was attributed to 1 MLE and was used to calibrate and quantify other desorption signals. As can be seen in Figure 4.3b, for the ozone exposures above 0.08 L, surface oxygen coverage starts to exceed the convergence coverage of 1 MLE. This can be explained by the transformation of the surface oxygen overlayer to form a new structure with a higher oxygen density. We tentatively assign this latter structure to a bulk-like silver oxide.

Analysis of the Ag(111) single crystal surface after various ozone exposures at 140 K by LEED revealed no ordered structures suggesting randomly located oxygen species at 140 K for all oxygen coverages. However, annealing of the

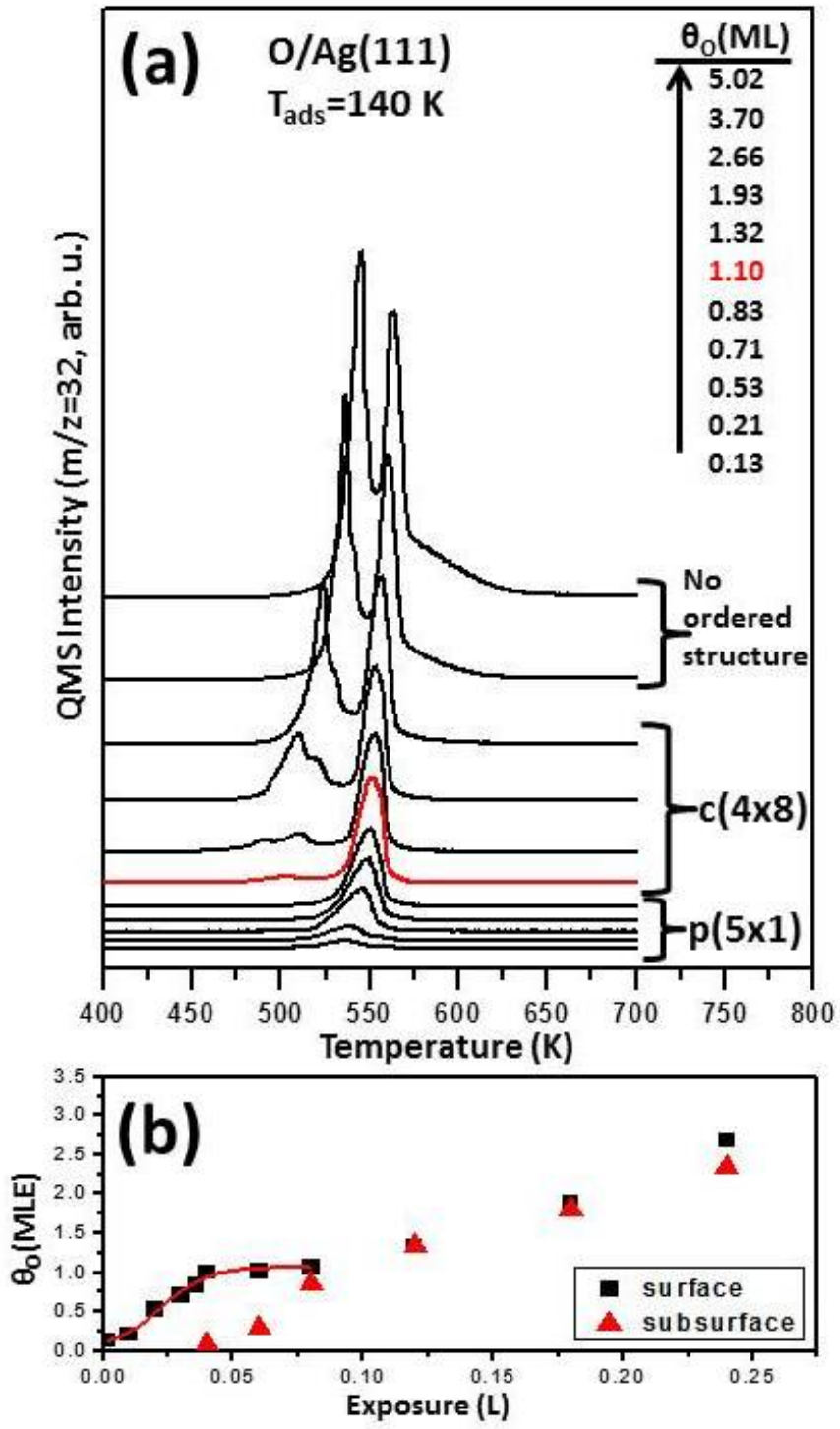

Figure 4.3: (a) TPD profiles for oxygen desorption ($m/z = 32$) obtained by increasing ozone exposures on clean Ag(111) at 140 K. (b) Relative oxygen surface coverages (obtained via integrated TPD desorption signals in part (a)) for surface and subsurface oxygen species on Ag(111) as a function of ozone exposure.

O/Ag(111) surfaces originally prepared at 140 K indicated that thermal activation led to the ordered oxide formation with a *p(5x1)* structure for $\theta_O < 1.10$ MLE (Figures 4.4a and 4.4b), as well as an additional oxide structure which can be tentatively assigned to a *c(4x8)* structure appearing at 1.10 MLE $< \theta_O <$ 1.93 MLE (Figures 4.4c and 4.4d). Oxide formation due to the annealing of oxygen overlayers on Ag(111) was also previously observed by Bukhtiyarov *et al.* [41], where it was demonstrated via XPS that atomic oxygen adsorbed on Ag(111) at 300 K can form silver oxide when the sample was heated to 420 K. LEED images in Figure 4.4 were obtained by dosing different exposures of ozone on Ag(111) at 473 K (*i.e.* a temperature which is slightly below the beginning of the oxygen desorption) followed by pumping and cooling the sample to 140 K for LEED analysis. It is worth mentioning that ozone accumulation using relevant exposures at 140 K and heating to 473 K yielded identical LEED images to that of direct ozone dosing at 473 K. Starting from the lowest oxygen coverage (*i.e.* $\theta_O = 0.13$ MLE) up to $\theta_O = 1.10$ MLE, sharp spots of the *p(5x1)* structure were detectable after annealing at 473 K. For $\theta_O \geq 1.10$ MLE, another ordered LEED structure started to appear after annealing at 473 K along with the emergence of the subsurface oxygen signals in TPD (red spectrum in Figure 4.3a). We tentatively assigned this structure to a *c(4x8)* overlayer consisting of three separate domains rotated by 120° with respect to each other. These domains are color-coded in the theoretical LEED pattern given in Figure 4.4d. *c(4x8)* reconstruction on O/Ag(111) was also observed by Schnadt and co-workers via scanning tunneling microscopy (STM) and was associated with a significantly oxidized silver structure [50]. In the current study, *c(4x8)* structure was only observed at relatively high oxygen coverages (*i.e.* 1.10 MLE $< \theta_O <$ 1.93 MLE) where the surface oxygen species converged to a constant value (black curve in Figure 4.3b) while subsurface oxygen was monotonically rising (red curve in Figure 4.3b). For $\theta_O > 1.93$ MLE, LEED images became extremely fuzzy suggesting the lack of an ordered structure at high coverages. This fuzzy structure may be possibly associated with an amorphous bulk-like oxide structure. Current results are in good agreement with DFT calculations of Li *et al.*, who proposed that increasing oxygen coverages on Ag(111) surface by ozone exposure might lead to ordered atomic oxygen overlayers followed by oxide-like thick films at higher θ_O [45]. In a related study, Martin

et al. deposited atomic oxygen on Ag(111) by thermal cracking of O_2 (g) at 500 K with $P_{O2} = 10^{-7}$ mbar [57]. They reported bulk-like silver oxide formation at high θ_O and argued that *c(4x8)* overlayer is the precursor state for bulk-like silver oxide formation.

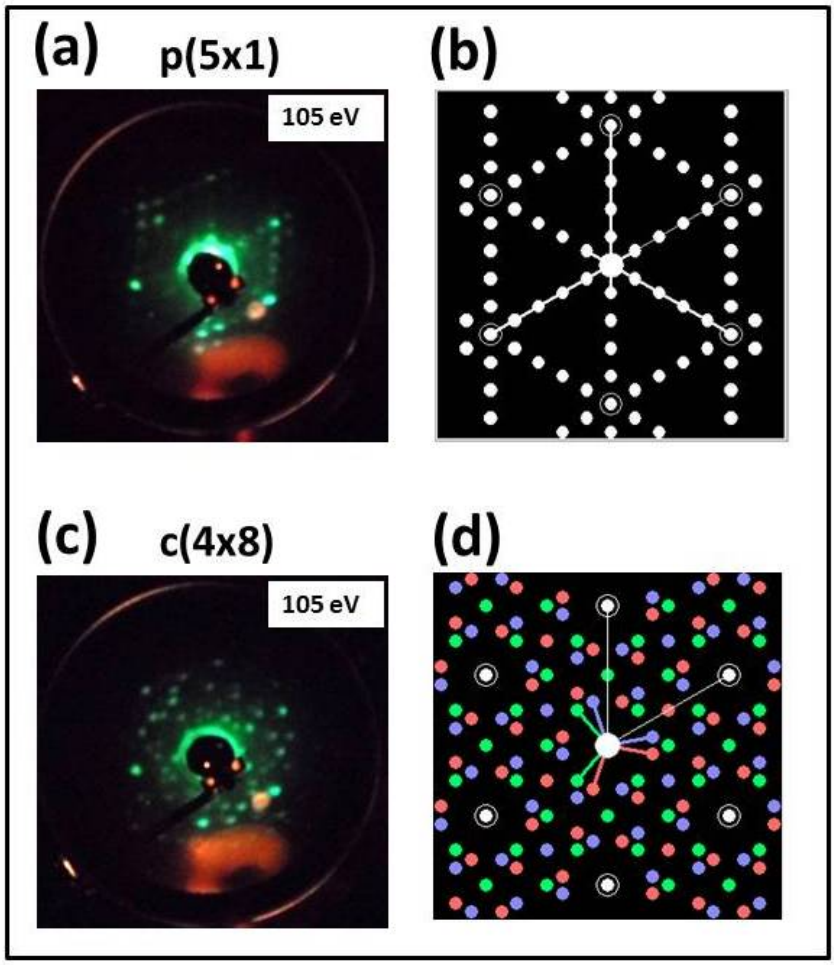

Figure 4.4: LEED images of O/Ag(111) overlayers obtained by introducing different ozone exposures at 140 K on clean Ag(111) surface followed by pumping and annealing to 473 K in UHV. (a) LEED image of the p(5x1)-O/Ag(111) overlayer ($\theta_O = 0.83$ MLE) and (b) its simulated (theoretical) LEED pattern. (c) LEED image of the c(4x8)-O/Ag(111) overlayer ($\theta_O = 1.10$ MLE) and (d) its simulated (theoretical) LEED pattern.

Oxygen accumulation on the Ag(111) surface at 140 K was also analyzed by XPS. O *1s* spectra of the O/Ag(111) surface as a function of increasing oxygen coverage is given in Figure 4.5. Due to the detection limit of our photoelectron

detector, we were able to observe a reliable O *1s* signal at $\theta_O \geq 0.53$ MLE. Signals in the region between 530-531 eV were assigned to atomic oxygen either on the surface (O_a) or in the subsurface (O_{sub}), whereas surface oxide (O_{ox}) signals were found between 528.1-528.5 eV [38, 39, 40, 41, 42, 50, 56, 60, 63, 127, 128]. As mentioned above, ordered surface oxide (O_{ox}) species were not detectable at 140 K according to LEED experiments. Schlögl and coworkers previously reported that O *1s* signal of bulk silver oxide appeared at 529.0 eV [51]. In another study, Heine *et al.* assigned an O *1s* signal at 528.9 eV to silver oxide species at the step edges of the Ag(111) surface [60] and suggested that subsurface oxygen increases the step density of the Ag(111) surface. In Figure 4.5, a noticeable increase in the O *1s* signal at *ca.* 529 eV is visible at $\theta_O \geq 1.10$ MLE (*i.e.* in correlation with the appearance of the subsurface oxygen features in TPD data given in Figure 4.3a). This O *1s* feature at *ca.* 529 eV may be associated with disordered oxide and/or amorphous bulk-like oxide (O_{bulk}) species. Indications of the formation of bulk-like silver oxide species were also present in the Ag *3d* XPS spectra (Figure 4.6) revealing a broadening in the full width at half maximum (FWHM) of the Ag *3d* peak with increasing oxygen coverages $\theta_O > 1.90$ MLE. Broadening of the Ag *3d* XPS signal due to the formation of silver oxide was also previously reported by Bukhtiyarov *et al.* [41].

Inset in the right hand side of Figure 4.5 shows the variation of the O *1s*/Ag *3d* integrated signal ratios in XPS as a function of oxygen coverage calculated from the ozone exposure values using the TPD data in Figure 4.3. It is apparent that the O *1s*/Ag *3d* integrated signal ratio reaches a convergence for $\theta_O \geq 3.70$ MLE (Figure 4.5) while total $m/z = 32$ TPD desorption signal intensity still continues to increase within this coverage window (Figure 4.3b). These observations may indicate continuous transport of oxygen species towards the subsurface region (*i.e.* possibly below 10 nm of the surface) of the O/Ag(111) system at high oxygen coverages which cannot be readily detectable by the surface-sensitive XPS technique. It should be noted that x-ray induced oxygen desorption during XPS analysis could also contribute to the high-coverage convergence of the O *1s*/Ag *3d* signal ratio.

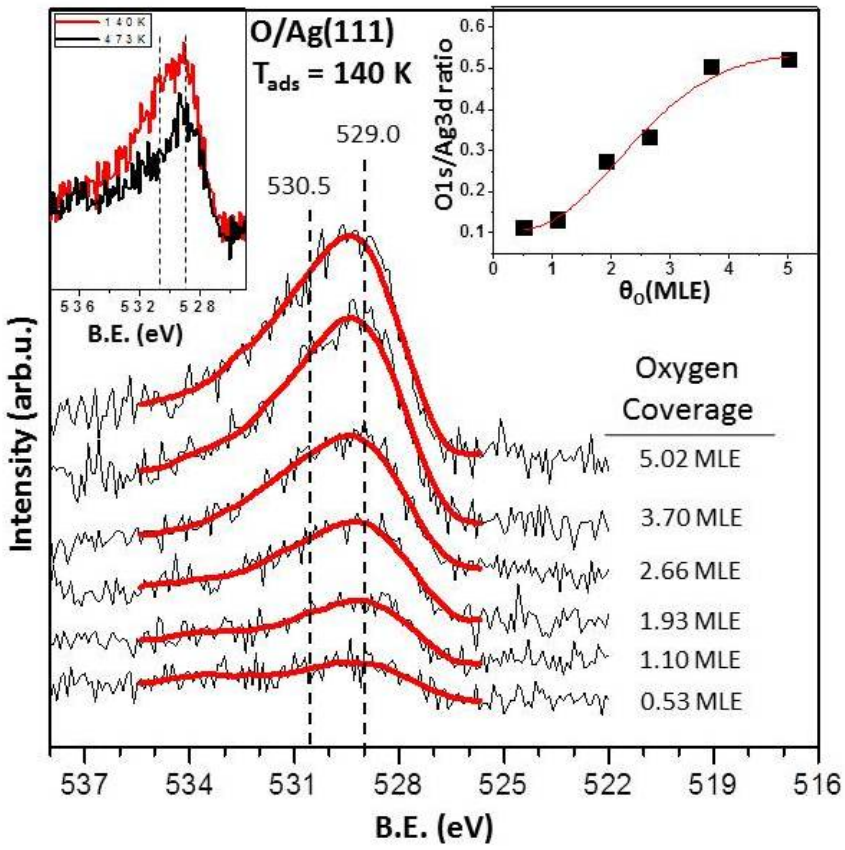

Figure 4.5: O *1s* XPS spectra of O/Ag(111) as a function of increasing oxygen coverage obtained by increasing exposures of ozone at 140 K. Inset on the right shows the integrated O *1s*/Ag *3d* signal ratio as a function of oxygen coverage. Inset on the left shows the O *1s* XPS spectra for O/Ag(111) with $\theta_O = 2.66$ MLE dosed at 140 K (red) and dosed at 473 K (black).

O *1s* signal of 2.66 MLE O/Ag(111) surface obtained at 140 K was also compared to the analogous surface prepared at 473 K using an identical ozone exposure. These results are shown in the left-hand-side inset of Figure 4.5 (red and black spectra; respectively). It is apparent that the O *1s* spectrum corresponding to 473 K reveals attenuated features at *ca.* 529 eV and *ca.* 530.5 eV, which may be attributed to the partial loss of bulk-like oxide (O_{bulk}) and surface/subsurface (O_a/O_{sub}) atomic oxygen species, respectively. O *1s* feature at 529 eV corresponding to bulk-like oxide species shows relatively less significant attenuation. These observations indicate transport of oxygen from the surface and subsurface regions of silver towards bulk upon thermal activation provided by annealing at

473 K.

Other than the O *1s* signals due to surface atomic oxygen (O_a) and bulk-like oxide (O_{bulk}) species, a less prominent shoulder at 532 eV is also detectable in the O *1s* spectra presented in Figure 4.5 which can be associated with hydroxide (minority) species due to background water adsorption. Note that the presence of physisorbed oxygen species can be readily excluded due to the extremely low desorption temperature of such species (*i.e.* ∼50 K) [38].

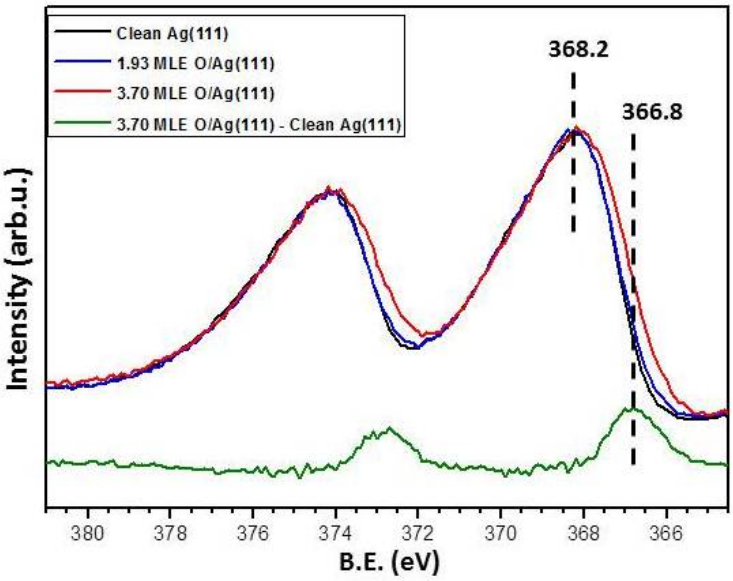

Figure 4.6: Normalized Ag *3d* XPS spectra for clean Ag(111) (black), θ_O = 1.93 MLE O/Ag(111) (blue), θ_O = 3.70 MLE O/Ag(111) (red) and subtracted spectrum of clean Ag(111) from θ_O = 3.70 MLE O/Ag(111) (green).

4.3 C-H and O-H Activation on Ag(111)

In order to determine the reactivity of surface oxygen atoms (O_a) and surface oxide overlayers (O_{ox}) towards C-H and O-H bond activation, O_a and O_{ox} overlayers were separately prepared as described in Section 4.2 and methanol was used as a probe molecule. Methanol oxidation reactions were performed on oxygen pre-covered Ag(111) single crystal at different conditions. Before the methanol

oxidation reactions, desorption behavior and molecular orientation of methanol molecules on the clean Ag(111) single crystal surface without oxygen layers were determined.

4.3.1 Methanol on Clean Ag(111)

Methanol adsorption was carried out on the clean Ag(111) surface at 100 K and m/z=31 signal was monitored in TPD experiments along with other fragments (m/z = 28, 29, 30, 32) and m/z=18 signal for water desorption from background adsorption. Fragmentation pattern of methanol during RGA is given in Appendix B. In all of the TPD experiments, methanol was found to desorb molecularly in a reversible manner from the clean Ag(111) single crystal surface. TPD spectra of m/z=31 signal as a function of methanol exposure are given in Figure 4.7. In this figure, a desorption maximum at 157 K was observed for the lowest methanol coverage of $\theta_{methanol}$ = 0.1 MLE. With increasing methanol coverage, desorption signal became broader and another desorption maximum appeared at 160 K. Figure 4.7 shows that the major methanol desorption features at 155 and 160 K reached saturation which was immediately followed by the appearance of an additional desorption maximum at 138 K that can be assigned to the formation of multilayer methanol overlayers. Integrated desorption signal at the saturation point (third spectrum from the bottom) was assumed to be 1 MLE of methanol coverage and used to estimate the relative coverages of other signals. Presence of two different desorption maxima at sub-monolayer coverages was explained in the literature by suggesting methanol adsorption at two different geometries on Ag(111) single crystal [129]. With increasing methanol coverage, amorphous (α_2) and crystalline (α_1) methanol multilayers appeared at 141 and 137 K; respectively. Saturation coverage slightly increased and reached to another convergence with the accumulation of multilayers of methanol. Current TPD spectra of methanol on the clean Ag(111) are in very good agreement with the former results in the literature [129].

IRAS spectra corresponding to the adsorption of methanol on clean Ag(111)

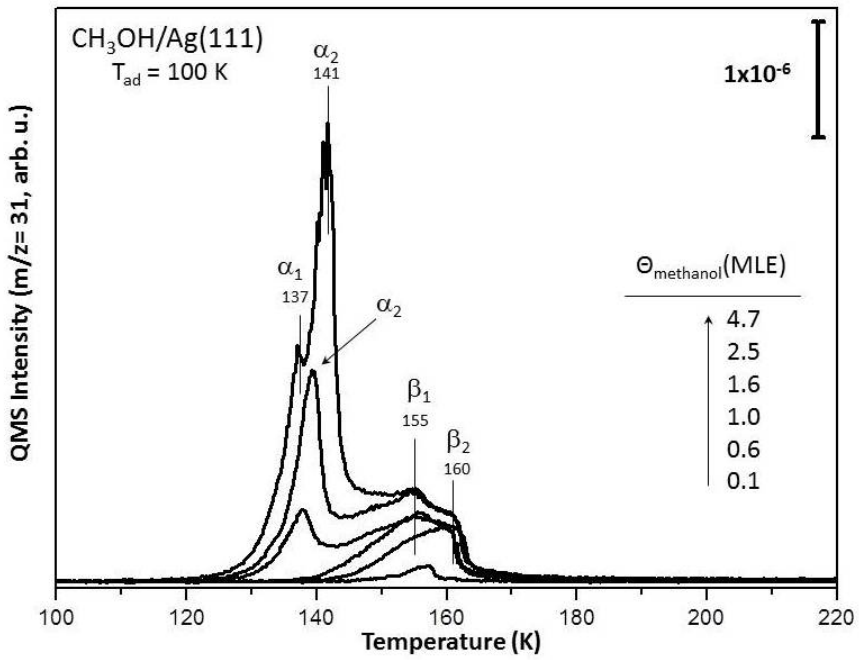

Figure 4.7: TPD profiles (m/z = 31) obtained after methanol adsorption on clean Ag(111) surface at 100 K as a function of increasing methanol coverage.

for various coverages of methanol at 100 K are given in Figure 4.8. For the lowest coverage of methanol ($\theta_{methanol}$ = 0.1 MLE), symmetric (ν_s) and antisymmetric (ν_{as}) CH_3 stretching signals appeared at 2820 cm^{-1} and 2953 cm^{-1}, respectively [130]. For 1.0 MLE methanol coverage, ν_{as} signal shifted to 2943 cm^{-1} and antisymmetric deformation overtone ($2\delta_{as}$) at 2917 cm^{-1} became more prominent. C-O stretching signal observed for both 0.2 and 1.0 MLE coverages of methanol at 1022 cm^{-1} and 1035 cm^{-1}, respectively. These C-H and C-O stretching signals and the lack of O-H signals for submonolayer methanol coverages ($\theta_{methanol} \leq$ 0.1 MLE) indicate that C-O bond axis in methanol molecule stays perpendicular to the silver surface; while O-H bond axis locates parallel to the surface. For multilayer methanol coverages($\theta_{methanol}$ = 1.6 and 4.7 MLE), ν_{as} (CH) signals broaden and two ν_s signals appeared at 2830 cm^{-1} and 2806 cm^{-1} suggesting variations in adsorption geometry of methanol in the multilayer coverage. In addition, broad ν (OH) band at 3297 cm^{-1} and ν (CO) signals at 1038 cm^{-1} and 1049 cm^{-1} for $\theta_{methanol}$ = 1.6 and 4.7 MLE coverages confirm the various adsorption geometries in the multilayer adsorption regime.

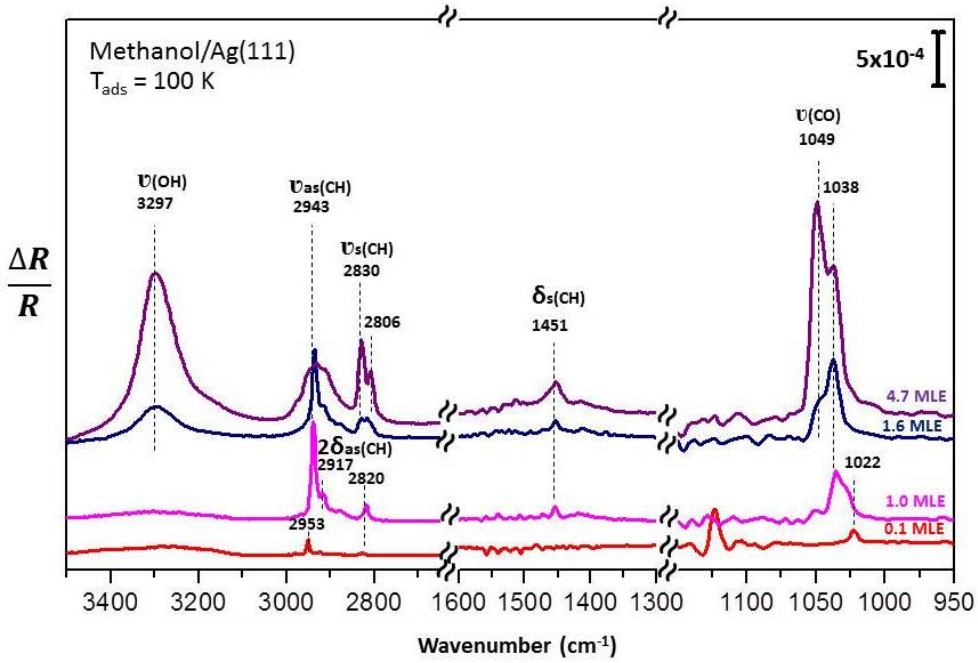

Figure 4.8: IRAS spectra of methanol adsorption on clean Ag(111) surface at 100 K as a function of methanol surface coverage.

4.3.2 Methanol on oxygen pre-covered Ag(111)

Methanol oxidation reactions were carried out on O/Ag(111) surfaces and the resulting products were followed in TPRS experiments. In order to prevent poisoning of the O/Ag(111) surface with excess methanol, a fixed methanol exposure (equivalent to 2 MLE coverage of methanol at 100 K) was dosed on the O/Ag(111) at 200 K (*i.e.* at a temperature above the desorption maximum of the first monolayer of methanol on clean Ag(111)). During TPRS experiments, m/z =31 (methanol), 32 (O_2, methanol), 30 (formaldehyde), 29 (formaldehyde, methanol), 28 (CO, formaldehyde, methanol), 44 (CO_2), 18 (H_2O) and 2 (H_2) desorption channels were simultaneously monitored. Two different sets of TPRS spectra for methanol oxidation reaction are presented in Figure 4.9, where the main difference between these different sets of spectra is the temperature of oxygen delivery.

TPRS spectra in Figure 4.9a corresponds to the presence of surface atomic

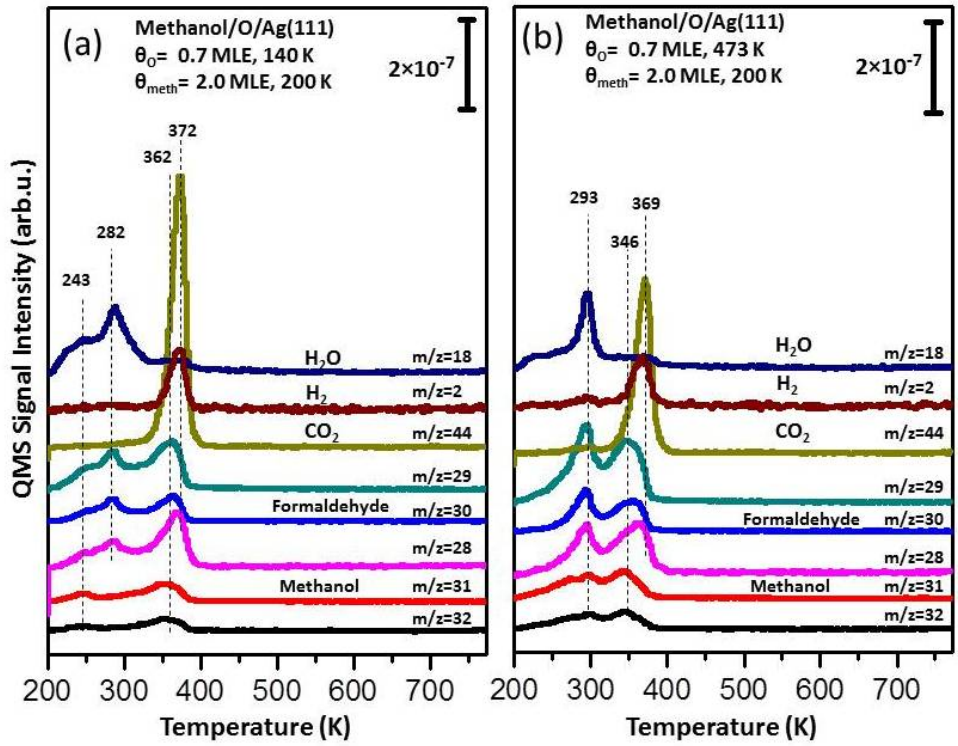

Figure 4.9: TPRS profiles for the reaction of methanol with oxygen on Ag(111). In all of the experiments, an identical exposure of methanol ($P_{methanol}$ = 1.0 x 10^{-9} Torr x 60 sec.) was dosed at 200 K on oxygen-covered (θ_O = 0.7 MLE) Ag(111) surface, where oxygen was delivered by ozone exposure either at (a) 140 K or at (b) 473 K

oxygen (O_a) species on Ag(111) obtained *via* oxygen delivery at 140 K and revealed the obvious reaction between surface oxygen species and methanol yielding formaldehyde as a partial oxidation product at 282 and 362 K; and CO_2 as a complete oxidation product at 372 K. No unreacted oxygen (m/z=32) was observed indicating consumption of all surface oxygen (O_a) species. In addition, methanol desorption was observed together with formaldehyde due to the disproportionation reaction of methoxy species formed after methanol adsorption on oxygen pre-covered Ag(111) surface [131]. It is worth mentioning that methanol desorption can not originate from molecular methanol adsorption due to the methanol dosage temperature (200 K) which is above the desorption maximum of the first monolayer on clean Ag(111). On the other hand, TPRS data given in Figure

4.9b corresponding to the interaction of methanol with the *p(5x1)* oxide overlayer (confirmed by LEED), a very similar extent of reaction between methanol and oxygen was observable. Concurrent desorption of methanol and formaldehyde at 298 K slightly increased while a small decrease in CO_2 desorption at 369 K was observed.

Methanol oxidation reactions on the Ag(111) single crystal surface as a function of oxygen coverage (where ozone was delivered at 140 K and methanol was delivered 200 K) were performed and the corresponding TPRS spectra of the selected products (*i.e.* formaldehyde, methanol, CO_2) are given in Figure 4.10. In Figures 4.10c-f, formaldehyde and methanol desorption were observed ∼350 K at low oxygen coverages (0.1 and 0.2 MLE) for both O_a and O_{ox} covered Ag(111) surfaces. With increasing oxygen coverage (θ_O = 0.7 MLE), a new formaldehyde and methanol desorption state appeared at 250 K. These low-temperature methanol and formaldehyde desorption states became dominant at $\theta_O = 1.3$ MLE oxygen coverage and the desorption states of methanol and formaldehyde appearing at ∼350 K vanished. An important conclusion that can be drawn from these observations is the fact that increasing oxygen coverage on Ag(111) decreases the oxidation temperature of methanol and facilitates the partial oxidation reaction (*i.e.* C-H and/or O-H bond activation).

Integrated desorption signals of the relevant products in Figure 4.10 were also calculated (after compensating for the interferences between various desorption signals due to mass spectroscopic fragmentation). These results are presented as histograms in Figure 4.11 revealing relative product selectivity for dissimilar oxygen coverages. In order to calculate total integrated TPRS signals of formaldehyde in Figure 4.10, mass spectroscopic fragment of formaldehyde m/z=30 signal was considered by referring to RGA fragments in Appendix B. Pure formaldehyde yields a total fragments to m/z=30 intensity ratio of 3.2 (100+73+59+3/73) upon fragmentation in the QMS. Hence m/z=30 integrated signal (I_{30}) should be multiplied by a factor of 3.2. However, m/z=30 channel has a small contribution from methanol and should be subtracted from the integrated m/z=30 signal (I_{30}) to calculate net formaldehyde quantity ($Q_{Formaldehyde}$) as given in Equation 4.1. Contribution of methanol in m/z=30 signal is 0.14 times the m/z=31 signal.

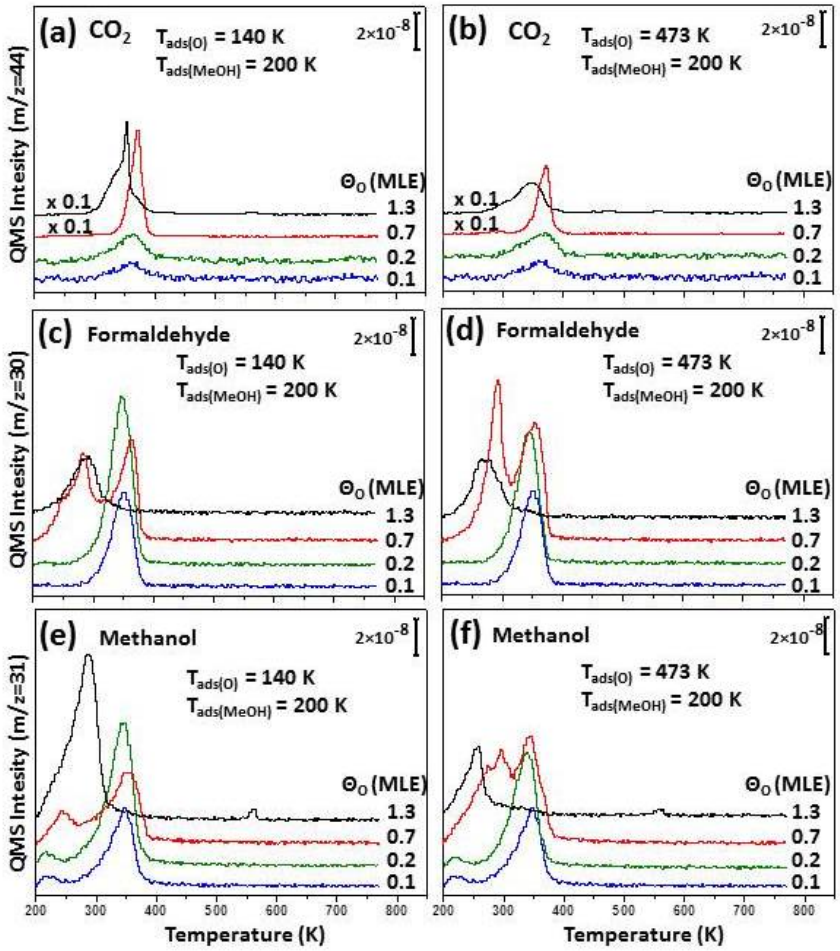

Figure 4.10: TPRS profiles of methanol oxidation reaction products (*i.e.* formaldehyde, methanol, CO_2) for the reaction between methanol (Tads=200 K) and oxygen pre-covered Ag(111) surfaces as a function of oxygen coverage.

In addition, m/z=31 signal was used to calculate total methanol quantity ($Q_{Methanol}$). Pure methanol yields a total fragments to m/z=31 intensity ratio of 3.0 (100+86+65+35+14/100) upon fragmentation in the QMS. Hence m/z=31 integrated signal (I_{31}) should be multiplied by a factor of 3.0. Calculation of the net methanol quantity is given in Equation 4.2. Very small contribution of formaldehyde to m/z=31 signal given in Equation 4.2 was ruled out. As can be seen in Figures 4.10 and 4.11, formaldehyde selectivity is higher for small oxygen coverages (θ_O = 0.1 and 0.2 MLE) and limited CO_2 production was observed for both O_a and O_{ox} covered surfaces. However, CO_2 production drastically increased

with increasing oxygen coverage for $\theta_O \geq 0.7$ MLE. While *p(5×1)* surface oxide (O_{ox}) including 0.7 MLE oxygen showed slightly higher total conversion yield and formaldehyde selectivity compared to equivalent O_a species, *c(4×8)* surface oxide (O_{ox}) including 1.3 MLE oxygen revealed much lower conversion in comparison with 1.3 MLE of O_a species.

$$Q_{Formaldehyde} = \left(\int I_{30}.\Delta T\right) \times 3.2 - \left(\int I_{31}.\Delta T\right) \times 0.14 \tag{4.1}$$

$$Q_{Methanol} = \left(\int I_{31}.\Delta T\right) \times 3.0 - \left(\int I_{30}.\Delta T\right) \times 0.05 \tag{4.2}$$

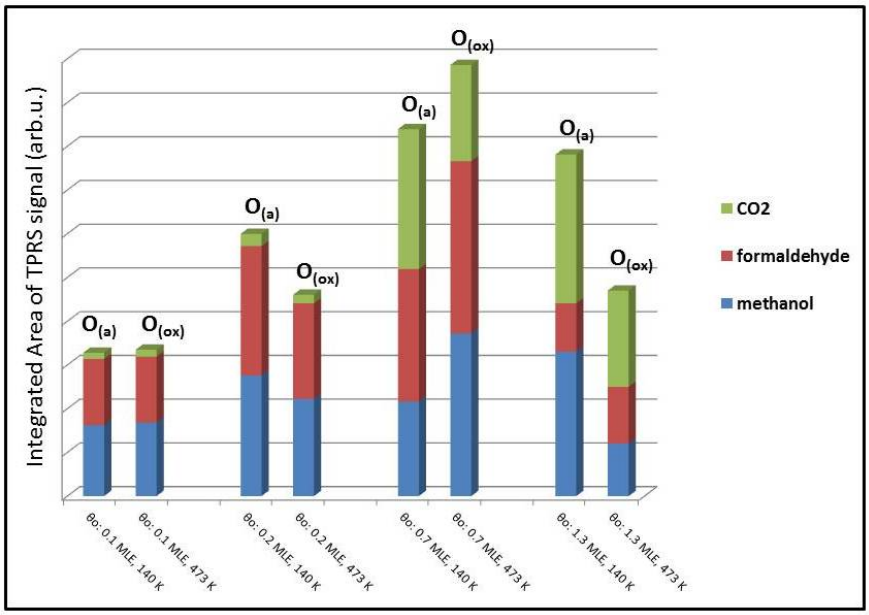

Figure 4.11: Integrated TPRS desorption signals for the methanol oxidation products (*i.e.* formaldehyde, methanol, CO_2) on O/Ag(111) surface including either O_a or O_{ox} species as a function of oxygen coverage extracted from the TPRS data given in Figure 4.10.

IRAS spectra corresponding to the adsorption of $\theta_{methanol} = 1$ MLE methanol at 100 K on O_a/Ag(111) for various oxygen coverages at 140 K are given in Figure 4.12. For lowest oxygen coverage (*i.e.* $\theta_O = 0.1$ MLE) in Figure 4.12, CH_3 symmetric stretching signal was observed at 2790 cm^{-1} and resulted a slight red-shift ($\sim$3 cm^{-1}) with increasing oxygen coverage (*i.e.* incresing methoxy concentration). An intense C-O stretching signal (ν(CO)) was observed at 1041 cm^{-1} for

$\theta_O = 0.1$ MLE oxygen coverage and a blue-shift ($\sim$3 cm^{-1}) was observed for $\theta_O =$ 0.2 MLE. Very broad ν(CO) signal was observed when the initial oxygen coverage was increased to 1.0 MLE. For all oxygen coverages, symmetric and antisymmetric 2δ (CH_3) overtones appeared at 2873 cm^{-1} and 2909 cm^{-1}, respectively. These signals are clearly different than CH_3 modes obtained after methanol adsorption on the clean Ag(111) (see Figure 4.8) and they indicate the formation of methoxy species due to the deprotonation of methanol on oxygen pre-covered Ag(111) surface [130]. In addition, O-H stretching signal was observed at 3631 cm^{-1} for low oxygen coverages ($\theta_O = 0.1$ and 0.2 MLE) in Figure 4.12 indicating deprotonation of the α-H of methanol by the oxygen atoms on Ag(111). Infrared vibrational frequencies of methoxy species on Ag(111) are given in Appendix C.

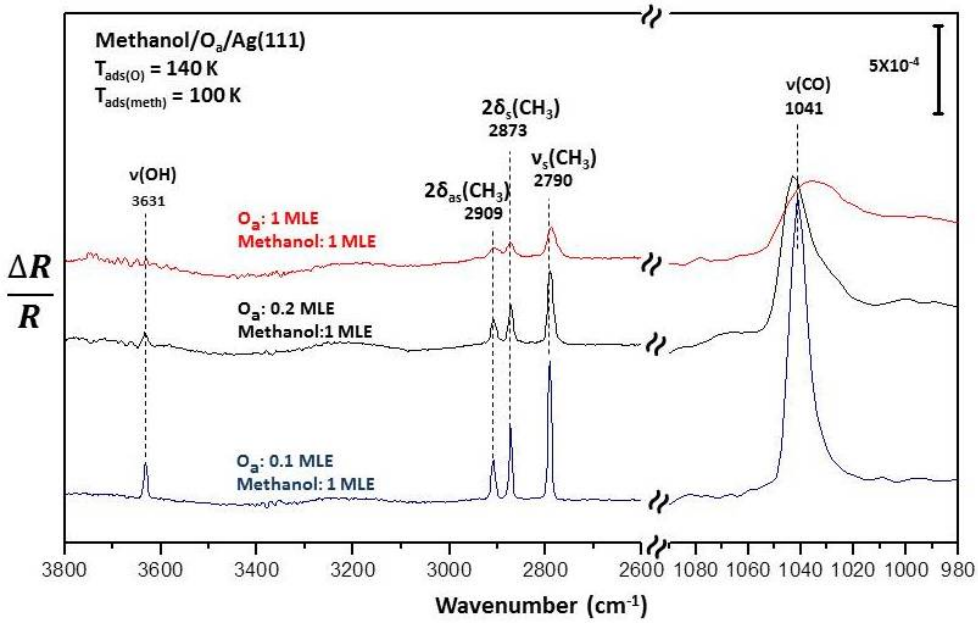

Figure 4.12: IRAS spectra of methanol (1.0 MLE) on O_a/Ag(111) for various oxygen coverages at 140 K

Observed ν(CO) signal $\sim$1041 cm^{-1} in Figure 4.12 indicates a perpendicular orientation of C-O bond of methoxy species to the surface plane. A gradual decrease in the intensities and increase in the FWHM values of all C-H, O-H and C-O signals with increasing initial oxygen coverage are probably due to increasing intermolecular interactions between adsorbed methoxy species on Ag(111) with increasing surface coverages and changing molecular orientation of methoxy

species towards tilted bond locations. Besides, red-shift in $\nu_s(CH_3)$ and blue-shift in $\nu(CO)$ modes with increasing methoxy coverage can be attributed to the competition between methoxy species for back-donated electron density [130]. As a result, increasing methoxy coverage strengthens the C-O bond while weakens the C-H bond. It is worth mentioning that the increasing quantity of methoxy species with increasing oxygen coverage was shown by TPRS in Figure 4.10 and Figure 4.11. Thus, the possibility of limited methanol adsorption with increasing oxygen amount (*i.e.* a competition of methanol and atomic oxygen for the available adsorption sites of Ag(111)) can be ruled out. Furthermore, orientational changes of the methoxy species with increasing oxygen coverage should also be closely related to surface reconstructions and morphology changes upon oxidation of the silver surface.

As a result, methanol molecules adsorbed on the clean Ag(111) surface *via* the oxygen atom with a perpendicular C-O bond orientation to the surface plane and desorbed in a reversible manner. When methanol was adsorbed on oxygen pre-covered Ag(111) surface, methoxy species was formed by O-H bond cleavage and α-H abstraction as shown in Equations 4.3 - 4.4 below. Formaldehyde formation (Equation 4.5) and desorption was observed after methoxy formation by TPRS experiments together with methanol desorption (Equation 4.6). C-H bond cleavage must be an intermediate step for formaldehyde formation. In addition, CO_2 desorption was also observed in the presence of excess oxygen atoms. CO_2 formation mechanism from methanol oxidation on Cu [131] and Au [111] surfaces was studied in the literature and formate was reported as an intermediate species (see Equations 4.7 - 4.9). Both O_a and O_{ox} species were found to be active in C-H and O-H bond cleavage. The product distribution of methanol oxidation reaction on Ag(111) single crystal surface is governed predominantly by the amount of oxygen species available on the catalyst with a possibly weaker contribution from the differences in the nature of these oxygen species.

$$CH_3OH(g) + O(a) \rightarrow CH_3O(a) + OH(a) \tag{4.3}$$

$$CH_3OH(g) + OH(a) \rightarrow CH_3O(a) + H_2O(a) \tag{4.4}$$

$$CH_3O(a) \rightarrow H_2CO(g) + H(a) \tag{4.5}$$

$$CH_3O(a) + H(a) \rightarrow CH_3OH(g) \tag{4.6}$$

$$H_2CO(a) + O(a) \rightarrow CH_2COO(a) \tag{4.7}$$

$$CH_2COO(a) \rightarrow HCOO(a) + H(a) \tag{4.8}$$

$$HCOO(a) \rightarrow CO_2(g) + H(a) \tag{4.9}$$

$$2H(a) \rightarrow H_2(g) \tag{4.10}$$

4.3.3 The Effect of Methanol Dosage Temperature to the Methanol Oxidation Reaction Pathways

Formation of the methoxy species when methanol is accumulated on oxygen pre-covered Ag(111) single crystal at 100 K was discussed in the previous subsection and the corresponding IRAS spectrum of methoxy species formed after 1.0 MLE methanol accumulation on $\theta_O = 0.7$ MLE of oxygen pre-covered Ag(111) surface is given in Figure 4.13*a*. When the Ag(111) single crystal containing methoxy species was annealed, methoxy species was found to be stable up to 300 K (Figure 4.13, spectrum *b*). As can be seen from the spectra a and b of Figure 4.13, C-H bond strengthens (blue-shift) while C-O bond weakens (*i.e.* red-shift) at 300 K in comparison to 100 K. However, when the same amount of methanol was accumulated on $\theta_O = 0.7$ MLE of oxygen pre-covered Ag(111) surface at 300 K, methoxy signals were completely disappeared and new signals that are characteristic for formate were observed (4.13c). Formate signals at 1320, 2807 and 2883 cm^{-1} in Figure 4.13c belong to ν_s(OCO), ν(CH) and 2δ(CH)/ν_{as}(OCO)+δ(CH) modes, respectively [132]. In the literature, four different adsorption configurations of formate species were identified by the oxidation of formic acid on Ag(111). Signals in spectrum c of Figure 4.13 belong to α-formate which adsorbs symmetrically on the surface by bridging from its oxygen atoms to two adjacent Ag atoms and C-H bond stays perpendicular to the surface plane [132].

TPRS experiments for the same conditions given in 4.13a and c were also performed and corresponding TPRS spectra are given in Figure 4.14. As can

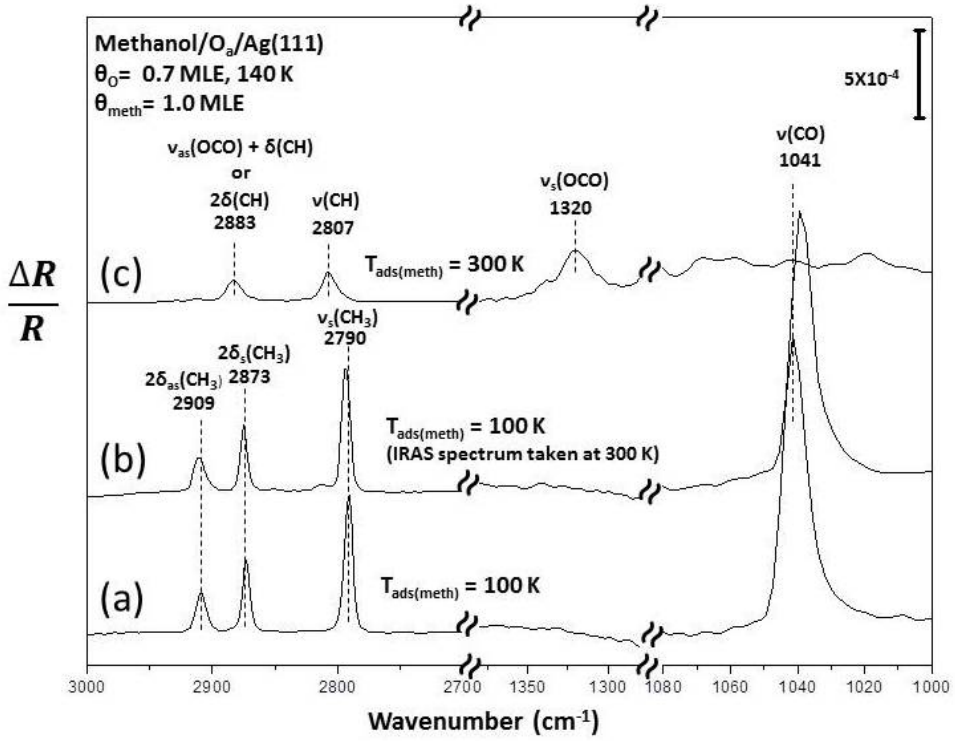

Figure 4.13: IRAS spectra of methanol (1.0 MLE) on O/Ag(111) ($\theta_O = 0.7$ MLE) for methanol accumulation temperature (a) at 100 K, (b) at 100 K followed by annealing to 300 K, (c) at 300 K.

be seen in Figure 4.14a, formaldehyde desorption appeared at 292 K, while CO_2 desorption was observed in the form of two separate states at 365 K and 483 K. A broad water desorption signal between 200-400 K also indicates methoxy formation by O-H bond activation of methanol molecules. However, no formaldehyde desorption was detected in Figure 4.14b when methanol was accumulated at 300 K although formate is stable at 300 K (4.13b). Despite the fact that formate species yield only CO_2, CO_2 desorption signal intensities at 373 K and 466 K in Figure 4.14b were unexpectedly lower than CO_2 signals in Figure 4.14a. Thus, it is very likely that the methanol quantity adsorbed on O_a/Ag(111) surface at 300 K is lower compared to that of the methanol adsorption at 100 K.

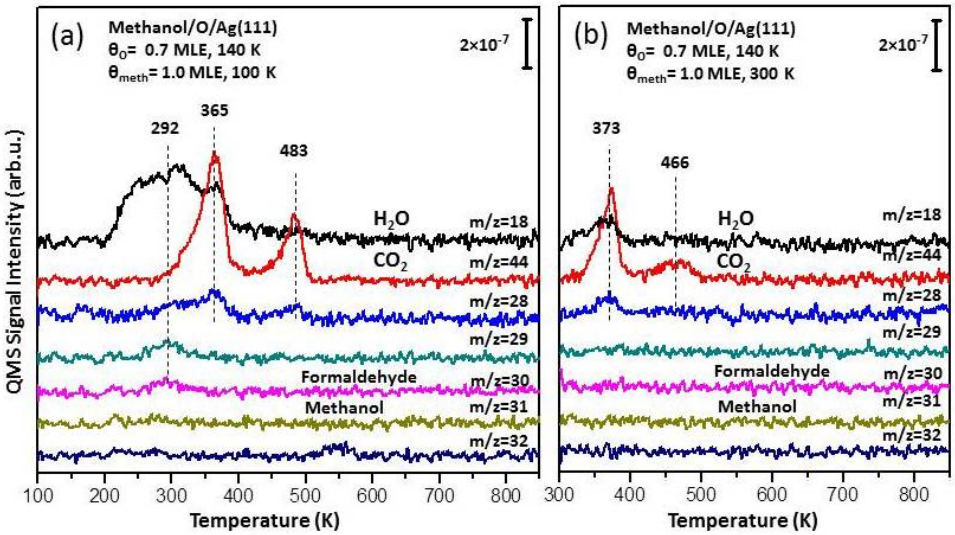

Figure 4.14: TPRS spectra of methanol (1.0 MLE) on O/Ag(111) (θ_O = 0.7 MLE) for methanol accumulation temperature (a) at 100 K and (b) at 300 K.

4.4 N-H Activation on Ag(111)

4.4.1 Ammonia on Clean Ag(111)

Ammonia adsorption was carried out on the clean Ag(111) surface at 90 K and m/z=17 signal was monitored in TPD experiments along with m/z=28, 18, and 2 signals in order to check the presence of potential decomposition products and water desorption from background adsorption (Figure 4.15). RGA of ammonia was given in Appendix B. In all of the TPD experiments, ammonia was found to desorb molecularly in a reversible manner from the clean Ag(111) single crystal surface, where no ammonia decomposition products, namely N_2 and H_2 desorption were detectable at any ammonia coverage. In Figure 4.15, two ammonia desorption maxima located at 138 K and 120 K were observed for the lowest ammonia coverage of $\theta_{NH3} = 0.10$ MLE. With increasing ammonia coverage, desorption signal at 120 K became broader and its desorption maximum shifted to lower temperatures. Broadening and the low-temperature shift with increasing ammonia coverage in the sub-monolayer range is a common behavior of ammonia TPD profiles obtained from numerous metal surfaces such as Pt(111) [122],

Au(111) [125], Rh(111) [123], and Ir(100) [124] which can be attributed to heterogeneity of the adsorbed ammonia species, as well as repulsive interactions (or decreasing attractive interactions) between the adsorbates in the first monolayer [67]. Figure 4.15 shows that the major ammonia desorption feature at 110 K reached saturation which was immediately followed by the appearance of an additional desorption maximum at 98 K that can be assigned to the formation of multilayer ammonia overlayers.

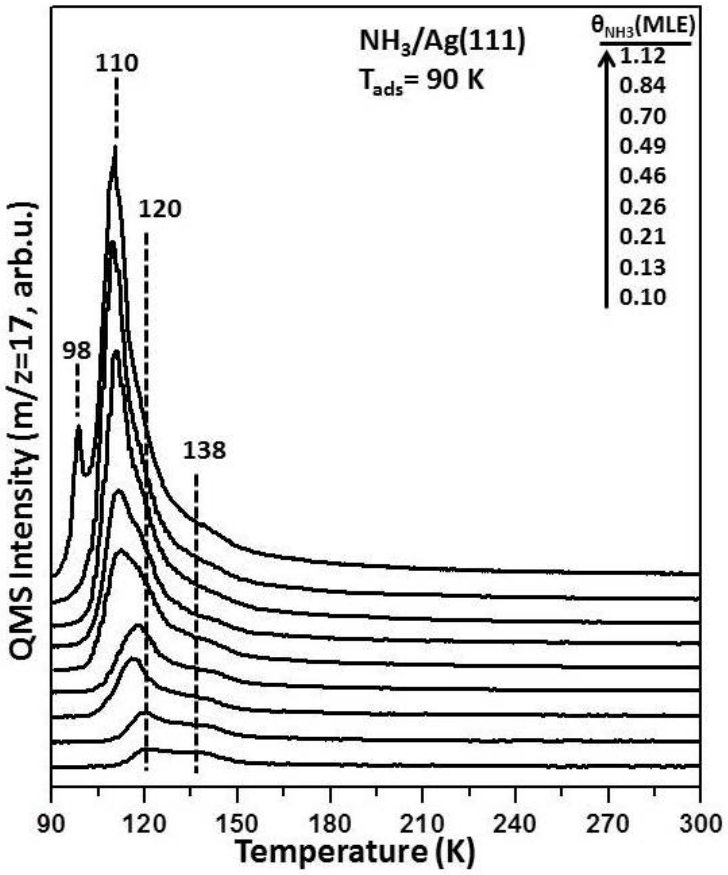

Figure 4.15: TPD profiles (m/z=17) obtained after ammonia adsorption on clean Ag(111) surface at 90 K as a function of increasing ammonia coverage.

TPD data given in Figure 4.15 can be used to estimate the relative ammonia surface coverages. For this purpose, the multilayer signal at 98 K was deconvoluted and subtracted from the whole desorption spectrum and the integrated desorption signal between 90 K and 480 K associated with the desorption maximum at 110 K was used to estimate $\theta_{NH3} = 1$ MLE. It is worth mentioning that

TPD experiments were also performed for ammonia coverages greater than 1.12 MLE, revealing a typical zero-order desorption kinetics. In the literature, analogous monolayer and multilayer ammonia desorption signals were also observed on other metal surfaces [123], [124] as well as on Ag(110) [133]. The less-prominent ammonia desorption signal at 138 K in Figure 4.15 can be attributed to stronger ammonia adsorption on surface defects and/or adsorption of ammonia with dissimilar geometries/orientations on different surface adsorption sites. In overall, TPD results for NH_3 adsorption on clean Ag(111) given in Figure 4.15 clearly point out to the fact that in the absence of oxygen species, Ag(111) is incapable of activating NH_3. On the other hand, as will be shown below, ammonia activation and its selective catalytic oxidation is achievable by fine-tuning the nature and surface coverage of oxygen species on Ag(111).

IRAS spectra corresponding to the adsorption of ammonia on clean Ag(111) for various coverages of ammonia at 90 K are given in Figure 4.16. For the lowest coverage of ammonia ($\theta_{NH3} = 0.21$ MLE), symmetric (δ_s) and antisymmetric (δ_{as}) NH_3 deformation signals appeared at 1072 cm^{-1} and 1618 cm^{-1}, respectively; while symmetric (ν_s) and antisymmetric (ν_{as}) NH_3 stretching modes can be seen at 3275 cm^{-1} and 3390 cm^{-1}, respectively [133]. For sub-monolayer coverages, it is commonly observed that ammonia molecules are typically adsorbed on transition metal surfaces through unpaired electrons of nitrogen and the molecular axis stays perpendicular to the surface [134]. In such cases, δ_{as} and ν_{as} modes cannot be observed as reported in the literature for ammonia adsorption on Ni(111) [135], Ru(0001) [136], Pt(111) [137], and Cu(110) [138]. In contrast, IRAS data in Figure 4.16 suggest that on clean Ag(111) surface, molecular axis of ammonia is tilted with respect to the Ag(111) surface for sub-monolayer coverages. A similar behavior was also observed for ammonia adsorption on clean Ag(110) via Electron Energy Loss Spectroscopy (EELS) [133]. For the IRAS spectrum corresponding to $\theta_{NH3} = 0.84$ MLE, δ_s signal was found to vanish and NH_3 stretching modes were observed to broaden and shift to lower frequencies, namely to 3347 cm^{-1} and 3266 cm^{-1}. These changes in the IRAS spectra are probably due to increasing intermolecular interactions between adsorbed ammonia molecules on Ag(111) with increasing surface coverages as well as due to the formation

of hydrogen bonding interactions. Loss of the δ_s-feature was also reported on NH_3/Ru(0001) by Rodriquez *et al.* for the second layer of (*i.e.* multilayer) ammonia on Ru(0001) and was attributed to the formation of intermolecular hydrogen bonding and/or smaller IR absorption cross section of the ammonia molecules in the second layer [136].

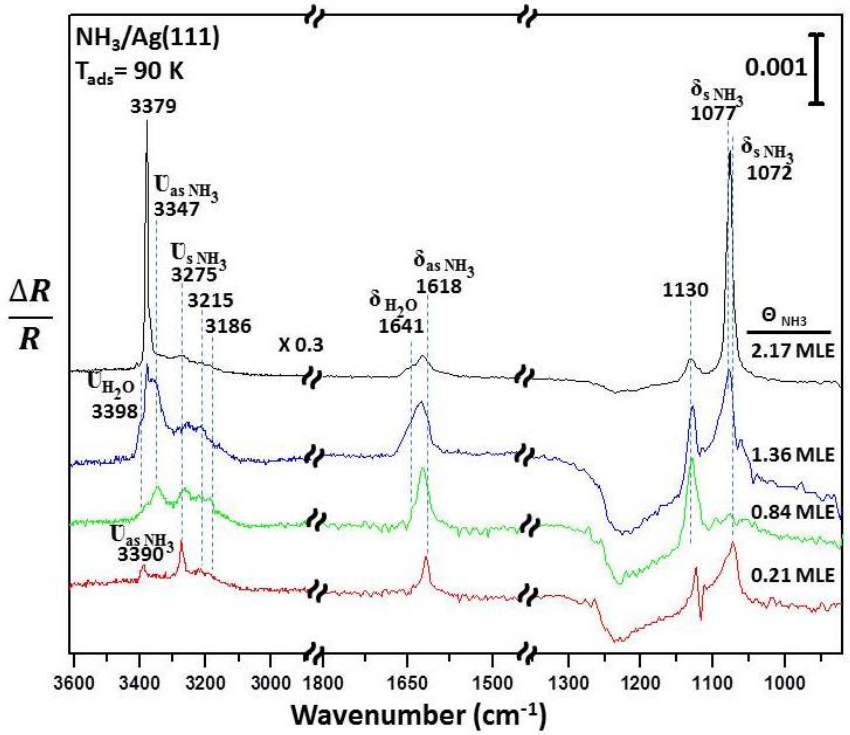

Figure 4.16: IRAS spectra of ammonia adsorption on clean Ag(111) surface at 90 K as a function of ammonia surface coverage.

IRAS spectrum corresponding to $\theta_{NH3} = 0.84$ MLE also revealed water stretching and bending signals due to background water adsorption located at 3398 cm^{-1} and 1641 cm^{-1}, respectively [139]. Furthermore, IRAS signals at 3186 cm^{-1} and 3215 cm^{-1} might be related to hydronium ions and hydrogen bonded water molecules located on the surface or on ammonia overlayer with different orientations [139]. When the ammonia coverage was increased to 1.36 MLE, symmetric deformation mode (δ_s) at 1072-1077 cm^{-1} reappeared and the antisymmetric (ν_{as}) NH_3 stretching signal became broader. Furthermore, at $\theta_{NH3} = 2.17$ MLE an additional sharp signal appeared at 3379 cm^{-1} which can be assigned to the

formation of solid multilayer ammonia [137]. These results are in very good agreement with the former reports in the literature for multilayer ammonia adsorption on various single crystals [136, 140]. Vibrational frequencies of NH_3 on Ag(111) for different NH_3 coverages obtained by the currently presented IRAS spectra are given in Table 4.1. IRAS data given in Figure 4.16 for NH_3/Ag(111) is in agreement with the corresponding TPD data presented in Figure 4.15, suggesting molecular adsorption (*i.e.* lack of dissociation) of ammonia on Ag(111) in the absence of additional oxygen species.

Table 4.1: Vibrational frequency assignments for the NH_3/Ag(111) IRAS data presented in Figure 4.16

Chemical/Mode (cm^{-1})	δ_s(HNH)	δ_{as}(HNH)	ν_s(NH)	ν_{as}(NH)
NH_3 on Ag(111) (θ_{NH3} = 0.21 MLE)	1072	1618	3275	3390
NH_3 on Ag(111) (θ_{NH3} = 0.84 MLE)	-	1640	3266	3347
		1625		
NH_3 on Ag(111) (θ_{NH3} = 1.36 MLE)	1077	1625	3257	3379
		1651		3358
NH_3 on Ag(111) (θ_{NH3} = 2.17 MLE)	1077	1625	3275	3379
		1651		
NH_3 on Ag(110) (submonolayer) [133]	1050	1640	3320	3400
Solid NH_3 [133]	1060	1646	3223	3378

4.4.2 Ammonia on Oxygen Pre-covered Ag(111)

Ammonia Selective Catalytic Oxidation (SCO) reaction was carried out on O/Ag(111) and the resulting products were followed in TPRS experiments. In order to prevent poisoning of the O/Ag(1111) surface with excess ammonia, NH_3 was dosed on the O/Ag(111) at 250 K (*i.e.* at a temperature above the desorption maximum of the first monolayer of ammonia on clean Ag(111)). During TPRS experiments, m/z=17 (NH_3), 28 (N_2), 30 (NO), 44 (N_2O), 46 (NO_2), 32 (O_2), 18 (H_2O) and 2 (H_2) desorption channels were simultaneously monitored.

Two different sets of TPRS spectra for oxygen-ammonia reaction are presented in Figure 4.17, where the main difference between these different sets of spectra is

the temperature of oxygen delivery. While the oxygen delivery at 140 K (multi-colored spectra) led to surface atomic oxygen (O_a) species on Ag(111), oxygen delivery at 473 K (grey spectra) resulted in the formation of a *p(5x1)* surface oxide.

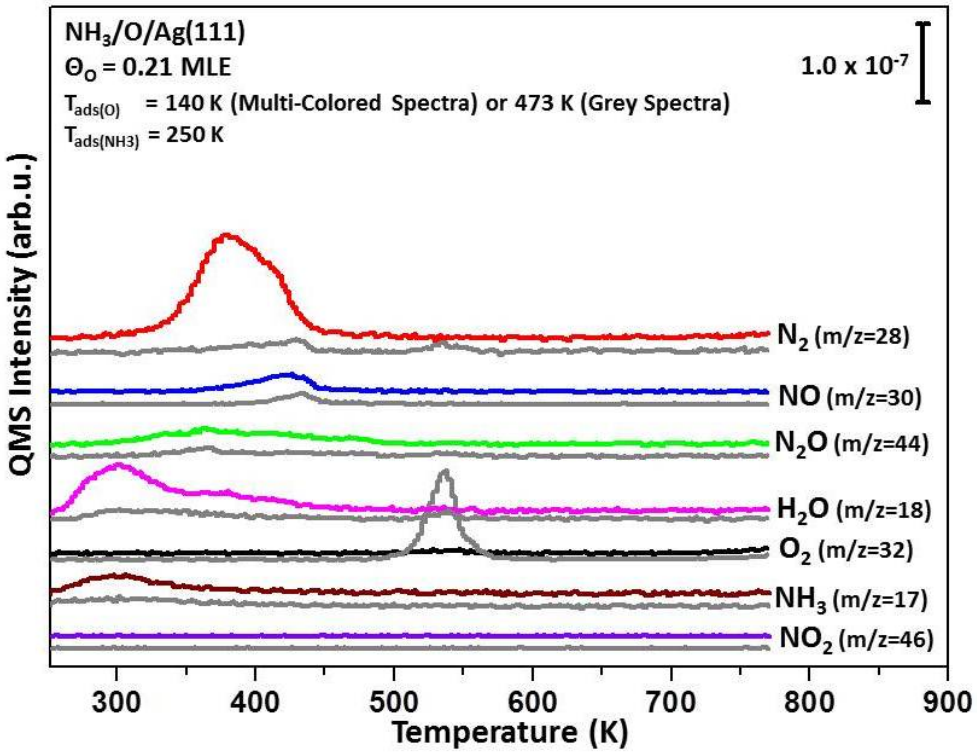

Figure 4.17: TPRS profiles for the reaction of ammonia with oxygen on Ag(111). In all of the experiments, an identical exposure of NH_3 (P_{NH3} = 2.0 x 10^{-9} Torr x 60 s) was dosed at 250 K on oxygen-covered (θ_O = 0.21 MLE) Ag(111) surface, where oxygen was delivered by ozone exposure either at 140 K (multi-colored spectra) or at 473 K (grey-colored spectra).

Multi-colored TPRS spectra in Figure 4.17 corresponding to the presence of surface atomic oxygen (O_a) species on Ag(111) obtained *via* oxygen delivery at 140 K revealed the obvious reaction between surface oxygen species and ammonia yielding SCO products such as N_2 (red), NO (blue) and N_2O (green) in a wide temperature range between 300-450 K. In addition, water desorption within the same temperature range was also in line with the N-H bond activation and hydrogen abstraction from ammonia by surface oxygen atoms on Ag(111). Neither unreacted oxygen nor NO_2 formation were detectable for the multi-colored TPRS

data.

On the other hand, for the grey-colored TPRS data given in Figure 4.17 corresponding to the interaction of ammonia with the *p(5x1)* oxide overlayer (confirmed by LEED), a very limited extent of reaction between ammonia and oxygen was observable. Strikingly intense desorption signal of the unreacted oxygen species at 537 K was consistent with the limited ammonia oxidation by the oxide overlayer. A similar behavior was also reported by Madix and co-workers for CO oxidation on Ag(111) suggesting that silver oxide overlayer was not the most reactive phase for CO oxidation reaction [141]. Thus, comparative analysis of the TPRS data shown in Figure 4.17 pointed to the fact that surface atomic oxygen (O_a) on Ag(111) could readily activate N-H bond cleavage in NH_3, while ordered silver oxide (O_{ox}) overlayers had limited activity for ammonia oxidation.

NH_3 SCO reaction on the Ag(111) single crystal surface containing different quantities of oxygen (delivered by ozone exposure at 140 K) were performed and the corresponding TPRS spectra of the selected products (i.e. N_2, NO, N_2O) are given in Figure 4.18. Alternative depictions of the same set of data were also provided in Appendix D. Integrated desorption signals of the relevant products in Figure 4.18 were also calculated (after compensating for the interferences between various desorption signals due to mass spectroscopic fragmentation). These results are presented as histograms in Figure 4.19 revealing relative ammonia SCO selectivity for dissimilar oxygen coverages. In order to calculate total integrated TPRS signals of N_2O in Figure 4.19, mass spectroscopic fragments of N_2O other than m/z=44 were also considered. By referring to the National Institute of Standards and Technology (NIST) mass spectroscopy database [142], relative intensities of the main fragments of N_2O were obtained as 100%, 32% and 11% for m/z=44, 30 and 28, respectively. Accordingly, the integrated m/z=44 desorption signal was multiplied by a factor of 1.43 (100+32+11/100). On the other hand, contribution of N_2O to the NO and N_2 integrated signals were subtracted (removed) from the integrated m/z=30 and 28 signals. Calculation of the net quantities of N_2, NO and N_2O molecules are given in Equations 4.11, 4.12 and 4.13, respectively. As can be seen in Figures 4.18 and 4.19, the main ammonia SCO product for low oxygen coverages (*i.e.* 0.13 MLE $< \theta_O <$ 1.10 MLE) was

clearly N_2 and the maximum N_2 formation was obtained for $\theta_O = 0.21$ MLE. It is also apparent that NO selectivity increased drastically for $\theta_O = 1.10$ MLE and became comparable to that of N_2.

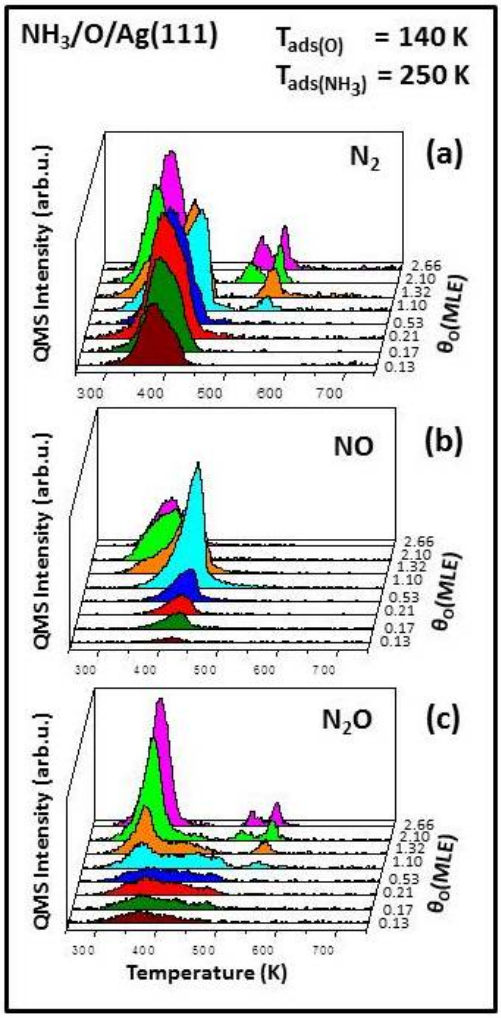

Figure 4.18: TPRS profiles of various ammonia SCO reaction products (i.e. N_2, NO, N_2O) for the reaction between ammonia and oxygen pre-covered Ag(111) surfaces as a function of oxygen coverage. For all of the data, oxygen was delivered on Ag(111) by ozone exposure at 140 K, while NH_3 was delivered using an identical ammonia exposure at 250 K (P_{NH3} = 2.0 x 1010^{-9} Torr x 60 s)

$$Q_{N_2} = \left(\int I_{28}.\Delta T\right) - \left(\int I_{44}.\Delta T\right) \times 0.11 \tag{4.11}$$

$$Q_{NO} = \left(\int I_{30}.\Delta T\right) - \left(\int I_{44}.\Delta T\right) \times 0.32 \tag{4.12}$$

$$Q_{N_2O} = \left(\int I_{44}.\Delta T\right) \times 1.43 \tag{4.13}$$

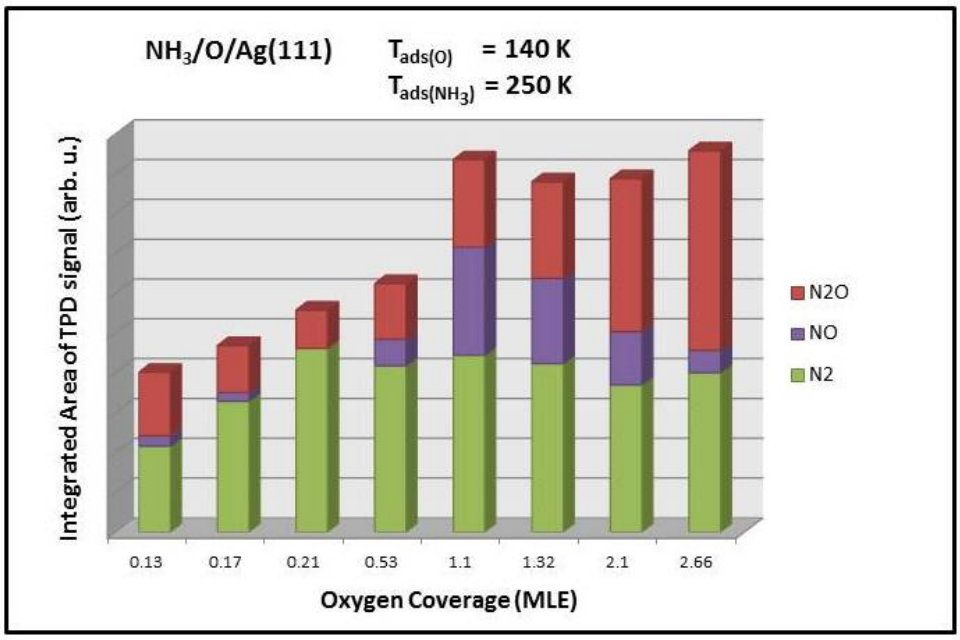

Figure 4.19: Integrated TPD desorption signals for the main ammonia SCO products (i.e. N_2, NO, N_2O) on O/Ag(111) surface as a function of oxygen coverage extracted from the TPRS data given in Figure 4.18.

It is worth mentioning that N_2 desorption maxima shifted to higher temperatures for $\theta_O \geq 1.10$ MLE (Figure 4.18a) and additional N_2 desorption states also became visible. This observation was concomitant to the appearance of excess oxygen desorption associated with surface and subsurface/bulk oxide states. Thus, it can be argued that formation of oxide species abundant in oxygen led to an attractive interaction between oxygen species and atomic nitrogen, resulting in the stabilization of the atomic nitrogen species generated by N-H bond activation of NH_3 and a shift in the N_2 desorption maxima to higher temperatures. Furthermore, generation of additional high temperature N_2 desorption states at elevated oxygen coverages can also be attributed to the increasing heterogeneity

of the adsorption sites of the substrate surface due to the formation of bulk-like silver oxide.

Furthermore, unreacted NH_3 was also monitored (see Appendix E) for the set of experiments presented in Figure 4.18. These results revealed limited amounts of ammonia desorption (*i.e.* lack of presence of excess ammonia) suggesting a high conversion of ammonia for the particular set of experimental conditions chosen for Figure 4.18.

It is worth mentioning that IRAS measurements were also performed at 250 K for SCO of ammonia on atomic oxygen (O_a) covered Ag(111) surface using experimental conditions (coverages) similar to the ones chosen for the TPRS experiments given in Figure 4.18. However no IRAS signals were detected possibly due to the unfavorable adsorption geometry or small IR absorption cross sections of the reactants and products lying, possibly close to parallel to the surface.

Chapter 5

Conclusions

In the current thesis study, nature of oxygen on Au(111) and Ag(111) single crystals was investigated by utilizing a multitude of surface-sensitive spectroscopic and diffraction techniques. Ozone decomposition method was used as an oxygen delivery agent under UHV conditions. TPD/TPRS, XPS and LEED data suggest that a variety of oxygen species can be generated on the Ag(111) surface upon ozone adsorption depending on the oxygen quantity and accumulation temperature. Activity of different oxygen species towards O-H, C-H, C-C and N-H bond cleavage was determined on both Au(111) and Ag(111) single crystal surfaces.

5.1 Bond Activation by Au(111)

Three different oxygen species were generated on the Au(111) single crystal upon ozone adsorption such as surface atomic oxygen (O_a), subsurface oxygen (O_{sub}) and surface oxide (O_{ox}). Oxygen accumulation on Au(111) surface at 140 K for θ_O<1.0 MLE of oxygen coverage resulted in surface atomic oxygen (O_a) formation, while 2D surface oxide (O_{ox}) started to grow for θ_O>1.0 MLE of oxygen coverage at the same temperature. It was also revealed that oxygen atoms dissolve (O_{sub}) in the bulk of the Au(111) single crystal when oxygen is accumulated

at 473 K.

Methanol, acetaldehyde and ammonia TPD experiments revealed that clean Au(111) single crystal is incapable of activating O-H, C-H, C-C and N-H bonds of these molecules in the absence of oxygen atoms. Surface atomic oxygen species (O_a) prepared at 140 K were found to be very active for O-H and C-H cleavage producing formaldehyde, methyl formate, CO_2 as partial/complete oxidation products of methanol. O_a was found to be capable of activating C-C bond of acetaldehyde producing two different partial oxidation products namely, methyl acetate and acetic acid without the formation of significant quantities of carbon dioxide. In addition to the generation of these products; indications of the polymerization of acetaldehyde on the gold surface were also observed as an additional catalytic route competing with the partial/total oxidation pathways. O_a was also active for N-H bond cleavage of ammonia molecules and showed very high selectivity towards N_2 formation rather than other toxic gases such as NO, NO_2 and N_2O formation.

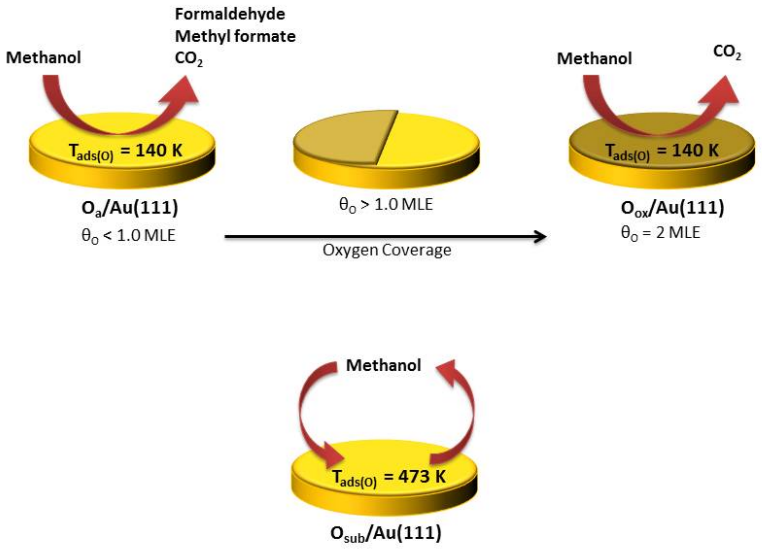

Figure 5.1: Reactivity and selectivity trends of methanol oxidation reaction on O/Au(111) as a function of oxygen coverage and temperature.

Surface oxide (O_{ox}) overlayer prepared on Au(111) for θ_O>1.0 MLE at 140 K was also found to be very active towards methanol. However it showed very high selectivity towards CO_2 in the methanol oxidation reactions. In addition, dissolved oxygen atoms (O_{sub}) prepared at 473 K for all coverages revealed almost no activity in methanol oxidation reactions. Overall reactivity and selectivity trends of methanol oxidation on O/Au(111) as function of adsorption temperatures, oxygen surface coverages and nature of the oxygen species deduced from the currently presented experimental findings are summarized in Scheme 5.1.

5.2 Bond Activation by Ag(111)

Three different oxygen species were generated on the Ag(111) surface upon ozone adsorption such as surface atomic oxygen (O_a), surface oxide (O_{ox}) and bulk-like oxide (O_{bulk}) species. Indications of oxygen transport to the subsurface region of silver at elevated ozone exposures were also detected. Oxygen overlayers prepared *via* ozone exposure at 140 K in UHV led to disordered overlayers (either in the form of atomic oxygen or bulk-like silver oxide) for all oxygen coverages, while annealing of these overlayers for intermediate oxygen coverages at 473 K resulted in the formation of ordered surface oxides with *p(5x1)* and *c(4x8)* structures.

Clean Ag(111) surface was found to be incapable of activating O-H and C-H bonds of methanol as well as N-H bonds of ammonia under UHV conditions in the absence of ozone exposure. IRAS experiments revealed that methanol molecules locate on the clean Ag(111) surface *via* the oxygen atom with a perpendicular C-O bond orientation to the surface plane. IRAS results also suggested that ammonia molecules are adsorbed on Ag(111) surface through unpaired electrons of nitrogen and the molecular axis of ammonia is tilted with respect to the Ag(111) surface for sub-monolayer coverages.

Disordered atomic oxygen (O_a) and surface oxide (O_{ox}) overlayers prepared on Ag(111) for $\theta_O \leq 0.2$ MLE were found to be very active for O-H and C-H bond cleavage producing formaldehyde as the dominant product. Increasing oxygen

quantity for both oxygen species (0.7 MLE $\leq \theta_O \leq$ 1.3 MLE) resulted mostly CO_2 formation indicating that the product distribution of methanol oxidation reaction on Ag(111) surface depends on the oxygen quantity. Another factor effecting the product distribution of methanol oxidation reaction was found to be methanol accumulation temperature. While methanol dosage at 100 K on atomic oxygen covered Ag(111) surface revealed methoxy formation followed by formaldehyde and methanol desorption, methanol accumulation at 300 K generated only formate species which yield CO_2.

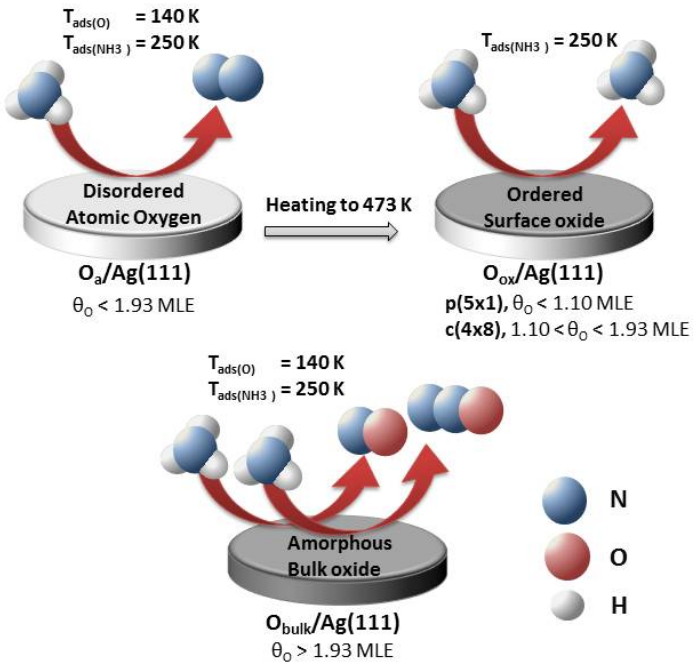

Figure 5.2: Reactivity and selectivity trends of ammonia SCO on O/Ag(111) as a function of oxygen coverage and temperature.

Disordered atomic oxygen overlayers (O_a) prepared on Ag(111) at 140 K for $\theta_O < 1.10$ MLE were found to be highly selective in SCO of ammonia, producing N_2 as the dominant product. On the other hand, ordered p(5×1) and c(4×8) surface oxide (O_{ox}) overlayers on Ag(111) prepared *via* ozone adsorption at 473 K were found to be almost entirely inactive in SCO where NH_3 and O_2 desorbed

in an intact manner in TPRS experiments. It was observed that extreme oxygen exposures on Ag(111) ($\theta_O > 1.93$ MLE) at 140 K led to bulk-like silver oxide (O_{bulk}) species with poor N_2 selectivity in ammonia SCO and increasing extent of formation of toxic pollutants such as NO and N_2O. Overall reactivity and selectivity trends of ammonia SCO on O/Ag(111) as function of adsorption temperatures, oxygen surface coverages and nature of the oxygen species deduced from the currently presented experimental findings are summarized in Scheme 5.2.

Currently presented experimental findings on Ag(111) single crystal model catalyst surface reveal valuable insights as well as new structure-functionality relationships at the molecular level regarding the reactivity of oxygen species in ammonia SCO. These findings may also possibly be relevant to other crucial heterogeneous catalytic oxidation/partial oxidation/oxidative coupling processes of CO, alkenes and alcohols.

Bibliography

[1] J. White and C. T. Campbell, "Surface chemistry in heterogeneous catalysis: An emerging discipline," *J. Chem. Educ*, vol. 57, no. 7, p. 471, 1980.

[2] J. M. Thomas and W. J. Thomas, *Principles and practice of heterogeneous catalysis*. John Wiley & Sons, 1997.

[3] X. Liu, R. J. Madix, and C. M. Friend, "Unraveling molecular transformations on surfaces: a critical comparison of oxidation reactions on coinage metals," *Chemical Society Reviews*, vol. 37, no. 10, pp. 2243–2261, 2008.

[4] M. Qian, M. Liauw, and G. Emig, "Formaldehyde synthesis from methanol over silver catalysts," *Applied Catalysis A: General*, vol. 238, no. 2, pp. 211–222, 2003.

[5] R. A. Sheldon, I. Arends, and A. Dijksman, "New developments in catalytic alcohol oxidations for fine chemicals synthesis," *Catalysis Today*, vol. 57, no. 1, pp. 157–166, 2000.

[6] T. W. G. Solomons, C. B. Fryhle, and S. A. Snyder, *Organic Chemistry*. John Wiley & Sons, 2014.

[7] D. I. Enache, J. K. Edwards, P. Landon, B. Solsona-Espriu, A. F. Carley, A. A. Herzing, M. Watanabe, C. J. Kiely, D. W. Knight, and G. J. Hutchings, "Solvent-free oxidation of primary alcohols to aldehydes using Au-Pd/TiO_2 catalysts," *Science*, vol. 311, no. 5759, pp. 362–365, 2006.

[8] S. Biella and M. Rossi, "Gas phase oxidation of alcohols to aldehydes or ketones catalysed by supported gold," *Chemical Communications*, no. 3, pp. 378–379, 2003.

[9] A. Wittstock, V. Zielasek, J. Biener, C. Friend, and M. Bäumer, "Nanoporous gold catalysts for selective gas-phase oxidative coupling of methanol at low temperature," *Science*, vol. 327, no. 5963, pp. 319–322, 2010.

[10] L. Chmielarz and M. Jabłońska, "Advances in selective catalytic oxidation of ammonia to dinitrogen: a review," *RSC Advances*, vol. 5, no. 54, pp. 43408–43431, 2015.

[11] J. E. Huheey, E. Keiter, and R. Keiter, *Inorganic Chemistry-Principles of Structure and Reactivity*. Harper Collins College Publishers, New York, 1993.

[12] D. R. Lide, "CRC handbook of chemistry and physics," *12J204*, 1947.

[13] G. Somorjai, "Active sites in heterogeneous catalysis," *Advances in catalysis*, vol. 26, pp. 1–68, 1977.

[14] J. Gong, "Structure and surface chemistry of gold-based model catalysts," *Chemical reviews*, vol. 112, no. 5, pp. 2987–3054, 2011.

[15] M. Pan, J. Gong, G. Dong, and C. B. Mullins, "Model studies with gold: a versatile oxidation and hydrogenation catalyst," *Accounts of chemical research*, vol. 47, no. 3, pp. 750–760, 2013.

[16] M. Dean and M. Bowker, "Adsorption studies on catalysts under UHV/HV conditions: I. oxygen adsorption on alumina supported silver," *Applied surface science*, vol. 35, no. 1, pp. 27–40, 1988.

[17] G. C. Bond, P. A. Sermon, G. Webb, D. A. Buchanan, and P. B. Wells, "Hydrogenation over supported gold catalysts," *Journal of the Chemical Society, Chemical Communications*, no. 13, pp. 444b–445, 1973.

[18] G. J. Hutchings, "Vapor phase hydrochlorination of acetylene: Correlation of catalytic activity of supported metal chloride catalysts," *Journal of Catalysis*, vol. 96, no. 1, pp. 292–295, 1985.

[19] M. Haruta, T. Kobayashi, H. Sano, and N. Yamada, "Novel gold catalysts for the oxidation of carbon monoxide at a temperature far below 0 ^{o}C," *Chemistry Letters*, vol. 16, no. 2, pp. 405–408, 1987.

[20] G. C. Bond and D. T. Thompson, "Catalysis by gold," *Catalysis Reviews*, vol. 41, no. 3-4, pp. 319–388, 1999.

[21] A. S. K. Hashmi and G. J. Hutchings, "Gold catalysis," *Angewandte Chemie International Edition*, vol. 45, no. 47, pp. 7896–7936, 2006.

[22] B. Xu, R. J. Madix, and C. M. Friend, "Predicting gold-mediated catalytic oxidative-coupling reactions from single crystal studies," *Accounts of chemical research*, vol. 47, no. 3, pp. 761–772, 2014.

[23] B. Min, A. Alemozafar, D. Pinnaduwage, X. Deng, and C. Friend, "Efficient co oxidation at low temperature on au (111)," *The Journal of Physical Chemistry B*, vol. 110, no. 40, pp. 19833–19838, 2006.

[24] T. A. Baker, B. Xu, X. Liu, E. Kaxiras, and C. M. Friend, "Nature of oxidation of the Au (111) surface: Experimental and theoretical investigation," *The Journal of Physical Chemistry C*, vol. 113, no. 38, pp. 16561–16564, 2009.

[25] R. A. Ojifinni, J. Gong, D. W. Flaherty, T. S. Kim, and C. B. Mullins, "Annealing effect on reactivity of oxygen-covered Au (111)," *The Journal of Physical Chemistry C*, vol. 113, no. 22, pp. 9820–9825, 2009.

[26] A. Krozer and M. Rodahl, "X-ray photoemission spectroscopy study of UV/ozone oxidation of Au under ultrahigh vacuum conditions," *Journal of Vacuum Science & Technology A: Vacuum, Surfaces, and Films*, vol. 15, no. 3, pp. 1704–1709, 1997.

[27] H. Tsai, E. Hu, K. Perng, M. Chen, J.-C. Wu, and Y.-S. Chang, "Instability of gold oxide Au_2O_3," *Surface science*, vol. 537, no. 1, pp. L447–L450, 2003.

[28] A. Y. Klyushin, T. C. Rocha, M. Hävecker, A. Knop-Gericke, and R. Schlögl, "A near ambient pressure XPS study of Au oxidation," *Physical Chemistry Chemical Physics*, vol. 16, no. 17, pp. 7881–7886, 2014.

[29] B. K. Min and C. M. Friend, "Heterogeneous gold-based catalysis for green chemistry: low-temperature CO oxidation and propene oxidation," *Chemical Reviews*, vol. 107, no. 6, pp. 2709–2724, 2007.

[30] B. Min, X. Deng, D. Pinnaduwage, R. Schalek, and C. Friend, "Oxygen-induced restructuring with release of gold atoms from Au (111)," *Physical Review B*, vol. 72, no. 12, p. 121410, 2005.

[31] T. A. Baker, C. M. Friend, and E. Kaxiras, "Effects of chlorine and oxygen coverage on the structure of the Au (111) surface," *The Journal of chemical physics*, vol. 130, no. 8, p. 084701, 2009.

[32] T. A. Baker, C. M. Friend, and E. Kaxiras, "Atomic oxygen adsorption on Au (111) surfaces with defects," *The Journal of Physical Chemistry C*, vol. 113, no. 8, pp. 3232–3238, 2009.

[33] T. A. Baker, X. Liu, and C. M. Friend, "The mystery of gold's chemical activity: local bonding, morphology and reactivity of atomic oxygen," *Physical Chemistry Chemical Physics*, vol. 13, no. 1, pp. 34–46, 2011.

[34] G. Rovida, F. Pratesi, M. Maglietta, and E. Ferroni, "Effects of oxygen on silver surface structure," *Journal of Vacuum Science and Technology*, vol. 9, no. 2, pp. 796–799, 1972.

[35] G. Rovida, F. Pratesi, M. Maglietta, and E. Ferroni, "Chemisorption of oxygen on the silver (111) surface," *Surface Science*, vol. 43, no. 1, pp. 230–256, 1974.

[36] H. Engelhardt and D. Menzel, "Adsorption of oxygen on silver single crystal surfaces," *Surface Science*, vol. 57, no. 2, pp. 591–618, 1976.

[37] R. Grant and R. Lambert, "Basic studies of the oxygen surface chemistry of silver: chemisorbed atomic and molecular species on pure Ag (111)," *Surface science*, vol. 146, no. 1, pp. 256–268, 1984.

[38] C. T. Campbell, "Atomic and molecular oxygen adsorption on Ag (111)," *Surface Science*, vol. 157, no. 1, pp. 43–60, 1985.

[39] V. Bukhtiyarov, A. Boronin, and V. Savchenko, "Two oxygen states and the role of carbon in partial oxidation of ethylene over silver," *Surface Science*, vol. 232, no. 1-2, pp. L205–L209, 1990.

[40] X. Bao, M. Muhler, T. Schedel-Niedrig, and R. Schlögl, "Interaction of oxygen with silver at high temperature and atmospheric pressure: a spectroscopic and structural analysis of a strongly bound surface species," *Physical Review B*, vol. 54, no. 3, p. 2249, 1996.

[41] V. Bukhtiyarov, V. Kaichev, and I. Prosvirin, "Oxygen adsorption on Ag (111): X-ray photoelectron spectroscopy (XPS), angular dependent x-ray photoelectron spectroscopy (ADXPS) and temperature-programmed desorption (TPD) studies," *The Journal of chemical physics*, vol. 111, no. 5, pp. 2169–2175, 1999.

[42] V. I. Bukhtiyarov, M. Hävecker, V. V. Kaichev, A. Knop-Gericke, R. W. Mayer, and R. Schlögl, "Atomic oxygen species on silver: Photoelectron spectroscopy and x-ray absorption studies," *Physical Review B*, vol. 67, no. 23, p. 235422, 2003.

[43] W. Huang and J. White, "Revisiting NO_2 on Ag (111): A detailed TPD and RAIRS study," *Surface science*, vol. 529, no. 3, pp. 455–470, 2003.

[44] A. Reicho, A. Stierle, I. Costina, and H. Dosch, "Stranski–krastanov like oxide growth on Ag (111) at atmospheric oxygen pressures," *Surface science*, vol. 601, no. 4, pp. L19–L23, 2007.

[45] W.-X. Li, C. Stampfl, and M. Scheffler, "Subsurface oxygen and surface oxide formation at Ag (111): A density-functional theory investigation," *Physical review B*, vol. 67, no. 4, p. 045408, 2003.

[46] A. Michaelides, M.-L. Bocquet, P. Sautet, A. Alavi, and D. King, "Structures and thermodynamic phase transitions for oxygen and silver oxide phases on Ag {111}," *Chemical physics letters*, vol. 367, no. 3, pp. 344–350, 2003.

[47] Y. Xu, J. Greeley, and M. Mavrikakis, "Effect of subsurface oxygen on the reactivity of the Ag (111) surface," *Journal of the American Chemical Society*, vol. 127, no. 37, pp. 12823–12827, 2005.

[48] M. Schmid, A. Reicho, A. Stierle, I. Costina, J. Klikovits, P. Kostelnik, O. Dubay, G. Kresse, J. Gustafson, E. Lundgren, *et al.*, "Structure of Ag (111) - p(4×4)-O: No silver oxide," *Physical review letters*, vol. 96, no. 14, p. 146102, 2006.

[49] J. Schnadt, A. Michaelides, J. Knudsen, R. T. Vang, K. Reuter, E. Lægsgaard, M. Scheffler, and F. Besenbacher, "Revisiting the structure of the p(4×4) surface oxide on Ag (111)," *Physical review letters*, vol. 96, no. 14, p. 146101, 2006.

[50] J. Schnadt, J. Knudsen, X. L. Hu, A. Michaelides, R. T. Vang, K. Reuter, Z. Li, E. Lægsgaard, M. Scheffler, and F. Besenbacher, "Experimental and theoretical study of oxygen adsorption structures on Ag (111)," *Physical Review B*, vol. 80, no. 7, p. 075424, 2009.

[51] X. Bao, M. Muhler, B. Pettinger, R. Schlögl, and G. Ertl, "On the nature of the active state of silver during catalytic oxidation of methanol," *Catalysis letters*, vol. 22, no. 3, pp. 215–225, 1993.

[52] V. Bukhtiyarov, I. Prosvirin, and R. Kvon, "Study of reactivity of oxygen states adsorbed at a silver surface towards C_2H_4 by XPS, TPD and TPR," *Surface science*, vol. 320, no. 1-2, pp. L47–L50, 1994.

[53] C. Carlisle, D. King, M.-L. Bocquet, J. Cerdá, and P. Sautet, "Imaging the surface and the interface atoms of an oxide film on Ag {111} by scanning tunneling microscopy: Experiment and theory," *Physical review letters*, vol. 84, no. 17, p. 3899, 2000.

[54] X. Bao, J. Barth, G. Lehmpfuhl, R. Schuster, Y. Uchida, R. Schlögl, and G. Ertl, "Oxygen-induced restructuring of Ag (111)," *Surface science*, vol. 284, no. 1-2, pp. 14–22, 1993.

[55] A. Michaelides, K. Reuter, and M. Scheffler, "When seeing is not believing: Oxygen on Ag (111), a simple adsorption system?," *Journal of Vacuum Science & Technology A: Vacuum, Surfaces, and Films*, vol. 23, no. 6, pp. 1487–1497, 2005.

[56] S. Günther, S. Böcklein, J. Wintterlin, M. A. Niño, T. O. Menteş, and A. Locatelli, "Locating catalytically active oxygen on Ag (111) - A spectromicroscopy study," *ChemCatChem*, vol. 5, no. 11, pp. 3342–3350, 2013.

[57] N. Martin, S. Klacar, H. Gronbeck, J. Knudsen, J. Schnadt, S. Blomberg, J. Gustafson, and E. Lundgren, "High-coverage oxygen-induced surface structures on Ag (111)," *The Journal of Physical Chemistry C*, vol. 118, no. 28, pp. 15324–15331, 2014.

[58] J. Derouin, R. G. Farber, S. L. Heslop, and D. R. Killelea, "Formation of surface oxides and Ag_2O thin films with atomic oxygen on Ag (111)," *Surface Science*, vol. 641, pp. L1–L4, 2015.

[59] T. E. Jones, T. C. Rocha, A. Knop-Gericke, C. Stampfl, R. Schlögl, and S. Piccinin, "Thermodynamic and spectroscopic properties of oxygen on silver under an oxygen atmosphere," *Physical Chemistry Chemical Physics*, vol. 17, no. 14, pp. 9288–9312, 2015.

[60] C. Heine, B. Eren, B. A. Lechner, and M. Salmeron, "A study of the O/Ag (111) system with scanning tunneling microscopy and X-ray photoelectron spectroscopy at ambient pressures," *Surface Science*, vol. 652, pp. 51–57, 2016.

[61] J. Derouin, R. G. Farber, M. E. Turano, E. V. Iski, and D. R. Killelea, "Thermally selective formation of subsurface oxygen in Ag (111) and consequent surface structure," *ACS Catalysis*, vol. 6, no. 7, pp. 4640–4646, 2016.

[62] B. V. Andryushechkin, V. M. Shevlyuga, T. V. Pavlova, G. M. Zhidomirov, and K. Eltsov, "Structural transformations on an oxidized Ag (111) surface," *JETP Letters*, vol. 105, no. 5, pp. 292–296, 2017.

[63] T. C. Rocha, A. Oestereich, D. V. Demidov, M. Hävecker, S. Zafeiratos, G. Weinberg, V. I. Bukhtiyarov, A. Knop-Gericke, and R. Schlögl, "The silver-oxygen system in catalysis: new insights by near ambient pressure x-ray photoelectron spectroscopy," *Physical Chemistry Chemical Physics*, vol. 14, no. 13, pp. 4554–4564, 2012.

[64] S. L. Schroeder and M. Gottfried, "Temperature-programmed desorption (TPD) thermal desorption spectroscopy (TDS)," *Userpage. Chemie. Fu-Berlin. De*, pp. 1–22, 2002.

[65] J. W. Niemantsverdriet, *Spectroscopy in catalysis*. John Wiley & Sons, 2007.

[66] D. A. King, "Thermal desorption from metal surfaces: A review," *Surface Science*, vol. 47, no. 1, pp. 384–402, 1975.

[67] I. Chorkendorff and J. W. Niemantsverdriet, *Concepts of modern catalysis and kinetics*. John Wiley & Sons, 2003.

[68] S. J. Garrett, "CHEM924 lecture notes, special topics in analytical chemistry- introduction to surface analysis," pp. 13.8–13.10, 2001.

[69] P. Redhead, "Thermal desorption of gases," *Vacuum*, vol. 12, no. 4, pp. 203–211, 1962.

[70] E. Habenschaden and J. Küppers, "Evaluation of flash desorption spectra," *Surface Science*, vol. 138, no. 1, pp. L147–L150, 1984.

[71] C. C. Chusuei and D. W. Goodman, "X-ray photoelectron spectroscopy," *Encyclopedia of physical science and technology*, vol. 17, pp. 921–938, 2002.

[72] Riber, "X-ray source model CX 700 and its power supply unit model ACX 700," *Instruction Manual*, vol. No: 608 362 02 P.

[73] Riber, "MAC 2 - analysis module and EA 150 - analyser," *Instructions Manual*, vol. No: 608 361 82 T.

[74] F. M. Hoffmann, "Infrared reflection-absorption spectroscopy of adsorbed molecules," *Surface Science Reports*, vol. 3, no. 2-3, pp. 107109–192, 1983.

[75] H. Bubert and H. Jenett, "Surface and thin film analysis: principles, instrumentation, applications," 2002.

[76] J. Pireaux, M. Chtaib, J. Delrue, P. Thiry, M. Liehr, and R. Caudano, "Electron spectroscopic characterization of oxygen adsorption on gold surfaces: I. substrate impurity effects on molecular oxygen adsorption in ultra high vacuum," *Surface science*, vol. 141, no. 1, pp. 211–220, 1984.

[77] X. Deng, B. K. Min, A. Guloy, and C. M. Friend, "Enhancement of O_2 dissociation on Au (111) by adsorbed oxygen: implications for oxidation catalysis," *Journal of the American Chemical Society*, vol. 127, no. 25, pp. 9267–9270, 2005.

[78] R. Ford and J. Pritchard, "Chemisorption of oxygen on gold," *Chemical Communications (London)*, no. 7, pp. 362–363, 1968.

[79] J. Gottfried, K. Schmidt, S. Schroeder, and K. Christmann, "Spontaneous and electron-induced adsorption of oxygen on Au (110)-(1×2)," *Surface science*, vol. 511, no. 1, pp. 65–82, 2002.

[80] T. S. Kim, J. D. Stiehl, C. T. Reeves, R. J. Meyer, and C. B. Mullins, "Cryogenic CO oxidation on TiO_2-supported gold nanoclusters precovered with atomic oxygen," *Journal of the American Chemical Society*, vol. 125, no. 8, pp. 2018–2019, 2003.

[81] J. Pireaux, M. Liehr, P. Thiry, J. Delrue, and R. Caudano, "Electron spectroscopic characterization of oxygen adsorption on gold surfaces: II. production of gold oxide in oxygen DC reactive sputtering," *Surface science*, vol. 141, no. 1, pp. 221–232, 1984.

[82] J. Wang, M. R. Voss, H. Busse, and B. E. Koel, "Chemisorbed oxygen on Au (111) produced by a novel route: reaction in condensed films of NO^{2+} H_2O," *The Journal of Physical Chemistry B*, vol. 102, no. 24, pp. 4693–4696, 1998.

[83] D. H. Parker and B. E. Koel, "Chemisorption of high coverages of atomic oxygen on the Pt (111), Pd (111), and Au (111) surfaces," *Journal of Vacuum Science & Technology A: Vacuum, Surfaces, and Films*, vol. 8, no. 3, pp. 2585–2590, 1990.

[84] J. Wang and B. E. Koel, "IRAS studies of NO_2, N_2O_3, and N_2O_4 adsorbed on Au (111) surfaces and reactions with coadsorbed H_2O," *The Journal of Physical Chemistry A*, vol. 102, no. 44, pp. 8573–8579, 1998.

[85] J. Wang and B. E. Koel, "Reactions of N_2O_4 with ice at low temperatures on the Au (111) surface," *Surface science*, vol. 436, no. 1, pp. 15–28, 1999.

[86] J. Barth, H. Brune, G. Ertl, and R. Behm, "Scanning tunneling microscopy observations on the reconstructed Au (111) surface: Atomic structure, long-range superstructure, rotational domains, and surface defects," *Physical Review B*, vol. 42, no. 15, p. 9307, 1990.

[87] M. Van Hove, R. Koestner, P. Stair, J. Biberian, L. L. Kesmodel, I. Bartoš, and G. Somorjai, "The surface reconstructions of the (100) crystal faces of iridium, platinum and gold: I. experimental observations and possible structural models," *Surface Science*, vol. 103, no. 1, pp. 189–217, 1981.

[88] U. Harten, A. Lahee, J. P. Toennies, and C. Wöll, "Observation of a soliton reconstruction of Au (111) by high-resolution helium-atom diffraction," *Physical review letters*, vol. 54, no. 24, p. 2619, 1985.

[89] Y. Hasegawa and P. Avouris, "Manipulation of the reconstruction of the Au (111) surface with the stm," *SCIENCE-NEW YORK THEN WASHINGTON-*, vol. 258, pp. 1763–1763, 1992.

[90] Y. Wang, N. S. Hush, and J. R. Reimers, "Simulation of the Au (111)-(22×3) surface reconstruction," *Physical Review B*, vol. 75, no. 23, p. 233416, 2007.

[91] R. Meyer, C. Lemire, S. K. Shaikhutdinov, and H.-J. Freund, "Surface chemistry of catalysis by gold," *Gold Bulletin*, vol. 37, no. 1-2, pp. 72–124, 2004.

[92] J. Chastain, R. C. King, and J. Moulder, *Handbook of X-ray photoelectron spectroscopy: a reference book of standard spectra for identification and interpretation of XPS data*. Physical Electronics Division, Perkin-Elmer Corporation Eden Prairie, Minnesota, 1992.

[93] N. Saliba, D. Parker, and B. Koel, "Adsorption of oxygen on Au (111) by exposure to ozone," *Surface science*, vol. 410, no. 2, pp. 270–282, 1998.

[94] J. Gong and C. B. Mullins, "Surface science investigations of oxidative chemistry on gold," *Accounts of chemical research*, vol. 42, no. 8, pp. 1063–1073, 2009.

[95] A. G. Sault, R. J. Madix, and C. T. Campbell, "Adsorption of oxygen and hydrogen on Au (110)-(1×2)," *Surface science*, vol. 169, no. 2-3, pp. 347–356, 1986.

[96] K. A. Davis and D. W. Goodman, "Propene adsorption on clean and oxygen-covered Au (111) and Au (100) surfaces," *The Journal of Physical Chemistry B*, vol. 104, no. 35, pp. 8557–8562, 2000.

[97] J. Gong, R. A. Ojifinni, T. S. Kim, J. D. Stiehl, S. M. McClure, J. M. White, and C. B. Mullins, "Low temperature CO oxidation on Au (111) and the role of adsorbed water," *Topics in Catalysis*, vol. 44, no. 1, pp. 57–63, 2007.

[98] J. L. Gland and E. B. Kollin, "Carbon monoxide oxidation on the Pt (111) surface: Temperature programmed reaction of coadsorbed atomic oxygen and carbon monoxide," *The Journal of Chemical Physics*, vol. 78, no. 2, pp. 963–974, 1983.

[99] P. S. Bagus, C. Brundle, F. Illas, F. Parmigiani, and G. Polzonetti, "Evidence for oxygen-island formation on Al (111): Cluster-model theory and x-ray photoelectron spectroscopy," *Physical Review B*, vol. 44, no. 16, p. 9025, 1991.

[100] I. Nakai, H. Kondoh, K. Amemiya, M. Nagasaka, T. Shimada, R. Yokota, A. Nambu, and T. Ohta, "Mechanism of the CO oxidation reaction on O-precovered Pt (111) surfaces studied with near-edge x-ray absorption fine

structure spectroscopy," *The Journal of chemical physics*, vol. 122, no. 13, p. 134709, 2005.

[101] J. Gottfried, K. Schmidt, S. Schroeder, and K. Christmann, "Oxygen chemisorption on Au (110)-(1×2) I. thermal desorption measurements," *Surface science*, vol. 525, no. 1, pp. 184–196, 2003.

[102] S. D. Miller and J. R. Kitchin, "Relating the coverage dependence of oxygen adsorption on Au and Pt fcc (111) surfaces through adsorbate-induced surface electronic structure effects," *Surface Science*, vol. 603, no. 5, pp. 794–801, 2009.

[103] B. Koslowski, H.-G. Boyen, C. Wilderotter, G. Kästle, P. Ziemann, R. Wahrenberg, and P. Oelhafen, "Oxidation of preferentially (111)-oriented Au films in an oxygen plasma investigated by scanning tunneling microscopy and photoelectron spectroscopy," *Surface science*, vol. 475, no. 1, pp. 1–10, 2001.

[104] H. Shi and C. Stampfl, "First-principles investigations of the structure and stability of oxygen adsorption and surface oxide formation at Au (111)," *Physical Review B*, vol. 76, no. 7, p. 075327, 2007.

[105] C. R. Aita and N. C. Tran, "Core level and valence band x-ray photoelectron spectroscopy of gold oxide," *Journal of Vacuum Science & Technology A: Vacuum, Surfaces, and Films*, vol. 9, no. 3, pp. 1498–1500, 1991.

[106] J. Kim, Z. Dohnálek, and B. D. Kay, "Cryogenic CO_2 formation on oxidized gold clusters synthesized via reactive layer assisted deposition," *Journal of the American Chemical Society*, vol. 127, no. 42, pp. 14592–14593, 2005.

[107] J. Gong, D. W. Flaherty, R. A. Ojifinni, J. M. White, and C. B. Mullins, "Surface chemistry of methanol on clean and atomic oxygen pre-covered Au (111)," *The Journal of Physical Chemistry C*, vol. 112, no. 14, pp. 5501–5509, 2008.

[108] W.-S. Sim, P. Gardner, and D. King, "The interaction of methanol with clean and oxygen-precovered Ag {111}: A RAIRS study," *Surface Review and Letters*, vol. 1, no. 04, pp. 673–676, 1994.

[109] B. Sexton, A. Hughes, and N. Avery, "A spectroscopic study of the adsorption and reactions of methanol, formaldehyde and methyl formate on clean and oxygenated Cu (110) surfaces," *Surface science*, vol. 155, no. 1, pp. 366–386, 1985.

[110] S. Şenozan, H. Ustunel, M. Karatok, E. I. Vovk, A. A. Shah, E. Ozensoy, and D. Toffoli, "Comparative analysis of reactant and product adsorption energies in the selective oxidative coupling of alcohols to esters on Au (111)," *Topics in Catalysis*, vol. 59, no. 15-16, pp. 1383–1393, 2016.

[111] D. Outka and R. Madix, "Bronsted basicity of atomic oxygen on the Au (110) surface: reactions with methanol, acetylene, water, and ethylene," *Journal of the American Chemical Society*, vol. 109, no. 6, pp. 1708–1714, 1987.

[112] "*NIST C*hemistry *W*ebbook, http://webbook.nist.gov/cgi/cbook.cgi?id=c107313&units=si&mask=200#mass-spec," (accessed Sept 10, 2017), Mass spectrum of methyl formate.

[113] B. Xu, X. Liu, J. Haubrich, R. J. Madix, and C. M. Friend, "Selectivity control in gold-mediated esterification of methanol," *Angewandte Chemie International Edition*, vol. 48, no. 23, pp. 4206–4209, 2009.

[114] I. S. Nielsen, E. Taarning, K. Egeblad, R. Madsen, and C. H. Christensen, "Direct aerobic oxidation of primary alcohols to methyl esters catalyzed by a heterogeneous gold catalyst," *Catalysis Letters*, vol. 116, no. 1-2, pp. 35–40, 2007.

[115] M. Pan, D. W. Flaherty, and C. B. Mullins, "Low-temperature hydrogenation of acetaldehyde to ethanol on H-precovered Au (111)," *The Journal of Physical Chemistry Letters*, vol. 2, no. 12, pp. 1363–1367, 2011.

[116] M. A. Henderson, Y. Zhou, and J. White, "Polymerization and decomposition of acetaldehyde on Ru (001)," *Journal of the American Chemical Society*, vol. 111, no. 4, pp. 1185–1193, 1989.

[117] H. Zhao, J. Kim, and B. E. Koel, "Adsorption and reaction of acetaldehyde on Pt (111) and Sn/Pt (111) surface alloys," *Surface science*, vol. 538, no. 3, pp. 147–159, 2003.

[118] W. Sim, P. Gardner, and D. King, "Surface-bound helical polyacetaldehyde chains and bidentate acetate intermediates on Ag {111}," *Journal of the American Chemical Society*, vol. 118, no. 41, pp. 9953–9959, 1996.

[119] J. Davis and M. Barteau, "Polymerization and decarbonylation reactions of aldehydes on the Pd (111) surface," *Journal of the American Chemical Society*, vol. 111, no. 5, pp. 1782–1792, 1989.

[120] M. Karatok, E. I. Vovk, A. A. Shah, A. Turksoy, and E. Ozensoy, "Acetaldehyde partial oxidation on the Au (111) model catalyst surface: C–C bond activation and formation of methyl acetate as an oxidative coupling product," *Surface Science*, vol. 641, pp. 289–293, 2015.

[121] Y. Li and M. Bowker, "Acetic acid on Rh (110): The stabilization and autocatalytic decomposition of acetate," *Journal of Catalysis*, vol. 142, no. 2, pp. 630–640, 1993.

[122] G. B. Fisher, "The electronic structure of two forms of molecular ammonia adsorbed on Pt (111)," *Chemical Physics Letters*, vol. 79, no. 3, pp. 452–458, 1981.

[123] R. Van Hardeveld, R. Van Santen, and J. Niemantsverdriet, "The adsorption of NH_3 on Rh (111)," *Surface science*, vol. 369, no. 1-3, pp. 23–35, 1996.

[124] A. Santra, B. Min, C. Yi, K. Luo, T. Choudhary, and D. Goodman, "Decomposition of NH_3 on Ir (100): A temperature programmed desorption study," *The Journal of Physical Chemistry B*, vol. 106, no. 2, pp. 340–344, 2002.

[125] B. D. Kay, K. R. Lykke, J. R. Creighton, and S. J. Ward, "The influence of adsorbate–absorbate hydrogen bonding in molecular chemisorption: NH_3, HF, and H_2O on Au (111)," *The Journal of chemical physics*, vol. 91, no. 8, pp. 5120–5121, 1989.

[126] C. Backx, C. De Groot, and P. Biloen, "Adsorption of oxygen on Ag (110) studied by high resolution ELS and TPD," *Surface Science*, vol. 104, no. 1, pp. 300–317, 1981.

[127] S. R. Bare, K. Griffiths, W. Lennard, and H. Tang, "Generation of atomic oxygen on Ag (111) and Ag (110) using NO_2: a TPD, LEED, HREELS, XPS and NRA study," *Surface science*, vol. 342, no. 1-3, pp. 185–198, 1995.

[128] R. Reichelt, S. Günther, M. Rößler, J. Wintterlin, B. Kubias, B. Jakobi, and R. Schlögl, "High-pressure STM of the interaction of oxygen with Ag (111)," *Physical Chemistry Chemical Physics*, vol. 9, no. 27, pp. 3590–3599, 2007.

[129] H. G. Jenniskens, P. W. Dorlandt, M. F. Kadodwala, and A. W. Kleyn, "The adsorption of methanol on Ag (111) studied with TDS and XPS," *Surface science*, vol. 357, pp. 624–628, 1996.

[130] W. Sim, P. Gardner, and D. King, "Structure and reactivity of the surface methoxy species on Ag {111}," *The Journal of Physical Chemistry*, vol. 99, no. 43, pp. 16002–16010, 1995.

[131] J. Russell, S. M. Gates, and J. Yates, "Reaction of methanol with Cu (111) and Cu (111) + O (ads)," *Surface science*, vol. 163, no. 2-3, pp. 516–540, 1985.

[132] W. Sim, P. Gardner, and D. King, "Multiple bonding configurations of adsorbed formate on Ag {111}," *The Journal of Physical Chemistry*, vol. 100, no. 30, pp. 12509–12516, 1996.

[133] J. L. Gland, B. A. Sexton, and G. E. Mitchell, "Ammonia adsorption on the Ag (110) surface," *Surface Science*, vol. 115, no. 3, pp. 623–632, 1982.

[134] E. Sälli, S. Martiskainen, and L. Halonen, "Computational study of the vibrational structure of the ammonia molecule adsorbed on the fcc (111) transition metal surfaces," *The Journal of Physical Chemistry C*, vol. 116, no. 28, pp. 14960–14969, 2012.

[135] Z. Xu, L. Hanley, and J. T. Yates Jr, "Layer interactions between dissimilar adsorbates. NH_3 layers on chemisorbed CO on Ni (111): A reflection infrared study," *The Journal of chemical physics*, vol. 96, no. 2, pp. 1621–1627, 1992.

[136] J. Rodriguez, W. K. Kuhn, C. M. Truong, and D. W. Goodman, "A FT-IRAS study of ammonia adsorbed on Ru (0001)," *Surface science*, vol. 271, no. 3, pp. 333–339, 1992.

[137] I. Villegas and M. J. Weaver, "Infrared spectroscopy of model electrochemical interfaces in ultrahigh vacuum: interfacial cation solvation by ammonia on Pt (111)," *Surface science*, vol. 367, no. 2, pp. 162–176, 1996.

[138] C.-M. Pradier, A. Adamski, C. Méthivier, and I. Louis-Rose, "Interaction of NH_3 and oxygen with Cu (110), investigated by FT-IRAS," *Journal of Molecular Catalysis A: Chemical*, vol. 186, no. 1, pp. 193–201, 2002.

[139] T. Fukushima, M.-B. Song, and M. Ito, "Local work-function changes of Pt (111) studied by STM and IRAS: coadsorption of Cl - with H_3O^+, NO, and CO molecules," *Surface science*, vol. 464, no. 2, pp. 193–199, 2000.

[140] J. Gohndrone, C. Olsen, A. Backman, T. Gow, E. Yagasaki, and R. Masel, "Ammonia adsorption and decomposition on several faces of platinum," *Journal of Vacuum Science & Technology A: Vacuum, Surfaces, and Films*, vol. 7, no. 3, pp. 1986–1990, 1989.

[141] A. Klust and R. J. Madix, "Mesoscopic restructuring and mass transport of metal atoms during reduction of the Ag(111)-p(4×4)- O surface with CO," *The Journal of chemical physics*, vol. 126, no. 8, p. 084707, 2007.

[142] "*NIST C*hemistry *W*ebbook, http://webbook.nist.gov/cgi/cbook.cgi?id=c10024972&units=si&mask=200#mass-spec," (accessed Sept 10, 2017), Mass spectrum of nitrous oxide.

[143] "*NIST C*hemistry *W*ebbook, http://webbook.nist.gov/cgi/cbook.cgi?id=c64197&units=si&mask=200#mass-spec," (accessed Sept 10, 2017), Mass spectrum of acetic acid.

Appendix A

Diagram of the IRAS Setup

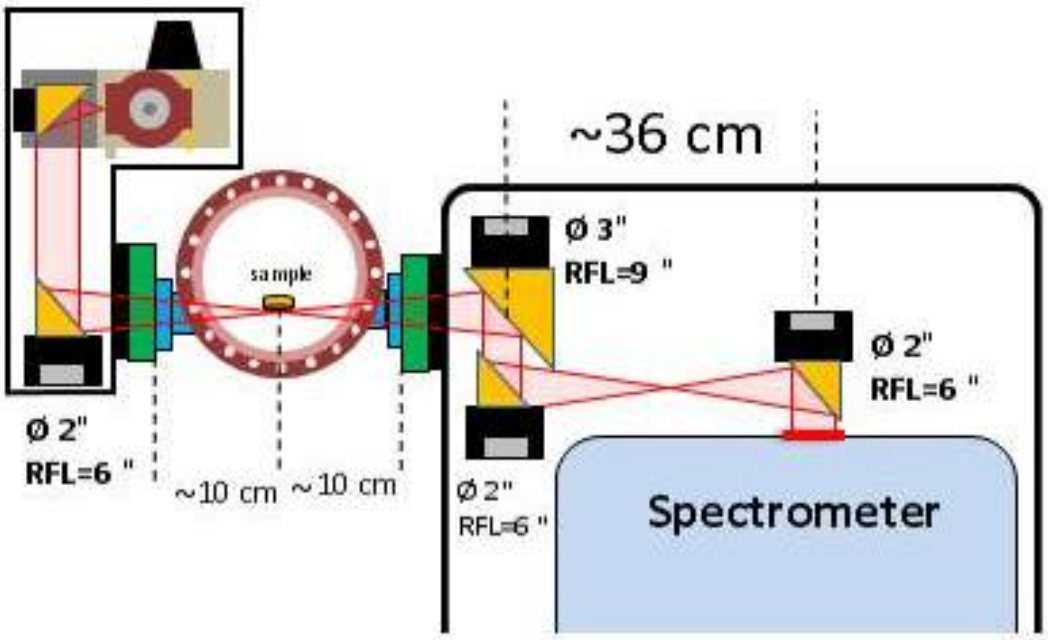

Appendix B

QMS Fragmentation Patterns of the Chemicals

Chemical/*(m/z)*	16	17	28	29	30	31	32	43	44	45	59	60	74
Methanol	-	-	35	86	14	100	65	-	-	-	-	-	-
Formaldehyde	-	-	59	100	73	3	-	-	-	-	-	-	-
Methyl formate [112]	-	-	5	46	7	100	46	-	-	-	-	40	-
Acetaldehyde	-	-	-	100	-	-	-	26	31	-	-	-	-
Methyl acetate	-	-	-	9	-	-	-	100	-	-	5	-	11
Acetic acid [143]	-	-	-	9	-	-	-	100	-	89	-	74	-
Ammonia	90	100	-	-	-	-	-	-	-	-	-	-	-

Appendix C

Infrared Frequencies and Mode Assignments for Methanol and Methoxy Species on Ag(111)

Molecule/ Mode (cm^{-1})	ν(OH)	$\nu_{as}(CH_3)$	$2\delta_{as}(CH_3)$	$2\delta_s(CH_3)$	$\nu_s(CH_3)$	2ν(CO)	$\delta_{as}(CH_3)$	$\delta_s(CH_3)$	ν(CO)
CH_3OH	-	2943	2917	-	2830	-	-	1451	1038
CH_3OH [130]	-	2947	2920	-	2828	-	1482	1455	1026
CH_3O	3631	-	2909	2873	2790	-	-	-	1041
CH_3O [130]	-	-	2907	2874	2792	2031	-	1432	1048
CH_3OH(g)[130]	3667	3006 2962	2956 2921	2893	2848	2054	1473 1466	1452	1034

Appendix D

Alternative depiction of TPRS data for ammonia SCO reaction

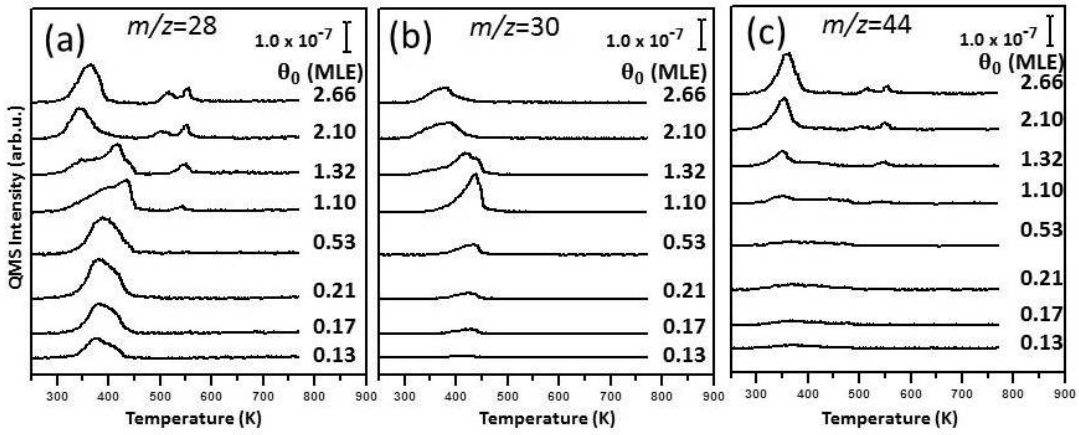

Figure D.1: Alternative depiction of the TPRS data corresponding to the various ammonia SCO reaction products (*i.e.* N_2, NO, N_2O) for the reaction between ammonia and oxygen pre-covered Ag(111) surfaces as a function of oxygen coverage. For all of the data, oxygen was delivered on Ag(111) by ozone exposure at 140 K, while NH_3 was delivered after ozone using an identical ammonia exposure at 250 K ($P(NH_3) = 2.0 \times 10^{-9}$ Torr $\times$ 60 sec.)

Appendix E

TPRS profiles for NH_3 and H_2O during ammonia SCO reaction

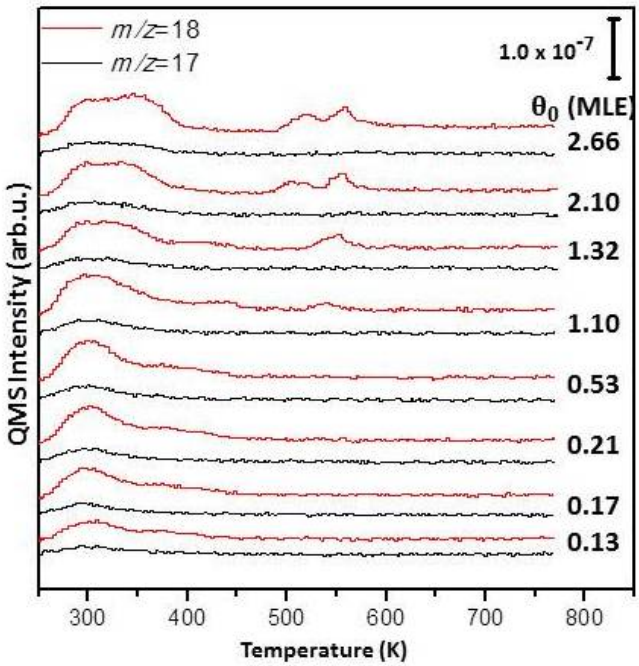

Figure E.1: TPRS profiles for NH_3 ($m/z = 17$) and H_2O ($m/z = 18$) desorption channels obtained during the reaction between ammonia and oxygen pre-covered Ag(111) surfaces as a function of oxygen coverage as shown in Figure 4.18 of the main text.

Appendix F

List of Publications

- **Karatok, M.**, Vovk, E. I., Shah, A. A., Turksoy, A., Ozensoy, E. **(2015)**. Acetaldehyde Partial Oxidation on the Au (111) Model Catalyst Surface: C-C Bond Activation and Formation of Methyl Acetate as an Oxidative Coupling Product. **Surface Science**, 641, 289-293.

- Şenozan, S., Ustunel, H., **Karatok, M.**, Vovk, E. I., Shah, A. A., Ozensoy, E., Toffoli, D. **(2016)**. Comparative Analysis of Reactant and Product Adsorption Energies in the Selective Oxidative Coupling of Alcohols to Esters on Au (111). **Topics in Catalysis**, 59(15-16), 1383-1393.

- Erdogan, D. A., Sevim, M., Kısa, E., Emiroglu, D. B., **Karatok, M.**, Vovk, E. I., Bjerring, M., Akbey, Ü., Metin, Ö., Ozensoy, E. **(2016)**. Photocatalytic Activity of Mesoporous Graphitic Carbon Nitride (mpg-C_3N_4) towards Organic Chromophores under UV and VIS Light Illumination. **Topics in Catalysis**, 59(15-16), 1305-1318.

- **Karatok, M.**, Vovk, E. I., Koc, A. V., Ozensoy, E. **(2017)**. Selective Catalytic Ammonia Oxidation to Nitrogen by Atomic Oxygen Species on Ag (111). **The Journal of Physical Chemistry C**, (in press, DOI: 10.1021/acs.jpcc.7b08291).

- **Karatok, M.**, Vovk, E. I., Shah, A. A., Ozensoy, E. Revisiting the Nature of Oxygen on Au(111). (in preparation).

- **Karatok, M.**, Vovk, E. I., Ozensoy, E. Reactivity of Oxygen Species in Methanol Partial Oxidation Reaction Pathways on Ag(111). (in preparation).

- Ercan, K.E., Say, Z., Kurt, M., **Karatok, M.**, Pantaleo, G., Liotta, L. F., Ozensoy, E. New Generation Pt-Free $LaCo_xMn_{1-x}O_3$ Type Advanced Hybrid Perovskites with Fine-Tunable Properties for NO_x Removal Systems (in preparation).

- Persembe, E., **Karatok, M.**, Zahmakiran, M., Ozensoy, E. CO-Tolerant Trimetallic PgAgCr Nanoparticles Promoted with MnO_x for Additive-Free Ultra-Pure Hydrogen Production from Formic Acid. (in preparation).